# Local Structure in Hard Particle Self-Assembly and Assembly Failure

by

Erin Griffin Teich

A dissertation submitted in partial fulfillment
of the requirements for the degree of
Doctor of Philosophy
(Applied Physics)
in The University of Michigan
2018

Doctoral Committee:

Professor Sharon C. Glotzer, Chair
Professor Greg van Anders
Professor Xiaoming Mao
Professor Michael J. Solomon
Professor Robert Ziff

Erin Griffin Teich

erteich@umich.edu

ORCID iD: 0000-0001-7553-7054

For my parents.

# ACKNOWLEDGEMENTS

I'd like to thank my advisor, Sharon Glotzer– thank you so much for your support and for teaching me how to be a good scientist and to ask the right questions. Greg van Anders, it has been such a wonderful experience to work with you for these many years and to learn from you– you've been an invaluable mentor and source of support. Thank you also to the other members of my committee, Xiaoming Mao, Bob Ziff, and Mike Solomon– I really appreciate your time, and your interesting and informed questions have made my work so much better. And to Karen Coulter, our lab manager– you are such a steady rock in our lab; thank you so much for everything that you do to help us run smoothly and to support us. I have also been the grateful beneficiary of fellowships from the National Science Foundation and the Blue Waters sustained petascale computing project.

I've been so fortunate to work with so many wonderful scientists and people during my years here– thank you to all Glotzer group members past and present who have made the lab a scientifically fascinating, supportive environment. Daphne Klotsa, you have been a wonderful mentor and friend to me ever since I first joined the group. Ben Schultz and Pablo Damasceno, thank you also for your friendship and scientific mentorship when I was new in the group– I learned so much from both of you. Chrisy Du, Jim Antonaglia, and Paul Dodd, you've been such great friends and sources of support, not to mention incredible scientists who have taught me so much. I'd also like to thank Josh Anderson, Matthew Spellings, Jens Glaser, and Simon Adorf– you have written some incredible code that I would be completely sunk without, and your

dedication to helping me and others use your software and generally become better programmers is so generous. Thank you. And to Julia Dshemuchadse, you have been just such a wonderful friend and true mentor for these many years– I'm so grateful to you for your advice and for always being willing to listen and ready to help. Thank you so much.

My friends and family in Ann Arbor are, in my humble opinion, the most kind, caring, funny, and smart individuals in the state, and it has been a pleasure to be distracted from physics and to explore Michigan with you all. To Grace and Gan, I'd be such a less happy human without you. I love you so much– thank you for your unwavering support and inexplicable interest in the minutiae of my daily existence. To my sisters, Sunny and Hayley, I'm so lucky to have such kind and strong and brilliant role models; thank you for your lifelong support and love. Jordan, I'm so happy you are a part of our family. Special thanks to Rowan Benjamin Teichstrom and Xander Jack Teichstrom for existing and for enormously helpful discussions over the past three years. And to my parents, no words can express what you mean to me. You are my biggest advocates and you have believed in me when I didn't believe in myself. I'm so lucky to have you. This thesis is dedicated to you– thank you so much for your love.

# TABLE OF CONTENTS

# LIST OF FIGURES

**Figure**

# LIST OF TABLES

**Table**

# LIST OF APPENDICES

**Appendix**

# ABSTRACT

The relationship between local order and global structure is not often a straightforward one in systems on the nano- and microscale in which interactions are usually weak and thermal fluctuations drive self-assembly. Moreover, structure in systems for which particle symmetry is broken is difficult to describe theoretically on any level higher than a pairwise one, due to the prohibitively high-dimensional nature of the relevant configuration space. However, a thorough understanding of local structure in all phases of soft matter systems is necessary to gain a complete picture of the physics of these systems and to leverage them for technological and materials science applications. In this dissertation, I investigate local structure in systems of anisotropic particles mediated exclusively by entropy maximization. Specifically, I explore the role of local structure in crystallization and its failure by tackling two related lines of inquiry.

First, I study the interplay between particle shape and spherical confinement in systems of hard polyhedral particles, to examine locally dense clusters of anisotropic particles and their possible connection to preferred local structures during unconfined self-assembly. I use Monte Carlo simulation methods to find putative densest clusters of the Platonic solids in spherical confinement, for up to $N = 60$ constituent particles. I find that a spherical boundary suppresses the packing influence of particle shape and produces a robust class of common cluster structures. I also find a range of especially dense clusters at so-called "magic numbers" of constituent particles, and discover that a magic-number cluster of tetrahedra is a prominent motif in the self-assembled structure of tetrahedra, the dodecagonal quasicrystal.

Second, I explore the influence of local structure in systems of hard polyhedral particles that fail to crystallize. I use a shape landscape, or a two-dimensional space of particles that are continuously interrelated by a set of shape perturbations, to investigate why slight changes to particle shape sometimes result in the vitrification rather than crystallization of dense monatomic systems of these particles. I show that assembly failure in these systems arises from a multiplicity of competing local structures, each of which is prevalent in ordered phases crystallized by particles that are only slightly different in shape. Thus, systems that fail to assemble do so because they cannot crystallize into any one ordered phase.

Third, I demonstrate that fragility in these systems, a technologically relevant measure of glass-forming ability, can be tuned by slight changes to particle shape. I relate this finding to simulations of molecular systems in which fragility is linked to intermolecular bond angle.

Finally, I detail the methods and applications of software I developed to detect multi-particle local structure in real space. This software is open-source and in current use, and has already been utilized for local structure detection in several papers by myself and others.

I conclude this dissertation by providing an outlook on the implications and future directions of my work.

# CHAPTER I

# Introduction

## 1.1 Self-assembly in soft matter

*Soft condensed matter* is a fairly modern classification for materials whose length scales lie in the nano- to microscopic range, and whose energy scales lie within the range of a few $k_BT$ (where $k_B$ is Boltzmann's constant and T is the temperature of the system) [1]. These two criteria have profound implications for the phase behavior of soft matter – since the strength of the interaction between system components is on the order of the thermal energy of the system, thermal fluctuations have the ability to spontaneously drive structural evolution. Self-assembly typically occurs on multiple length scales, and can result in surprisingly complex structures. Examples of soft matter include polymer melts, colloidal solutions, liquid crystals, gels, glasses, foams, membranes, and micelles [1].

It has been shown computationally, experimentally, and theoretically that the size, shape, and interactions of self-assembling building blocks greatly affect the resulting structure. Specifically, breaking the symmetry of the building block, rendering it *anisotropic* in some way (e.g. through faceting, surface patterning, or changes to aspect ratio), enables the assembly of a wide variety of target structures with symmetries and hierarchical features not ordinarily achievable by spherical or otherwise isotropic building blocks alone [2]. Recent experimental advances in (for example)

selective deposition, surface templating, emulsion drying, and lithography have made the prospect of anisotropic particle assembly an increasingly intriguing one [2–15].

Prediction and control of self-assembly in soft matter systems of anisotropic building blocks is not straight-forward. Nevertheless, precise control over structure on the nano- and micro-scale enables the development of novel materials for optical cloaking [16], information storage [17], computation on the mesoscale [18], adaptation [19] and self-replication [20], drug delivery [21], and tissue scaffolding [22], among other applications. Even the failure of materials to organize in a predictable or periodic fashion is leveraged in a variety of current technologies, including rewritable data storage devices [23], fiber optic networks [24], and innumerable other applications that utilize glass. Thus, control over the failure of assembly is equally useful. More generally, the quest to predict and understand soft matter systems is a playground for the development of statistical mechanical tools, both analytical and computational, due to the typical size of systems under consideration and their classical (rather than quantum) nature.

## 1.2 Local structure

Control over self-assembly requires a comprehensive understanding of the fluid or liquid state of any system, as this is often the phase through which useful crystalline structures are accessed in experiments and in nature. Fluids have traditionally been treated in the formalism of statistical mechanics as isotropic media, characterized fully by their pair correlation function $g(r)$ [25]. Indeed, this treatment has historically had major success in describing phase behavior, phase transitions, and other macroscopic phenomena in a variety of systems [25]. However, the treatment of any fluid as a spatially homogeneous medium is an oversimplification. As one may imagine, systems with components that interact, whether those interactions are isotropic or anisotropic, naturally have preferred local structures. These local arrangements vary in size and

shape, and depend on the governing interactions. Accordingly, a full treatment of the self-assembly of any system should include a consideration of local structure in its fluid.

Local structure is already presumed by many in the glass community to play an important role in the vitrification of supercooled liquids or supercompressed fluids [26]. By definition, supercooled liquids are below the melting temperature (or supercompressed fluids above the crystallization density), so it is reasonable that local structure might exist and persist in these systems. Work on the structure of supercooled liquids began over 50 years ago, when Sir Charles Frank showed that an icosahedral arrangement of 12 particles around a central one is the most energetically preferred in a theoretical model for simple monatomic liquids [27]. Bernal later considered general structures prevalent in random dense packings of hard sphere liquid models, and work has since continued unabated to identify other prevalent structures in supercooled metallic [28] and other [26] systems.

Whether or not local structure persists into the fluid regime is a topic of greater debate and fewer systematic investigations. Evidence of this persistence is rather incontrovertible in systems with strong or directional interactions, including notably tetrahedral liquids like water and silicon [29]. There have been some attempts to treat local structures in the fluid, and their influence on crystallization, in a formal sense [30–32], including the proposal of an idea that there may be a loose three-dimensional corollary to the two-dimensional hexatic phase [33], but these ideas have fallen out of favor. Crystallization is still primarily explained through Classical Nucleation Theory, in which crystalline nuclei form spontaneously out of a homogeneous fluid background rather than resulting from any rearrangement of local structures [34]. However, Tanaka *et al.* [35] posit that bond-orientational ordering and formation of local structures, in addition to density-based crystalline ordering, is required to fully understand crystallization from the fluid. Those ideas will be explored more in

Chapter IV of this dissertation.

## 1.3 Local dense packing in hard anisotropic fluids

In systems where interactions between particles are anisotropic, the identification of significant local structure in the fluid is less analytically tractable, due to the several-fold increase in dimensionality needed to characterize particle arrangements. Recent progress has been made, however, in theoretical treatments of preferred local structure in "hard" systems, or those governed solely by entropy. In these systems, there are no forces between particles, and instead their interactions are over the very short length scales relevant to volume exclusion. Free volume, then, becomes the relevant currency in these systems: the free volume available to any given particle dictates its vibrational entropy. Recent works by van Anders and Glotzer *et al.* considered free volume exchange in monodisperse systems of anisotropic hard particles, and found that systems maximizing their entropy via this mechanism exhibit preferences for certain pairwise configurations [36, 37]. These preferences can be expressed through the concept of statistically emergent forces, termed "directional entropic forces" [38].

Directional entropic forces can be quantified via a so-called potential of mean force and torque (PMFT), $F_{12}\left(\Delta\xi_{12}\right)$, associated with a pairwise configuration $\Delta\xi_{12}$ between any two particles in the system. $F_{12}$ is implicitly defined as follows [37]:

$$Z \equiv \int d\Delta\xi_{12} e^{-\beta F_{12}(\Delta\xi_{12})} \tag{1.1}$$

$Z$ is the partition function (where we are ignoring overall constants due to integration over momentum terms and normalization by any factors proportional to Planck's constant), and $\beta \equiv 1/k_B T$. $F_{12}\left(\Delta\xi_{12}\right)$ controls the contribution of the state characterized by $\Delta\xi_{12}$ to the partition function; when it is lower, the contribution is greater, implying that the state characterized by $\Delta\xi_{12}$ contributes more microstates

to Z.

Van Anders *et al.* explored the physical meaning of $F_{12}(\Delta\xi_{12})$ by decomposing it into contributions from (i) the particle pair with configuration $\Delta\xi_{12}$ and (ii) the surrounding sea of particles. Mathematical detail can be found in Appendix A; in general, the authors found that $F_{12}$ is minimized by some $\Delta\xi_{12}$ in a density-dependent manner according to a trade-off between increasing the free volume available to the particle pair, thereby increasing the configurational entropy of the pair, and packing the pair in a locally dense fashion, thereby increasing the configurational entropy of the sea of particles surrounding the pair. If particles are highly faceted, for example, they tend to align face-to-face with their neighbors at suitably high densities, as this pair arrangement strikes the best balance between the aforementioned free volume considerations. The authors then computed $F_{12}(\Delta\xi_{12})$ for a variety of hard-particle systems, and showed that even at intermediate packing fractions it has relative minima that can be on the order of a few $k_BT$. Thus, directional entropic forces associated with specific pair configurations seem to be powerful enough to direct self-assembly in certain systems of hard anisotropic particles.

## 1.4 Outline

On a pairwise level, then, locally dense packings are of significant import in the physics of self-assembly of hard particle systems. Van Anders *et al.* hypothesize that assembly in these systems amounts to nature solving a few-body problem, i.e. the maximization of the local density of a subset of particles [37].

This thesis tackles two broad lines of inquiry related to this hypothesis. The first is, how does the interplay between hard particle shape and spherical confinement influence cluster structure? We were inspired to ask this question by considering locally dense packing on intermediate length scales, i.e. for several particles. We hypothesize that a spherical volume is a zeroth-order approximation of the local environment for

a dense fluid on intermediate length scales, and generate a library of dense cluster structures of hard, faceted particles, packed inside spherical containers, to serve as potential candidates for motifs found in associated hard particle systems during self-assembly. Moreover, dense particle packing in a confining volume generally remains a rich, largely unexplored problem, despite applications in blood clotting, plasmonics, industrial packaging and transport, colloidal molecule design, and information storage. We use Monte Carlo simulation methods to find putative densest clusters of the Platonic solids in spherical confinement, for up to $N = 60$ constituent polyhedral particles. We find that densest clusters exhibit a wide variety of point group symmetries. For many $N$ values, icosahedra and dodecahedra form clusters that resemble sphere clusters. These common structures are layers of optimal spherical codes [39] in most cases, a surprising fact given the significant faceting of the icosahedron and dodecahedron. We also investigate cluster density as a function of $N$ for each particle shape, and find especially dense clusters at so-called "magic numbers" of constituent particles. Finally, we find that the densest tetrahedron cluster across all investigated values of $N$ is also a prominent motif in the self-assembled structure of tetrahedra, the dodecagonal quasicrystal. This suggests that, for tetrahedra, self-assembly may favor the formation of local structures that pack densely inside a sphere.

Our second line of inquiry relates to how local structure changes as hard particle shape is perturbed. In particular, we are interested in why slight changes in particle shape, which necessarily influence local structure, sometimes result in assembly failure and consequent glass formation, rather than crystallization. We explore the role of locally favored structural motifs in glass formation by examining the glass transition in an extended alchemical space, or a space containing systems with modified constituent particle attributes. We investigate a family of monatomic systems of hard particles of related polyhedral shapes via Monte Carlo simulation, and show that assembly failure in these systems arises from a multiplicity of competing local

particle environments, each of which is prevalent in – and predictable from – nearby ordered structures in alchemical space. We provide evidence that competition among local particle environments prevents crystallization by artificially tuning the presence of competing motifs to promote or disrupt crystallization. Additionally, we show that systems escape regions of competition and consequently crystallize when allowed to thermodynamically explore alchemical space via alchemical Monte Carlo [40].

Finally, we demonstrate that fragility, a technologically relevant measure of glass-forming ability, is dependent on system location in alchemical space, and thus can be tuned by changing particle shape. This study demonstrates the power of considering alchemical space in questions of local structure, self-assembly and its failure; in addition, we contribute to the body of literature probing the long-sought nature of the relationship between structure and dynamics in glass-forming systems.

The last chapter in this thesis details software I developed over the past few years to identify local structure in simulation trajectories. I discuss a variety of applications of that software, both in my projects and in other lab members' research.

# CHAPTER II

# Methods

## 2.1 Simulation methods

### 2.1.1 Monte Carlo sampling

Equilibrium statistical mechanics, at its core, is a quest to compute the partition function of any given system. For most biological or materials systems, whose phase space is extraordinarily high in dimension, the partition function is analytically intractable, and must instead be sampled computationally. Moreover, since the partition function contains states that are orders of magnitude more probable than others, it must be sampled intelligently, in a non-uniform manner, to compute ensemble averages that are accurate and computationally efficient [41]. Monte Carlo importance sampling is one such intelligent sampling method. In essence, microstates of the system are randomly sampled with a probability proportional to their Boltzmann factor. This ensures that the system is sampled according to its underlying statistical mechanical probability distribution, and that more probable states are sampled more often.

Particle positions and orientations evolve during a Monte Carlo simulation according to a trial-move update scheme, wherein particles are chosen randomly and then translated or rotated (in the case of non-spherical particles) with equal proba-

bility by a random amount within some range imposed by the size of the move type. Particle rotation and translation are decoupled from each other, to enable the most agnostic sampling of phase space. Additionally, move sizes are sometimes tuned over the course of the simulation, to facilitate an exploration of phase space that is computationally efficient. Any move from state $o$ to state $n$ is accepted with a probability $acc_{o\to n}$ given by the standard Metropolis criterion [41]:

$$acc_{o\to n} = \min\left(1, \frac{e^{-\beta U(n)}}{e^{-\beta U(o)}}\right) \tag{2.1}$$

$U(s)$, where $s = \{o, n\}$, is the potential energy of state $s$. This acceptance probability formulation ensures that the system obeys detailed balance, where the average number of accepted trial moves from state $o$ to state $n$ equals the average number of accepted trial moves from state $n$ to state $o$ [41]. In practice, for hard particle systems with no interactions aside from excluded volume, this means that moves are rejected if they result in any particle overlaps (since this results in an infinite energy for the configuration), and accepted otherwise (since this results in zero energy for the configuration).

### 2.1.2 The isobaric ensemble with confinement constraints

In the chapter of this thesis that discusses results for packing clusters of polyhedral particles in spherical confinement, we use traditional Monte Carlo sampling methods in the isobaric ensemble, with the additional constraint that we reject moves if they result in any particle overlaps or the presence of a portion of any particle outside the spherical container. Due to their faceting, polyhedra are fully encased in the container if all their vertices are inside the container. Spheres are fully encased in the container as long as their radial distance from the container center remains within a small tolerance of $(R_{circ} - R)$, where $R_{circ}$ is the container radius and $R$ is the particle radius.

Container resize moves occur with a probability equal to $1/(N+1)$, where $N$ is the number of particles in the system. During the run, simulation parameters are tuned such that particle translation, particle rotation, and container resize acceptance rates are approximately 0.2. (We found an acceptance rate of 0.2 to be near optimal in similar Monte Carlo implementations, so we adopted this as a convention.) Container shrinking moves are always accepted provided that they do not cause any particle overlaps and that confinement is maintained, whereas container expansion moves are accepted with a probability

$$P_{o\to n} = \exp\left[-\beta p\left(V_n - V_o\right) + N\log\left(V_n/V_o\right)\right] \tag{2.2}$$

where $V_n$ is the new container volume, $V_o$ is the old container volume, and $p$ is the pressure of the system. This criterion can be derived by considering the analytical form of the partition function in the isobaric ensemble in the thermodynamic limit, where a small subsystem is considered to be in equilibrium with a larger bath of ideal gas particles at some pressure $p$, and volume exchange between the subsystem and the bath occurs in equilibrium [41]. In our case, the small subsystem is the spherical container and its confined particles. Container resizing consists of rescaling the container radius and is accompanied by identical rescaling of all particle positions with respect to the container center.

### 2.1.3 The alchemical ensemble

In the section of this thesis pertaining to the role of local structure in assembly failure, we also use Monte Carlo sampling in the so-called alchemical ensemble, as developed and utilized in earlier works [40, 42–44]. This sampling technique is implemented in a branch of our in-house HPMC software package [45].

This method extends the partition function in the following manner:

$$Z = \sum_{\sigma} e^{-\beta(H_\sigma - \mu N \alpha)} \tag{2.3}$$

$\sigma$ counts over microstates, $H_\sigma$ is the Hamiltonian evaluated for microstate $\sigma$, and the two additional parameters $\mu$ and $\alpha$ extend the ensemble. $\alpha$, the "alchemical" parameter, is a generalized displacement that represents a modified particle attribute. (In the discussion that follows, all systems are assumed monatomic, and all particles have identical values of $\alpha$.) $\alpha$ is scaled by $N$, the number of particles in the system, so that it is an intensive variable. $\mu$ is the generalized force associated with this generalized displacement; it is the "alchemical potential" of the system. It gives the change in free energy that the system experiences when $\alpha$ changes. The sum over microstates in this ensemble is then:

$$\sum_{\sigma} = \int d\alpha d\boldsymbol{r}^N d\boldsymbol{p}^N dq^N d\boldsymbol{L}^N \tag{2.4}$$

The integral contains the usual position and momentum terms, with additional sums over orientations and angular momenta since we typically sample particles of anisotropic shape, and an additional sum over the alchemical parameter $\alpha$. We can integrate out over momenta and write the partition function as

$$Z \sim \int d\alpha d\boldsymbol{r}^N dq^N (\det I_\alpha)^{N/2} e^{-\beta(U_\alpha - \mu N \alpha)} \tag{2.5}$$

The integral over angular momenta produces the term $(\det I_\alpha)^{N/2}$ inside the integral. It cannot be taken outside of the integral because the moment of inertia tensor, $I_\alpha$, now may depend on the alchemical parameter $\alpha$. The probability of observing a microstate with alchemical parameter $\alpha$ is thus proportional to $(\det I_\alpha)^{N/2}$. (Note also that the potential energy of the system, $U_\alpha$, may depend on the alchemical parameter.)

Importance sampling in this extended ensemble now must include random moves

in $\alpha$. We can use a Metropolis-like acceptance probability for moving from alchemical parameter $\alpha_o$ to alchemical parameter $\alpha_n$ that satisfies detailed balance:

$$acc_{o\to n} = \min\left(1, \frac{(\det I_{\alpha_n})^{N/2} e^{-\beta(U_{\alpha_n} - \mu N \alpha_n)}}{(\det I_{\alpha_o})^{N/2} e^{-\beta(U_{\alpha_o} - \mu N \alpha_o)}}\right) \tag{2.6}$$

In the simulations in this thesis, we set $\mu = 0$; effectively, we sample the microstates for which the free energy is a minimum with respect to $\alpha$. Then, the system is free to move about in alchemical space without bias to minimize its free energy via standard configurational changes. In this case, the Metropolis-like acceptance probability is written as:

$$acc_{o\to n} = \min\left(1, \frac{(\det I_{\alpha_n})^{N/2} e^{-\beta U_{\alpha_n}}}{(\det I_{\alpha_o})^{N/2} e^{-\beta U_{\alpha_o}}}\right) \tag{2.7}$$

## 2.2 Characterization of local particle environments

Throughout my dissertation, I developed several methods of characterizing local environments in systems of anisotropic particles. These methods target local structure on a variety of length scales, and operate on the set of particle positions and orientations. Details of the methods are fleshed out in the following sections.

### 2.2.1 Pairwise configurations

I analyzed pairwise configurations of particles when characterizing the local structure of hard particle glass-formers as detailed in Section IV. A configuration of two anisotropic particles can be fully characterized in a rotationally and translationally invariant manner if the particles' relative displacement (a vector) and relative misorientation (a unit quaternion) are captured. Thus, six scalars are required to fully characterize a configuration of just two particles. This is already a rather high-dimensional space; below, we characterize pairwise configurations using just two scalars, in an ef-

fort to lower this dimensionality. The particle pairs we characterize via this method are pairs of truncated polyhedra, where polyhedron faces, truncated edges, and truncated vertices are all particle facets. To identify the motif composed of particle $i$ and its nearest neighbor, particle $j$, we use two parameters. The first is associated with the "connection type" ($c_{ij}$, hereafter $c$) between $i$ and $j$. We say $i$ is "face-connected" ($c = f$) to $j$ if particle $i$'s face is the closest feature to the connection vector $\boldsymbol{r}_{ij}$ (from the center of $i$, $\boldsymbol{r}_i$, to the center of $j$, $\boldsymbol{r}_j$), $i$ is "edge-connected" ($c = e$) to $j$ if $i$'s (truncated) edge is closest, or $i$ is "vertex-connected" ($c = v$) to $j$ if $i$'s (truncated) vertex is closest to the connection vector. To calculate the connection type, we consider first the non-truncated polyhedron $i_{poly}$ located at $\boldsymbol{r}_i$ and oriented identically to $i$. We find the unit vectors $\{\hat{\boldsymbol{f}}_i\}$ that point from $\boldsymbol{r}_i$ to the faces of $i_{poly}$, the unit vectors $\{\hat{\boldsymbol{e}}_i\}$ that point from $\boldsymbol{r}_i$ to the edges of $i_{poly}$, and the unit vectors $\{\hat{\boldsymbol{v}}_i\}$ that point from $\boldsymbol{r}_i$ to the vertices of $i_{poly}$. We then find $\cos\gamma_f \equiv \max(\hat{\boldsymbol{r}}_{ij} \cdot \hat{\boldsymbol{f}}_i)$, $\cos\gamma_e \equiv \max(\hat{\boldsymbol{r}}_{ij} \cdot \hat{\boldsymbol{e}}_i)$, and $\cos\gamma_v \equiv \max(\hat{\boldsymbol{r}}_{ij} \cdot \hat{\boldsymbol{v}}_i)$. Motifs are categorized as face-connected if $\gamma_f = \min(\gamma_f, \gamma_e, \gamma_v)$, or edge- or vertex-connected if $\gamma_e$ or $\gamma_v$ are the minimum angles, respectively.

Motifs are further distinguished by their relative misorientation $\theta_{ij}$ (hereafter $\theta$), the angle of rotation required to orient $j$ identically to $i$. In calculating $\theta$, we take particle symmetry into account: each $\theta$ is actually the minimum of the set of equivalent angles $\{\tilde{\theta}\}$, found by permuting through all possible pairs of equivalent particle orientations according to the particles' rotation group. This group is the chiral tetrahedral point group **23** or chiral octahedral point group **432** for the polyhedra characterized by this method.

We categorize pairwise motifs by combining the connection type $c$ with the relative misorientation $\theta$ via a joint discrete probability distribution $P_{obs}(c, \theta_k)$:

$$P_{obs}(c, \theta_k) = \frac{N_{obs}(c, \theta_k)}{\sum_c \sum_{k=1}^{n_{bins}} N_{obs}(c, \theta_k)} \tag{2.8}$$

$N_{obs}(c, \theta_k)$ is the number of particles observed with connection type $c$ and misorientation $\theta$ in a bin centered at $\theta_k$ with some width $\Delta\theta$. There are $n_{bins}$ such bins for each connection type.

To determine statistically significant trends in this distribution, we must normalize by the equivalent joint discrete probability distribution $P_{rand}(c, \theta_k)$ for an "ideal gas" of non-interacting particles of the same symmetry group. The connection type is unrelated to the misorientation for non-interacting particles, so these probabilities can be considered separately: $P_{rand}(c, \theta_k) = P_{rand}(c)P_{rand}(\theta_k)$. The negative log of the joint probability distribution, normalized with respect to an ideal gas, is an especially useful quantity:

$$-\log P(c, \theta_k) = -\log \frac{P_{obs}(c, \theta_k)}{P_{rand}(c, \theta_k)} \tag{2.9}$$

For each connection type, $\log P_{rand}(\theta_k)$ displaces $-\log P_{obs}(c, \theta_k)$ in the same misorientation-dependent manner, while $\log P_{rand}(c)$ displaces $-\log P_{obs}(c, \theta_k)$ by some connection-dependent scalar over all misorientations. When $-\log P(c, \theta_k) < 0$, we observe a connection type $c$ and misorientation $\theta_k$ that is more probable than in the ideal gas. Different pairwise motifs can be identified according to $\theta$ ranges that correspond to local minima, or basins, in $-\log P(c, \theta_k)$. In the remainder of this thesis, the discrete $\theta_k$ is labeled as the continuous $\theta$ for simplicity.

We computed the random $\theta$ probability distribution $P_{rand}(\theta)$ for both chiral tetrahedral and chiral octahedral point groups by generating 10 million random pairs of orientations and computing the minimum rotation angle $\theta$ between them with respect to the associated underlying rotation group, as detailed earlier. We computed $P_{rand}(c)$ for the chiral tetrahedral point group by generating 2.5 million pairs of particles of appropriate symmetry with random orientations and a random unit displacement

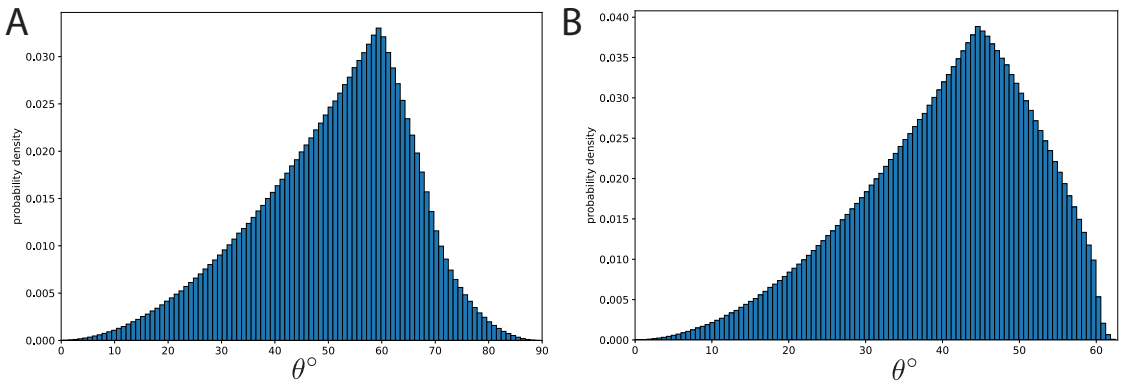


Figure 2.1: Random $\theta$ probability distributions $P_{rand}(\theta)$ for the (a) chiral tetrahedral point group and (b) chiral octahedral point group.

vector between them. We then determined connection types for these pairs in the manner detailed above. $P_{rand}(c)$ for the chiral octahedral point group was not ultimately necessary for our analysis, but could be found in a similar manner. Fig. 2.1 shows the generated $P_{rand}(\theta)$ for the chiral tetrahedral and chiral octahedral point groups.

We note that analytical tools developed by the polycrystalline materials community [46–48] can be brought to bear on this problem, since $P_{rand}(\theta)$ for any underlying particle symmetry group maps to the random grain boundary misorientation angle distribution for that same underlying (crystal grain) symmetry group. For our purposes, however, it was sufficient to numerically calculate $P_{rand}(\theta)$. See Appendix D for more detail regarding analytical treatments of misorientation spaces.

### 2.2.2 Multi-particle configurations

Throughout my dissertation, I also found it useful to characterize particle environments using particle position data only. Particle environments in this case are defined as sets of vectors pointing from the center of each particle in the system to the centers of some number of its nearest neighbors. Multi-particle configurations defined in this way can be analyzed in real space and in Fourier space.

#### 2.2.2.1 Analysis in real space

I utilized a real-space analysis of local particle environments to characterize crystalline domains and other motifs of interest in various systems in several projects over the course of my thesis. This analysis uses an "environment matching" scheme, which I developed and implemented in *freud* [49], our group's open-source simulation analysis package. Applications of the analysis, by myself and various collaborators, are discussed in detail in Section VI. The scheme is described in the following paragraphs.

We define particle $i$'s environment as the set of vectors $\{\boldsymbol{r}_{im}\}$, where $\boldsymbol{r}_{im}$ points from the center of particle $i$ to the center of particle $m$, and $m$ is an index over $i$'s $M$ nearest neighbors. Particle $j$'s environment is defined as the set of vectors $\{\boldsymbol{r}_{jm'}\}$, where $\boldsymbol{r}_{jm'}$ points from the center of particle $j$ to the center of particle $m'$ and $m'$ loops over $j$'s $M$ nearest neighbors. We then compare the environments of particle $i$ and particle $j$ by attempting to match these sets of vectors: $j$'s environment "matches" $i$'s environment if we can find a rotation $R$ and a one-to-one mapping such that $|\boldsymbol{r}_{im} - R\boldsymbol{r}_{jm'}| < t$ for every mapping pair $(m, m')$ for some threshold $t$. This mapping can either be rotationally sensitive, in which case $R$ is set to the identity $\hat{I}$ and identical environments of different orientations are regarded as distinct, or rotationally invariant, in which case an attempt to find the rotation $R$ that minimizes the root-mean-squared displacement (RMSD) between the environments is made prior to the attempt to find the more restrictive mapping according to the threshold.

The problem of finding $R$ and an appropriate one-to-one mapping is very non-trivial, and is known as the "registration" problem in various image recognition communities. Wolfgang Kabsch developed a solution to one half of this problem in 1976 [50]: the eponymous Kabsch algorithm finds the optimal rotation to minimize the RMSD between two *labelled* sets of points centered about the origin. In other words, each point in each set is distinguishable and labelled by its position in the set, and the RMSD minimized by the Kabsch algorithm is an average over every pair of points at

the same position in each set. The real issue in finding the RMSD between *indistinguishable* point sets, then, is one of permutation. One could, theoretically, compare every permutation of one point set against the other point set and use the Kabsch algorithm to find the minimum RMSD across all permutations. However, the number of permutations of $N$ points is $N!$, meaning that, very quickly, the number of calculations required to exhaustively solve the problem combinatorially explodes. Paul M. Dodd, a member of our group, implemented a brute-force solution to the registration problem that I incorporated into our environment-matching scheme – I will briefly outline this solution and the Kabsch algorithm in the following paragraphs.

First, I will outline Wolfgang Kabsch's solution to minimizing the RMSD between two labelled sets of points. This explanation largely follows that laid out by Lydia E. Kavraki in her online bioinformatics class "Geometric Methods in Structural Computational Biology" [51].

Let $\{\boldsymbol{x}_n\}$ and $\{\boldsymbol{y}_n\}$, $n = 1 \dots N$, be two sets of vectors centered at the origin. Let $U$ be a rotation matrix that acts on $\{\boldsymbol{x}_n\}$. The mean-squared displacement between these vector sets is

$$E = \frac{1}{N} \sum_n |U\boldsymbol{x}_n - \boldsymbol{y}_n|^2 \tag{2.10}$$

We can re-write the above as a matrix equation, where $X$ and $Y$ are $3 \times N$ matrices of all vectors in $\{\boldsymbol{x}_n\}$ and $\{\boldsymbol{y}_n\}$ respectively:

$$
\begin{aligned}
NE &= \sum_n \sum_{k=1}^{3} (UX - Y)_{kn} (UX - Y)_{kn} \\
&= \sum_n \sum_{k=1}^{3} (UX - Y)^T_{nk} (UX - Y)_{kn} \\
&= \mathrm{Tr} \left[ (UX - Y)^T (UX - Y) \right] \\
&= \mathrm{Tr}\, X^T U^T U X + \mathrm{Tr}\, Y^T Y - 2\, \mathrm{Tr}\, Y^T U X \\
&= \mathrm{Tr}\, X^T X + \mathrm{Tr}\, Y^T Y - 2\, \mathrm{Tr}\, Y^T U X
\end{aligned} \tag{2.11}
$$

The fourth line follows from the third by noting that the trace of a matrix equals the trace of its transpose. Minimizing $E$, therefore, means choosing $U$ such that $\mathrm{Tr}\, Y^T U X$ is maximal. This quantity can be thought of as the overlap between the rotated set of vectors $UX$ and the unrotated set $Y$. If bra-ket notation is easier to intuit (as it is for me), each element of the trace is equivalent to $\langle \boldsymbol{y}_n | U | \boldsymbol{x}_n \rangle$. We find $U$ by performing a singular value decomposition $XY^T = VSW^T$, where $V$ and $W^T$ are orthonormal matrices of the left and right eigenvectors of $XY^T$, and $S$ is a diagonal matrix of its eigenvalues in decreasing order.

$$
\begin{aligned}
\mathrm{Tr}\, Y^T U X &= \mathrm{Tr}\, X Y^T U \\
&= \mathrm{Tr}\, V S W^T U \\
&= \mathrm{Tr}\, S W^T U V
\end{aligned} \tag{2.12}
$$

Since $S$ is a diagonal matrix, the above trace is a (weighted) sum over the diagonal elements of $W^T U V$. $W^T U V$ is an orthonormal matrix because it is a product of orthonormal matrices, and elements of $S$ are never negative, so the trace is maximal when $W^T U V = I$, the identity matrix. $I$ is the orthonormal matrix with maximal

trace. Thus, the $U$ that minimizes $E$ is given by:

$$W^T U V = I$$
$$U = W V^T \tag{2.13}$$

If $U$ found above is an improper rotation, meaning $\det U = -1$, we must instead use the next best (proper) rotation by setting the final column of $W^T U V$ to be $(0, 0, -1)$ rather than $(0, 0, 1)$. This will insure that the next best $U$ is a proper rotation, and subtracts the smallest element of $S$ during the trace, rather than adding it. The optimal proper rotation $U$ can be concisely written as:

$$U = W \begin{pmatrix} 1 & 0 & 0 \\ 0 & 1 & 0 \\ 0 & 0 & d \end{pmatrix} V^T \tag{2.14}$$

with $d = \text{sign}\left(\det XY^T\right)$.

Thus, given the order of $\{\boldsymbol{x}_n\}$ and $\{\boldsymbol{y}_n\}$, finding the minimal RMSD via the above method is actually rather trivial. The difficult step is finding the proper order of $\{\boldsymbol{x}_n\}$ and $\{\boldsymbol{y}_n\}$. Below I outline Paul M. Dodd's brute-force strategy for finding this proper order.

1. 3 random points are chosen from the set $\{\boldsymbol{y}_n\}$
2. 3 points are chosen from the set $\{\boldsymbol{x}_n\}$
3. $U$ is found that minimizes the RMSD between these two subsets of 3 vectors each
4. The RMSD between $UX$ and $Y$, the full sets of points, is found. The RMSD is

computed over the pairing of points found by looping over each point in $\{\boldsymbol{y}_n\}$ and pairing it with the nearest point in $\{U\boldsymbol{x}_n\}$ that is not already matched to any other point in $\{\boldsymbol{y}_n\}$. (This method is not guaranteed to find the absolutely minimal RMSD; to do that, one would have to implement a solution to the well-known assignment problem.)

* Steps 2-4 are repeated either until the RSMD between the full sets falls below 1e-6, or until every possible combination and permutation of 3 points in $\{\boldsymbol{x}_n\}$ has been considered.

5. The returned RMSD (and optimal rotation and pairing) is the minimal one over all those calculated in the previous step.

Using three vectors above is reasonable because many particle environments in a typical system are misaligned by essentially a rigid rotation. The stricter criterion of all properly rotated and paired vectors having a displacement below some threshold is then applied to determine if these vector sets match. If there was no registration by the above algorithm, the pairing is rather more uninformed than that found in Step 4: each point in $\{\boldsymbol{y}_n\}$ is looped over, and paired with any unpaired point in $\{\boldsymbol{x}_n\}$ if the displacement between the points is below the threshold. If a complete 1-1 map is found this way, then the point sets match.

#### 2.2.2.2 Analysis in Fourier space

I analyzed multi-particle configurations of particles in Fourier space when characterizing clusters of polyhedra in spherical confinement as detailed in Section III. To perform this analysis, I computed bond order parameters [52], first developed by Paul J. Steinhardt and colleagues in the early 1980s to identify local icosahedral order in liquids and glasses, and used them to build associated shape descriptors [53] for cluster configurations. This technique is described in the following paragraphs.

For a given $l$, the bond order parameter for a set of $N$ points constituting cluster $i$ is

$$Q_l^i \equiv \left[ \frac{4\pi}{2l+1} \sum_{m=-l}^{l} \left| \frac{1}{N} \sum_{j=1}^{N} Y_l^m \left( \boldsymbol{r_j} \right) \right|^2 \right]^{1/2} \tag{2.15}$$

where $\boldsymbol{r_j}$ is the vector pointing from a reference point to point $j$, and $Y_l^m$ is the spherical harmonic associated with angular momentum number $l$ and magnetic quantum number $m$. We use the centroid of cluster $i$ as our reference point.

Bond order parameters are rotationally-invariant combinations of the Fourier components of point distributions on the surface of a unit sphere. To see this, consider first the simpler example of a distribution of points on the perimeter of a unit circle. This is a one-dimensional distribution, where all points can be fully characterized by their polar angle $\theta$. Any distribution on the circle, $f(\theta)$, can be written in terms of basis vectors of sines and cosines as

$$f\left(\theta\right) = \frac{1}{\sqrt{2\pi}} \sum_{l=0} \psi_l e^{-il\theta} \tag{2.16}$$

$\psi_l$ is the (complex) Fourier coefficient corresponding to $l$, or the strength of the distribution for frequency $l$. It can be found in the usual manner, by taking advantage of the orthonormality of the basis vectors $\frac{1}{\sqrt{2\pi}} e^{-il\theta}$:

$$\begin{aligned}
\frac{1}{\sqrt{2\pi}} \sum_{l'=0} \psi_{l'} e^{-il'\theta} &= f\left(\theta\right) \\
\frac{1}{2\pi} \int d\theta \sum_{l'=0} \psi_{l'} e^{-il'\theta} e^{il\theta} &= \frac{1}{\sqrt{2\pi}} \int d\theta f\left(\theta\right) e^{il\theta} \\
\sum_{l'=0} \psi_{l'} \delta_{ll'} &= \frac{1}{\sqrt{2\pi}} \int d\theta f\left(\theta\right) e^{il\theta} \\
\psi_l &= \frac{1}{\sqrt{2\pi}} \int d\theta f\left(\theta\right) e^{il\theta}
\end{aligned} \tag{2.17}$$

Consider that $f(\theta)$ is the discrete probability density distribution of $N$ points distributed with angles $\{\theta_j\}$ about the unit circle, such that $\int d\theta f(\theta) = 1$:

$$f(\theta) = \frac{1}{N}\sum_{j=1}^{N}\delta(\theta - \theta_j)$$

Then,

$$\begin{aligned}\psi_l &= \frac{1}{\sqrt{2\pi}}\int d\theta f\left(\theta\right) e^{il\theta} \\ &= \frac{1}{\sqrt{2\pi}}\int d\theta \frac{1}{N}\sum_{j=1}^{N}\delta(\theta - \theta_j)e^{il\theta} \\ &= \frac{1}{N\sqrt{2\pi}}\sum_{j=1}^{N} e^{il\theta_j}\end{aligned} \tag{2.18}$$

Consider the re-scaling $\psi_l \rightarrow \sqrt{2\pi}\psi_l$. These re-scaled coefficients have a very physically intuitive meaning [54]. $\psi_0 = 1$ is just a reflection of our normalization choice. $\psi_1 = \frac{1}{N}\sum_{j=1}^{N} e^{i\theta_j}$, however, is the pattern's centroid in the complex plane. In general, $\psi_l = \frac{1}{N}\sum_{j=1}^{N} e^{il\theta_j}$ can be thought of as the centroid of the pattern formed by multiplying every angle by $l$. If the pattern is $l$-fold rotationally symmetric, then any $\theta_j$ in the pattern corresponds to an $l$-membered set $\{\theta_{j'}\}$ given by $\theta_{j'} = \theta_j + 2\pi m/l$ for $0 \leq m < l$. For any member of this set, $e^{il\theta_{j'}} = e^{il\theta_j}e^{i2\pi m} = e^{il\theta_j}$. Thus, $q_l$ can be re-written as:

$$\begin{aligned}\psi_l &= \frac{1}{N}\sum_{j=1}^{N} e^{il\theta_j} \\ &= \frac{l}{N}\sum_{k=1}^{N/l} e^{il\theta_k}\end{aligned}$$

$k$ counts over the unique values of $\theta$ in the distribution under symmetry. $\psi_l$ thus has a larger signal if the pattern is $l$-fold rotationally symmetric, due to the above constructive interference.

$\psi_l$, the centroid of the pattern formed by multiplying every angle by $l$, is in general not a point at the origin of the complex plane. Thus, it has some angular component itself, and is dependent on global rotations of the whole pattern, i.e. if $\theta_j \to \theta_j + \alpha$ for every value $j$ and some displacement angle $\alpha$. However, the distance between the centroid and the origin, $|\psi_l|$, is rotationally-invariant. This quantity, $q_l \equiv |\psi_l|$, is the one-dimensional analogue of Steinhardt's higher-dimensional bond-orientational order parameter.

Steinhardt's bond-orientational order parameter characterizes a set of bonds typically pointing from the center of some particle to the centers of its nearest neighbors. These bonds, projected onto the surface of a unit sphere, are just a distribution of points on the surface of that sphere. This distribution can be written as a superposition of spherical harmonics, the analogous orthonormal basis vectors to $\frac{1}{\sqrt{2\pi}} e^{il\theta_j}$:

$$f(\theta, \phi) = \sum_{l=0} \sum_{m=-l}^{l} q_{lm} Y_{lm}^*(\theta, \phi) \tag{2.19}$$

We again let $f(\theta, \phi)$ be a discrete probability density distribution characterizing $N$ points on the surface of the unit sphere:

$$f(\theta, \phi) = \frac{1}{N} \sum_{j=1}^{N} \delta(\Omega - \Omega_j)$$

$\Omega_j$ is the solid angle of the unit sphere at which point $j$ is located. We use the orthonormality of the spherical harmonics to find $q_{lm}$:

$$\sum_{l'} \sum_{m'=-l'}^{l'} q_{l'm'} Y^*_{l'm'}(\theta,\phi) = f(\theta,\phi) \tag{2.20}$$

$$\int d\Omega \sum_{l'} \sum_{m'=-l'}^{l'} q_{l'm'} Y^*_{l'm'}(\theta,\phi) Y_{lm}(\theta,\phi) = \int d\Omega f(\theta,\phi) Y_{lm}(\theta,\phi)$$

$$\sum_{l'} \sum_{m'=-l'}^{l'} q_{l'm'} \delta_{ll'} \delta_{mm'} = \int d\Omega f(\theta,\phi) Y_{lm}(\theta,\phi)$$

$$q_{lm} = \int d\Omega f(\theta,\phi) Y_{lm}(\theta,\phi)$$

$$= \int d\Omega \frac{1}{N} \sum_{j=1}^{N} \delta(\Omega - \Omega_j) Y_{lm}(\theta,\phi)$$

$$= \frac{1}{N} \sum_{j=1}^{N} Y_{lm}(\theta_j,\phi_j)$$

We can then build a rotationally-invariant parameter, $Q_l$, out of these $q_{lm}$ values, as we did to build $q_l$ out of $\psi_l$ in the one-dimensional case:

$$Q_l \equiv \left[ \frac{4\pi}{2l+1} \sum_{m=-l}^{l} |q_{lm}|^2 \right]^{1/2} \tag{2.21}$$

This normalization is useful because $\sum_m |q_{lm}|^2 \sim \frac{2l+1}{4\pi}$ due to the way the spherical harmonics are defined; thus the re-scaling by $\frac{4\pi}{2l+1}$ eliminates hidden $l$-dependence and in particular lets $Q_0 = 1$, in parallel to $q_0 = 1$ in the one-dimensional case.

Point clusters of a given symmetry have well-defined values of $Q_l$ for various $l$, due to constructive interference and consequent large signals in the Fourier coefficients, as explored in the one-dimensional case. In general, a vector of these order parameters at multiple values of $l$, $\{l_1, l_2 \ldots l_n\}$, acts as a signature for a particular distribution of points over the surface of a sphere. This vector constitutes a shape descriptor [53] characterizing a particular cluster $i$:

$$\boldsymbol{Q_i} = \left\langle Q^i_{l_1}, Q^i_{l_2}, \ldots Q^i_{l_n} \right\rangle \tag{2.22}$$

$\boldsymbol{Q_i}$ lies in $n$-dimensional space. Throughout this dissertation, we use the set of $l$ = (2, 3, ... 12) to calculate this vector.

To evaluate how well two different point configurations $i$ and $j$ match, we use the following quantity:

$$M_{dist}\left(i,j\right) \equiv 1 - \frac{|\boldsymbol{Q_i} - \boldsymbol{Q_j}|}{\sqrt{|\boldsymbol{Q_i}|^2 + |\boldsymbol{Q_j}|^2}} \tag{2.23}$$

This is effectively a normalized measure of the distance between two $Q$-vectors [53]: $M_{dist}\left(i,j\right)$ is 1 when $\boldsymbol{Q_i} = \boldsymbol{Q_j}$, and 0 when $\boldsymbol{Q_i}$ is perpendicular to $\boldsymbol{Q_j}$.

# CHAPTER III

# Clusters of polyhedra in spherical confinement

This chapter is adapted from Ref. [55], a publication in *Proceedings of the National Academy of Sciences* authored in 2016 by E.G. Teich, G. van Anders, D. Klotsa, J. Dshemuchadse, and S.C. Glotzer.

## 3.1 Packing in confinement

Phenomena as diverse as crowding in the cell [56, 57], DNA packaging in cell nuclei and virus capsids [58, 59], the growth of cellular aggregates [60], biological pattern formation [61], blood clotting [62], efficient manufacturing and transport, the planning and design of cellular networks [63], and efficient food and pharmaceutical packaging and transport [64] are related to the optimization problem of packing objects of a specified shape as densely as possible within a confining geometry, or packing in confinement. Packing in confinement is also a laboratory technique used to produce particle aggregates with consistent structure. These aggregates may serve as building blocks (or "colloidal molecules") in hierarchical structures [65, 66], information storage units [67], or drug delivery capsules [21]. Experiments concerning cluster formation via spherical droplet confinement [21, 68–74] are of special interest here. Droplets are typically either oil-in-water or water-in-oil emulsions, and particle aggregation is induced via the evaporation of the droplet solvent. Clusters may be

hollow (in which case they are termed "colloidosomes" [21]) or filled, depending on the formation protocol, and may contain a few [69] to a few billion [68] particles. Clusters of several metallic nanoparticles are especially intriguing given their ability to support surface plasmon modes over a range of frequencies [75]. The subwavelength scale of these clusters means that their optical response is highly dependent on their specific geometry [76]. Consequently, control over their structure enables control over their optical properties, with implications for cloaking [77], chemical sensing [78], imaging [79], non-linear optics [80], and the creation of so-called "meta-fluids" [81–83], among a host of other applications [84].

Additionally, the investigation of dense packings inside spheres offers a means by which to access locally dense particle configurations beyond pairwise arrangements. Pairwise local dense packing has been shown to be an important determinant of structure in dense fluids of hard particles [37], but the contribution of dense packing of multiple particles on intermediate length scales is less explored. Clusters of hard particles in spherical confinement may be candidates for preferred motifs in associated hard particle systems during self-assembly.

While some theoretical studies have addressed the confinement of anisotropic particles in one or two dimensions [85–89], a majority have focused on the confinement of spherical particles in one [90, 91], two [63, 92], and three [73, 93**?** –98] dimensions. There have also been studies of two-dimensional packings of circles [63, 64], ellipses [99–102], convex polygons [64], and other generalized two-dimensional objects [103]. However, to our knowledge, only a handful of studies have addressed three-dimensional dense packings of anisotropic particles inside a container. Of these, almost all pertain to packings of ellipsoids inside rectangular, spherical, or ellipsoidal containers [104–106], and only one investigates packings of polyhedral particles inside a container [107]. In that case, the authors used a numerical algorithm (generalizable to any number of dimensions) to generate densest packings of $N = (1 - 20)$ cubes

inside a sphere.

In contrast, the bulk densest packing of anisotropic bodies has been thoroughly investigated in three-dimensional Euclidean space [108–113]. This work has revealed insight into the interplay between packing structure, particle shape, and particle environment. Understanding the parallel interplay between shape and structure in confined geometries is both of fundamental interest and of relevance to the host of biological and materials applications just mentioned.

## 3.2 Putative densest packings via Monte Carlo simulation

We used Monte Carlo simulations to explore dense packings of an entire shape family, the Platonic solids, inside a sphere. The Platonic solids are a family of five regular convex polyhedra: the tetrahedron, cube, octahedron, dodecahedron, and icosahedron. Of these, all but the icosahedron are readily synthesized at nanometer scales, micron scales, or both; see for example [5–15, 86]. This set of shapes has a range of sphericity, as described by the isoperimetric quotient (IQ) of each polyhedron. $IQ \equiv 36\pi V^2/S^3$, where $V$ is polyhedron volume and $S$ is surface area. For spheres, $IQ = 1$, and for all other polyhedra, $0 < IQ < 1$ [114]. This quantity is the squared ratio of the volume of the polyhedron to the volume of a sphere with the same surface area. Since spheres maximize volume given any particular surface area, this quantity asymptotically approaches 1 as any polyhedron becomes increasingly "spherical."

For each polyhedron we generated and analyzed dense clusters consisting of $N = (4 - 60)$ constituent particles. We also generated dense clusters of hard spheres for the purposes of comparison. We found, for many $N$ values, that the icosahedra and dodecahedra pack into clusters that resemble sphere clusters, and consequently form layers of optimal spherical codes. For a few low values of $N$ the packings of octahedra and cubes also resemble sphere clusters. Clusters of tetrahedra do not. Our results, in contrast to those for densest packings in infinite space where particle shape sig-

nificantly affects packing structure [108, 110–112], suggest that the presence of the container suppresses the packing influence of particle shape at the range of $N$ studied. Spherical confinement provides a means by which to impose certain symmetries on anisotropic particles that otherwise might not pack like spheres. The imposed structures are a set of dense motifs that are robust against changes in particle shape. This result has implications for experimental applications in which the fabrication of highly spherical particles is difficult or undesirable, as in the case of several plasmonic applications [115–117].

We also examined cluster structure and density as they vary across each individual set of densest found packings and found a wide variety of cluster symmetries as $N$ varies. We note that in a spherical container, in contrast to the situation in infinite space described by Ulam's conjecture, spheres are not the worst packers of all convex bodies at small $N$. We additionally found that certain values of $N$, so-called "magic numbers," [118–121] correspond to especially high cluster densities of a given particle shape. These magic numbers, however, do not correspond to any particular cluster symmetry, indicating that especially dense clusters exist with a variety of symmetries and structures. Many of these structures are unachievable with densely-packed spheres, and are stabilized by a variety of contact types. They will be of interest to experimentalists who use clusters for plasmonics and other colloidal molecule applications.

## 3.3 Methods and protocols

### 3.3.1 Simulations

We used isobaric Monte Carlo simulations and specialized particle overlap checks with respect to a spherical container, as detailed in Section 2.1.2. For consistency, all particles were scaled such that they have equal circumscribing sphere radii. We ran

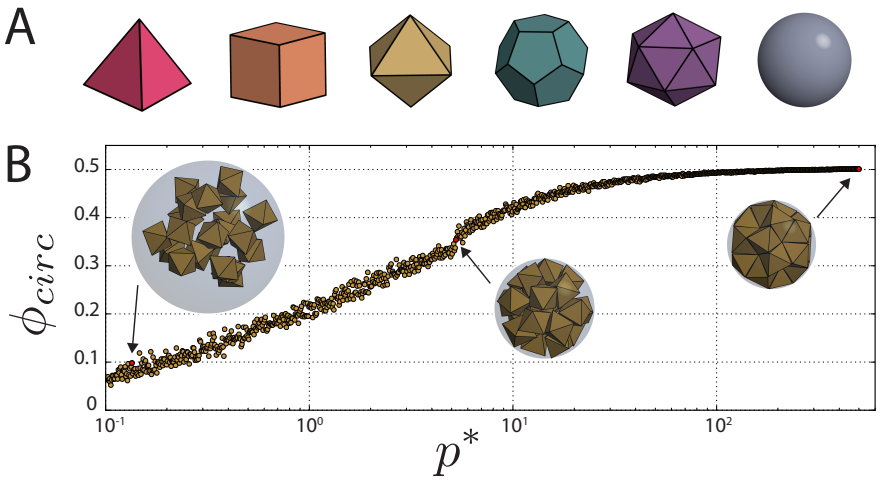


Figure 3.1: Overview of our methods. (a) The particle shapes studied: the Platonic solids and the sphere. (b) The evolution of the densest found 21-octahedron cluster via NPT compression in a spherical container. $p^*$ is the dimensionless pressure imposed on the system, and $\phi_{circ}$ is the density of the cluster. Insets are cluster images at $p^* = 0.135$, $p^* = 5.246$, and $p^* = 500$.

50 independent compression simulations at every (shape, $N$) state point, calculate the density for each of the resultant clusters via $\phi_{circ} \equiv NV_p/V_{circ}$, and chose the densest for further analysis. $V_p$ is the volume of a single particle and $V_{circ}$ is the volume of the container.

We induced increasing spherical confinement by raising dimensionless pressure exponentially from a minimum value of 0.1 to a maximum value of 500. Dimensionless pressure is defined here as $p^* \equiv \beta p l^3$, where $p$ is pressure and $l = R$ is the characteristic length scale in our systems. It is the particle radius for simulations involving spheres, while for simulations involving polyhedra it is the radius of their circumscribing sphere. The system was allowed to equilibrate for 1000 MC sweeps between pressure jumps. The total compression occurred over $10^7$ sweeps.

Fig. 3.1 summarizes our simulation method: part (a) displays the shapes studied, and part (b) shows a sample trajectory of cluster formation via our compression scheme. Inset images are snapshots of the cluster at indicated pressures. Fig. 3.2

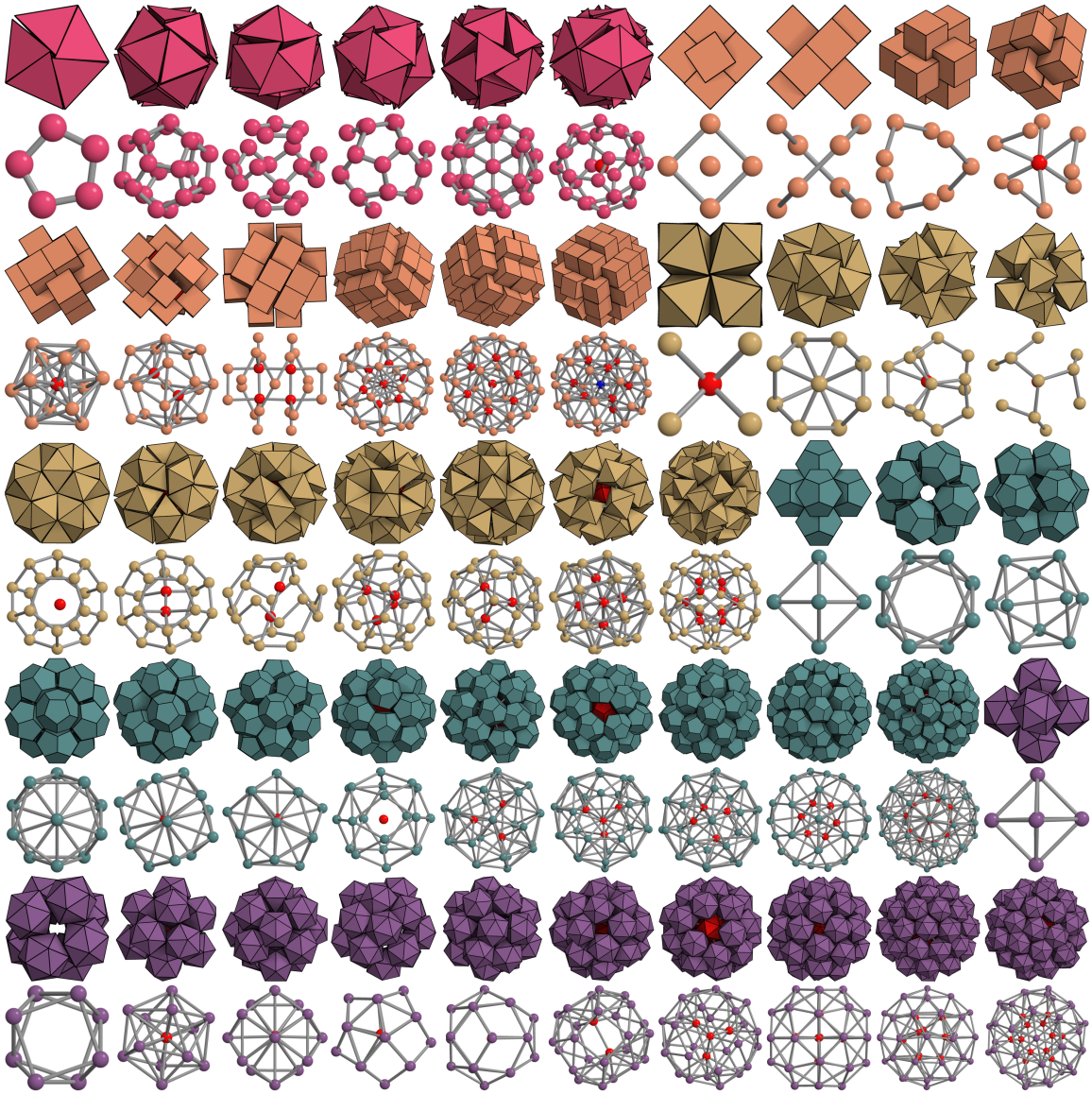

Figure 3.2: A selection of densest found clusters of the Platonic solids. $N$ increases from left to right for each particle shape. The screenshot of each cluster is accompanied by an image below showing its particle centers, with bonds drawn between neighboring particles at arbitrary distance cut-offs for clarity. Particles in next inner layers are colored red, while particles in innermost layers are colored blue. Whenever possible, clusters are displayed along an axis of symmetry.

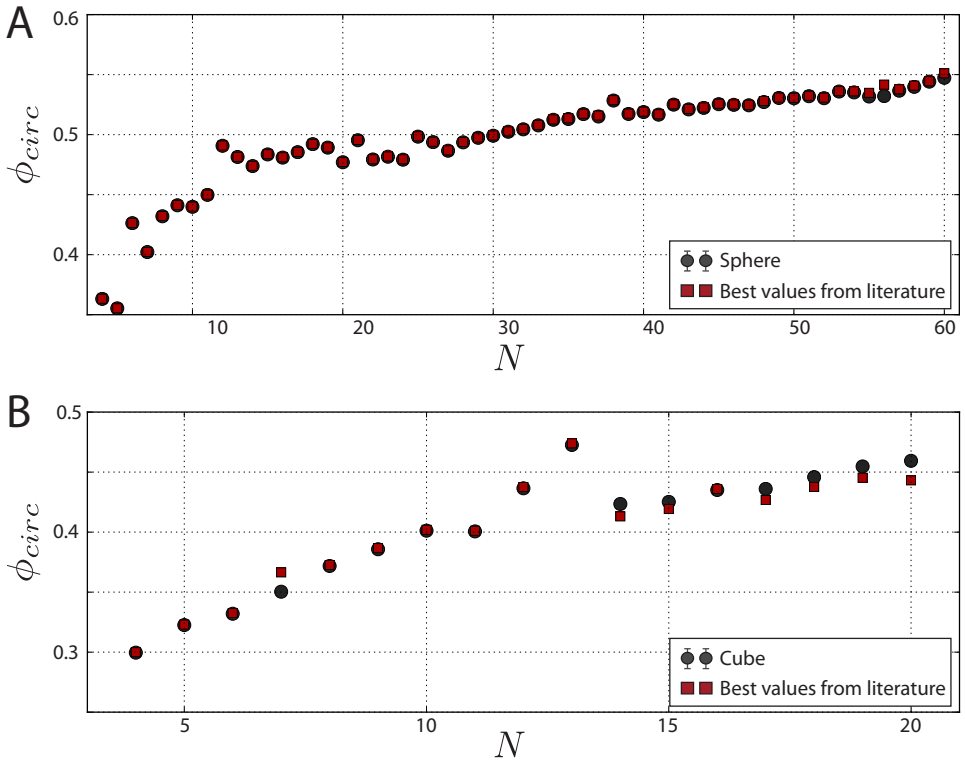


Figure 3.3: Validation of our method. Red squares are from densest known structures in the literature, and black circles represent our results. Vertical error bars are smaller than the data points, and indicate possible underestimation of $\phi_{circ}$ due to an overestimation of $R_{circ}$. (a) $\phi_{circ}$ for sphere clusters at $N = (4 - 60)$. Red squares are from Ref. [98]. (b) $\phi_{circ}$ for cube clusters at $N = (4 - 20)$. Red squares are from Ref. [107].

shows a sample of densest clusters found via this method, for a variety of constituent particle shapes and numbers.

As a validation of our method, we compare our results for $N = (4 - 60)$ sphere clusters to the literature results collected in Ref. [98] (Fig. 3.3A). Our methods produce densest sphere clusters for which $\Delta\phi_{circ} \equiv \left(\phi_{circ}^{lit} - \phi_{circ}^{us}\right)/\phi_{circ}^{lit}$ obeys $1.3 \times 10^{-4} < \Delta\phi_{circ} < 1.8 \times 10^{-2}$. $\phi_{circ}^{lit}$ are packing fractions of the densest clusters in the literature, while $\phi_{circ}^{us}$ are packing fractions of our densest generated clusters.

We also compare our results for $N = (4 - 20)$ cube clusters to clusters obtained in Ref. [107] (Fig. 3.3B). Our methods produce values of $\Delta\phi_{circ}$ for which $-3.7 \times 10^{-2} < \Delta\phi_{circ} < 3.0 \times 10^{-3}$, with the notable exception of the cluster of 7 cubes. In this case,

the densest cluster in the literature, a central cube surrounded by 6 cubes in face-face contact with it, is denser than our densest cluster by $\Delta\phi_{circ} \sim 4.4 \times 10^{-2}$. This value is about 15 times larger than the next largest value of $\Delta\phi_{circ}$. Although it is only about twice as large as the maximum value of $\Delta\phi_{circ}$ for our generated clusters of spheres, it occurs for a much lower value of $N$. The maximum value of $\Delta\phi_{circ}$ in the case of sphere clusters occurs at $N = 56$; at this system size, it is logical that our compression method may not be as well-equipped to find maximum cluster density as a numerical optimization, quasi-physical, or other dedicated algorithm, due to the high dimensionality of phase space. The high value of $\Delta\phi_{circ}$ at $N = 7$ cubes is somewhat surprising, by contrast, and can be explained by the fact that the denser cluster of cubes has a limited configuration space available to it at intermediate pressures during our simulation, and is thus disfavored with respect to other structural alternatives. See Appendix B for more details.

### 3.3.2 Cluster analysis

To quantify our structures and compare them with each other, we computed bond order parameters [52] and used them to build associated shape descriptors [53] for each cluster and each cluster layer in the manner detailed in Section 2.2.2.2. We then used variants of the parameter $M_{dist}(i, j)$, given by Eq. 2.23, to quantitatively compare clusters $i$ and $j$. We determined cluster structures to match if $M_{dist}(i, j) > 0.88$.

Imposing a strict cutoff value for $M_{dist}$, below which clusters are deemed structurally dissimilar for our purposes, inevitably results in an artificial oversimplification of the data. However, we needed to establish a cutoff in order to interpret our data objectively, without relying solely on potentially mistaken direct-eye observations of hundreds of dense clusters. To determine the cutoff $M_{dist} > 0.88$, we supplemented direct observations of cluster similarity with a comparison between $M_{dist}\,(i, j)$ and the root-mean-squared distance between certain sets of points $i$ and $j$.

We first observed that the set of particle centroids of most Platonic solid clusters looked similar to the set of sphere clusters for $M_{dist}$ in the range $0.9 \leq M_{dist} \leq 1$. This was a general observation, not true in some cases: some clusters looked quite non-identical by eye but gave a value of $M_{dist}$ greater than 0.9, while other clusters looked more similar but gave values of $M_{dist}$ less than 0.9.

We then gained intuition for what $M_{dist} = 0.9$ actually implies for differences between sets of points on the surface of a sphere. We placed $N$ points randomly on the surface of the unit sphere, perturbed them randomly on the surface for some number of timesteps, and computed both $M_{dist}(t)$ (calculated for the set of points $\{\boldsymbol{r}^N(t)\}$ at time t with respect to the set $\{\boldsymbol{r}^N(0)\}$ at time 0) and $\sqrt{\langle \Delta r^2 \rangle}$ (the time-dependent root-mean-squared distance between $\{\boldsymbol{r}^N(0)\}$ and $\{\boldsymbol{r}^N(t)\}$). We then compared these two metrics. For $N = (5, 10, 20, 30, 40, 50)$ points, a value of $M_{dist} \sim 0.90$ corresponded approximately to $\sqrt{\langle \Delta r^2 \rangle}$ in the range $[0.10 - 0.25]$. The relationship is not one-to-one given the angular sensitivity of $M_{dist}$. A quick back-of-the-envelope calculation (in the following paragraph) shows that this range of average particle displacements is not very significant with respect to the length scales of our dense clusters.

The upper limit of the average particle displacement range implied by $M_{dist} \sim 0.90$, $\sqrt{\langle \Delta r^2 \rangle} = 0.25$, is a chord length on the unit sphere that maps to an angular displacement of $\Delta\theta \sim 0.25$. The largest container radius $R$ encompassing any of our maximally dense clusters is $R \sim 4.79$ (corresponding to the $N = 60$ sphere cluster), and thus this angular displacement maps maximally to an average distance between two particles of $\sqrt{\langle \Delta r^2 \rangle} = 2R\sin(\Delta\theta/2) \sim 1.19$. This distance is only about 60% of 2.0, the circumsphere diameter of all particle shapes. Thus, $M_{dist} \gtrsim 0.90$ for two sets of points corresponding to our dense clusters implies that one set can be mapped onto the other with reasonably small average particle displacements, about 60% of one particle circumsphere diameter.

We chose our final, highly specific cutoff of $M_{dist} > 0.88$ by examining the distribution of $M_{dist}^{sph}$ values for all generated clusters. We noted that sticking to a hard cutoff of $M_{dist}^{sph} > 0.9$ would exclude a large number of clusters whose similarity to sphere clusters we could observe by eye. In fact, the largest bin (containing 15 clusters) of a 50-bin histogram of values of $M_{dist}^{sph}$ for all generated clusters was that with edges 0.889 and 0.904 (to 3 decimal places). We also noted that multiple clusters in the range $0.88 \leq M_{dist}^{sph} \leq 0.9$ looked structurally similar to sphere clusters. We therefore took $M_{dist}^{sph} > 0.88$ to be our condition for similarity between cluster structures.

## 3.4 Comparison with sphere clusters

We first compare our results for the densest found clusters of the Platonic solids with those of spheres. To measure similarity, we use $M_{dist}^{sph}$, given by Eq. 2.23 when $i$ is the set of polyhedron centroids for a given cluster of polyhedra and $j$ is the set of particle centroids for the corresponding sphere cluster. Fig. 3.4a shows a scatter plot of values of $M_{dist}^{sph}$ for every densest found cluster as a function of the $IQ$ of the constituent particle shape. Average values $\langle M_{dist}^{sph} \rangle$, computed across the set of all densest found clusters of each Platonic solid, are also marked in Fig. 3.4a with an image of the associated particle.

Given the similarity criterion $M_{dist}^{sph} > 0.88$ (marked by a black horizontal line in Fig. 3.4a and explained in the preceding section), we find that the number of clusters that are similar to sphere clusters is quite high for the icosahedron (the most spherical Platonic solid), and trends downward as the $IQ$ of the particle shape decreases. Of the 57 densest clusters found for each particle shape, 44 clusters of icosahedra, 20 clusters of dodecahedra, two clusters of octahedra, two clusters of cubes, and no clusters of tetrahedra are structurally similar to their corresponding cluster of spheres. $\langle M_{dist}^{sph} \rangle$ also trends downward as $IQ$ decreases.

Table 3.1: Outermost and next inner cluster layers as optimal spherical codes. Numbers corresponding to SC(total) are the number of layers that are deemed similar to optimal spherical codes for each particle shape, followed in parentheses by the total number of layers for which $N_{layer} \geq 4$. $\langle M_{dist}^{SC} \rangle$ is an average taken over each set of layers counted in the parentheses.

| | outer: SC (total) | $\langle M_{dist}^{SC} \rangle$ | inner: SC (total) | $\langle M_{dist}^{SC} \rangle$ |
|---|---|---|---|---|
| Sph | 36 (57) | 0.91 | 14 (30) | 0.82 |
| Icos | 43 (57) | 0.91 | 14 (30) | 0.86 |
| Dod | 42 (57) | 0.90 | 20 (30) | 0.90 |
| Oct | 3 (57) | 0.60 | 6 (32) | 0.77 |
| Cube | 1 (57) | 0.74 | 0 (35) | 0.67 |
| Tet | 0 (57) | 0.52 | 0 (3) | 0.76 |

## 3.5 Common motifs are optimal spherical codes

The dense clusters of spheres consist of layers whose configurations map to optimal spherical codes for a majority of cases. A spherical code, or finite set of points on the surface of a sphere, can be characterized by the minimal angle between vectors pointing from the center of the sphere to any two of the points. Optimal spherical codes are ones for which this minimal angle, which corresponds to the smallest distance between any two of the points, is maximized [39, 122]. Given a point radius (*i.e.* turning these points into circles), the optimal spherical code at $N$ maps to the arrangement of $N$ circles on a sphere such that they fit on its surface at minimal sphere radius and do not overlap. Optimal spherical codes are therefore a way of packing spherical particles such that their configuration within a cluster layer is spherical but still tightly packed. These motifs accordingly dominate in the dense sphere clusters, from which we demand that the particles both pack densely and fit inside a sphere.

The relationship between densest packings within a container and optimal spherical codes was previously addressed by Torquato *et al.* [122, 123]. They defined the $N$-specific densest local packing (DLP) problem, equivalent to finding the densest packing of spheres within a spherical container given that one additional sphere must always be at the center of the container. Torquato *et al.* proved that every solu-

tion to the optimal spherical code problem is also a solution to the DLP problem for $1 \leq R \leq \tau$, where $R$ is the greatest distance from the container center to the center of any sphere and $\tau$ is the golden ratio [122]. They also found solutions to the DLP problem for select values of $N$ up to $N = 1054$, and noted that the majority of their solutions maximized the number of spheres in the surface layer according to the optimal spherical code at the relevant container radius [123].

Here, we expand upon those observations and find that optimal spherical codes are prevalent motifs in solutions to a more general problem, one in which there is no particle fixed at the center of the container and the packing particles are not just spheres but faceted particles as well.

To determine the similarity between cluster layers and optimal spherical codes, we decompose every cluster into layers, and use $M_{dist}^{SC}$, given by Eq. 2.23 when $i$ is the set of particle centroids in a particular cluster layer and $j$ is the optimal spherical code at equal $N_{layer}$. We use conjectured optimal spherical codes found in Ref. [124]. The criterion for similarity is again $M_{dist}^{SC} > 0.88$. Layers in each cluster are identified using the DBSCAN clustering algorithm [125] in the scikit-learn Python module [126]. DBSCAN operates on the set of radial distances from the cluster centroid to all particle centroids. Our tuned DBSCAN parameters delineate cluster layers in nearly all cases, but we fail to detect distinct layering for one cluster of cubes ($N = 39$) and for 14 clusters of tetrahedra ($N = 45, 46, 49 - 60$), due to less distinct layering for these less spherical particles. Although these clusters consist of particles at a range of radial distances from each cluster center, the radial distances are not well-separated enough to be grouped into distinct layers by DBSCAN.

Fig. 3.4b shows scatter plots of values of $M_{dist}^{SC}$, both for the outermost layer and the next inner layer of every densest cluster found, as a function of the $IQ$ of the constituent particle shape. $M_{dist}^{SC}$ for any layer is only plotted when $N_{layer} \geq 4$. At higher $N$, there is also a third (innermost) layer, but at the particle numbers we

studied this third layer is just a single central particle and is not included in the figure. Average values $\langle M_{dist}^{SC} \rangle$ for each layer, computed across the set of all relevant layers of each particle shape, are also marked in Fig. 3.4b with an image of the associated particle. Table 3.1 tabulates this data.

Optimal spherical code motifs constitute the majority of layers for sphere, icosahedron, and dodecahedron clusters, and even appear in layers of the octahedron and cube clusters. Additionally, $\langle M_{dist}^{SC} \rangle > 0.88$ (marked by black horizontal lines in Fig. 3.4b) for the outer layers of the sphere, icosahedron, and dodecahedron clusters, and the inner layer of the dodecahedron cluster, indicating that these layers are, on average, optimal spherical codes. This is far from the case for the clusters of octahedra, cubes, and tetrahedra.

Given the wealth of studies showing that bulk dense packing is sensitive to minute differences in particle shape, e.g. [38, 113, 127], it is interesting that in spherical confinement icosahedra and dodecahedra pack like spheres. This is noteworthy because of a combination of two facts. First, icosahedra and dodecahedra are dual to each other, i.e. everywhere an icosahedron has a face, a dodecahedron has a vertex, and vice versa. Second, polyhedra make contact with the spherical container only at their vertices. These two facts would lead us to expect that icosahedra would arrange themselves differently than dodecahedra at the surface of the container to accommodate the "opposite" location of their vertices. However, what we observe instead is that the layered spherical code structures that occur for sphere packing are robust against changes in particle shape.

## 3.6 Common clusters across particle shape

Similarity to sphere clusters and optimal spherical codes produces a class of common structures formed by different particle types at specific values of $N$. Values of $N$ for which more than two particle types share a common cluster geometry, as well as

the respective cluster structure, are shown in Fig. 3.5. More common structures could be listed here if we relax our $M_{dist}^{sph}$ criterion; the current set represents a sample based on our cutoff $M_{dist}^{sph} > 0.88$. For most of these values of $N$, common structures are shared by clusters of spheres, icosahedra, and dodecahedra. Layers of these similar clusters are optimal spherical codes, indicated by $M_{dist}^{SC} > 0.88$, in all but six cases.

That these common motifs emerge simply from the spherical confinement of particles as non-spherical as dodecahedra, and in some cases even octahedra and cubes, is a result with intriguing experimental implications. Common configurations are resistant to significant deviations from spherical particle shape, meaning that they may be ideal target structures for the self-assembly of imperfectly spherical colloidal particles or faceted metallic nanoparticles.

## 3.7 Cluster symmetry and density

We next examine the relationship between symmetry and density of the dense packings as a function of $N$. Fig. 3.6 shows both of these cluster properties simultaneously: the respective crystal systems of the symmetry point groups of the outermost cluster layers are shown as vertical bars of color overlaid on plots of the cluster density $\phi_{circ}$ as a function of $N$. The crystal systems of the outermost layers are also tallied in Table 3.2. Point groups were determined by eye for all clusters.

Density profiles are similar in behavior for all particle shapes: density increases sharply with $N$ at low values of $N$, as the densest clusters gain enough particles to be approximately spherical, and then more gradually grows as $N$ increases. We expect $\phi_{circ}$ to approach the bulk densest packing fraction for each particle shape as $N$ goes to infinity, although at $N = 60$ the density is still far from its bulk value in all cases. Cluster symmetry, however, varies widely across $N$ for all particle shapes.

The set of conjectured optimal spherical codes displays a wide variety of point groups [128, 129], and it is thus unsurprising that the layers of the sphere, icosahedron,

Table 3.2: Crystal systems of all outer cluster layers. For each particle shape, data show the total number of outer layers whose symmetry point group belongs to each crystal system. A horizontal line separates crystal systems that are crystallographic from those that are not.

| | Sph | Icos | Dod | Oct | Cube | Tet |
|---|---|---|---|---|---|---|
| cubic | 6 | 6 | 5 | 3 | 5 | 0 |
| hexagonal | 2 | 5 | 1 | 2 | 0 | 1 |
| trigonal | 4 | 6 | 9 | 3 | 3 | 1 |
| tetragonal | 3 | 2 | 4 | 1 | 2 | 1 |
| orthorhombic | 8 | 3 | 7 | 6 | 10 | 2 |
| monoclinic | 8 | 7 | 4 | 7 | 14 | 10 |
| icosahedral | 3 | 3 | 3 | 2 | 1 | 1 |
| decagonal | 2 | 1 | 2 | 0 | 0 | 1 |
| octagonal | 3 | 3 | 1 | 1 | 0 | 0 |
| pentagonal | 2 | 1 | 2 | 0 | 0 | 0 |
| TOTAL | 41 | 37 | 38 | 25 | 35 | 17 |

and dodecahedron clusters also have a variety of symmetries as $N$ varies, at least when they match optimal spherical codes. Within the set of sphere, icosahedron, and dodecahedron clusters, a majority of clusters have non-triclinic point groups, and these point groups are spread widely across ten crystal systems.

It is significant, however, that even those cluster layers that do not map to optimal spherical codes display a variety of symmetries. These include the icosahedron and dodecahedron layers for which $M_{dist}^{SC} \leq 0.88$, as well as the majority of octahedron, cube, and tetrahedron cluster layers. In many cases, irrespective of the anisotropic particle shape, the requirement of high density and cluster sphericity imposed by the container selects for symmetric clusters.

## 3.8 Ulam's conjecture in spherical confinement

As an interesting aside, Ulam conjectured that spheres pack less densely than all other convex solids in infinite space [130]. The $n$-dimensional analogue of Ulam's conjecture is violated in Euclidean spaces for $n = 2, 4, 5, 6, 7, 8$, and 24 [131], but in three

dimensions it has been shown that spheres pack less densely than any other infinitesimal centrosymmetric convex shape deformation [131]. It is not known if in three dimensions spheres continue to be pesimal packers in confinement. We find that for a majority of lower $N$ values, spheres pack inside a spherical container more densely than one or more Platonic solids. In fact, at $N = (4 - 9)$, the sphere cluster has the highest value of $\phi_{circ}$. Spheres are only the worst packers for $N = (26, 29, 31 - 33, 35)$. We believe these results can be explained by considering the volume occupied by the particles in a spherical shell just below the container surface. A single spherical particle necessarily packs more densely than a convex faceted particle near the surface of the container, due to the fact that the faceted particle may touch the container only at its vertices. This density gain by spherical particle packing is a surface effect, and matters less and less as $N$ increases. At small values of $N$, however, it enables spheres to pack more densely than the various Platonic solids inside a spherical container, in contrast to what Ulam's conjecture asserts for infinite space.

## 3.9 Magic number clusters

In every density profile the cluster density jumps at certain values of $N$, and is markedly larger than densities at $N - 1$ and $N + 1$. These values of $N$ are marked by gray circles in Fig. 3.6; we term them "magic numbers" in deference to the wealth of literature exploring magic numbers in other cluster systems. Typically, magic numbers in other systems correspond to clusters of minimal energy [118, 119, 121, 132–134].

We deem a cluster at $N$ to be a magic-number cluster if its density $\phi_{circ}^{N}$ meets three criteria:

1. $\Delta\phi_{circ}^{N} \equiv \phi_{circ}^{N} - \frac{1}{2}(\phi_{circ}^{N-1} + \phi_{circ}^{N+1}) > 0.009$

2. $\phi_{circ}^{N} > \phi_{circ}^{N-1}$

3. $\phi_{circ}^{N} > \phi_{circ}^{N+1}$

Clusters at $N = 4$ and $N = 60$, the minimum and maximum values of $N$, are not considered, since they are incapable of satisfying criterion 1 and criterion 2 or 3, respectively. The cutoff value of 0.009 delimits a varied sample of clusters drawn from every particle shape that nevertheless represents only a small fraction ($\sim 0.064$) of all generated clusters.

The magic-number clusters for all particle shapes are shown in Fig. 3.7, along with the symmetry point groups of their layers. The structure and symmetry of each magic-number cluster vary widely both with $N$ and particle shape.

Magic-number clusters of spheres, icosahedra, and dodecahedra consist of either a single layer or a central single particle or dimer surrounded by an outer layer that maps to an optimal spherical code in 12 out of 15 cases. Multiple shapes have the same outer-layer structure at $N = 6$, 12 & 13, 21, and 38. Note that the $N = 25$ sphere and dodecahedron clusters do not actually share the same structure; the sphere cluster is a central particle surrounded by the $N = 24$ optimal spherical code, whereas the dodecahedron cluster is a central dimer surrounded by the $N = 23$ optimal spherical code. Of the three magic-number clusters that are not layers of optimal spherical codes ($N = 27$ dodecahedra, $N = 38$ spheres, and $N = 38$ dodecahedra), the case of $N = 38$ spheres and dodecahedra is particularly interesting. These clusters are both slight distortions of a particular common structure, a central six-particle octahedron surrounded by an outer layer whose centroids make up the union of a truncated octahedron and a cube. (The $N = 38$ icosahedron cluster is also observed to share this structure, although it is not a magic-number cluster and its value of $M_{dist}^{sph}$ is only $\sim 0.77$.) Although its outer layer is not an optimal spherical code, the $N = 38$ motif occupies a unique place in the pantheon of sphere cluster literature. It is an especially spherical arrangement of maximally close-packed spheres, and is thus optimal under a range of circumstances beyond just dense packing inside a spherical container. The

undistended version of this cluster is a segment of the *fcc* sphere packing, the densest packing possible for spheres in the bulk limit. Called the *fcc* truncated octahedron, this cluster is additionally known to be the global energy minimum of the 38-atom Lennard-Jones cluster [133, 135–137].

The magic-number clusters of the octahedra, cubes, and tetrahedra do not resemble optimal spherical codes, but rather are unique configurations whose structures allow each set of particles to be reasonably spherical and tightly packed. All magic-number clusters are displayed in Fig. 3.7; only a portion will be discussed here. The $N = 9$ octahedron cluster is a central particle surrounded by eight others, each face-sharing with it, in a regular cubic configuration. The $N = 21$ octahedron cluster is a central particle surrounded by a cage of twenty others, face-sharing with each other, in a regular dodecahedral configuration. The $N = 13$ cube cluster is an irregular icosahedral configuration surrounding a central particle in six sets of face-to-face aligned dimers. (A regular icosahedral configuration is an optimal spherical code, but the particular arrangement of these dimers distorts the configuration such that $M_{dist}^{SC}$ does not register the similarity.) The $N = 48$ cube cluster consists of the $N = 13$ cluster, with one dimer replaced by a single particle, surrounded by an outer layer of 36 particles with cubic symmetry (six particles per cubic "side"). The magic-number clusters of tetrahedra will be discussed in the next section.

Magic-number structures are unique, but all exhibit a trade-off between face-to-face alignment among particles, which enables tight packing but not necessarily cluster sphericity, and other types of contact between particles, which may promote cluster sphericity but not tight packing. No single rule appears to determine what makes a particular cluster "magic" for any particle shape: locally maximal density does not select for a particular type of symmetry or structure across particle types or even within the same particle type. These magic-number clusters do, however, provide a set of especially dense structures that possess symmetries not achievable via

the spherical confinement of spheres, icosahedra, or dodecahedra at identical values of $N$, a fact whose implications will be discussed in the *Conclusions*.

## 3.10 The densest found cluster of tetrahedra

The densest found cluster of tetrahedra suggests a connection between dense packings in a sphere and locally-preferred motifs[37] during the self-assembly of an unconfined bulk system. A bulk fluid of tetrahedra self-assembles into a dodecagonal quasicrystal under suitable conditions [138], forming a structure that is markedly different from the bulk densest known packing of tetrahedra (a crystalline arrangement with four tetrahedra per unit cell, arranged in two face-sharing dimers [111]). It was shown that en route to the quasicrystal, 20-tetrahedron icosahedral clusters in the fluid rearrange to form a 22-tetrahedron structure [138]. This 22-tetrahedron cluster consists of two pentagonal dipyramids at the cluster poles and a set of six face-to-face aligned dimers ringing the cluster equator. It is precisely the structure we find to be a magic-number cluster. Indeed, our set of densest found tetrahedron clusters forms a telling sequence of structures: as $N$ increases, the densest cluster passes from the $N = 5$ pentagonal dipyramid, through the $N = 20$ icosahedron, and maximizes cluster density at $N = 22$. Cluster density then dips, and significantly drops at $N = 27$ when the densest found cluster contains a particle at its center. That the $N = 22$ tetrahedron cluster is both a prominent motif in the self-assembled quasicrystal and the densest structure inside a sphere for $N = (4 - 60)$ suggests that the self-assembly of tetrahedra may favor the formation of local structures that pack densely inside a sphere.

## 3.11 Conclusions

We generated finite dense packings of the Platonic solids, for $N = (4 - 60)$ constituent particles, using Monte Carlo sampling within spherical confinement. We found that generated packings were layered structures, possessing maximally three layers at high $N$ and displaying a variety of point groups. Packings of the more spherical icosahedra and dodecahedra were structurally similar to sphere packings generated by the same method for many values of $N$, while packings of octahedra and cubes were similar to sphere packings only in two instances each, and packings of tetrahedra never matched sphere packings. Common packing structures were layers of optimal spherical codes in a majority of cases. The widespread similarity of finite dense packings of icosahedra and dodecahedra inside a spherical container to those of spheres indicates the suppression of the packing effects of particle shape by the container. Rather than particle shape and orientation, it is the particles' ability to pack tightly into spherical shells by mimicking the behavior of spherical particles and forming optimal spherical codes that enables dense packing. This is a result in contrast to dense packing in infinite three-dimensional Euclidean space, for which particle shape strongly influences packing structure [108, 110, 113].

We also generated cluster density profiles across $N$ for each particle shape, and noted that spheres were not the worst packers with respect to the volume of the container at most values of $N$, and were in fact the best packers at especially low values of $N$. This result is not consistent with the conjectured behavior of dense packings of spheres and convex solids in infinite space [130]; we hypothesize that it is due to the fact that spheres pack more densely than faceted convex particles near the surface of a spherical container. This surface packing effect becomes less influential on density as system size increases. Our density profiles additionally indicated clusters of especially dense design that we termed magic-number clusters. These clusters vary in symmetry and structure.

Common structures shared by clusters of spheres, icosahedra, dodecahedra, and in a few cases octahedra and even cubes are a class of dense motifs that are resistant to changes in particle shape, a result of interest to those in the colloidal and plasmonics communities for whom the fabrication of highly spherical particles is difficult to achieve or experimentally undesirable. In the plasmonics community, for example, recent efforts have focused on the manufacture of highly spherical metallic nanoparticles for the production of plasmonic nanoclusters with consistent and reproducible structure [116]. However, faceted geometries are thermodynamically preferred over spherical geometries during the metallic nanoparticle growth process [116, 139], which complicates the production of spherical metallic nanoparticles. We showed here that a host of sphere cluster geometries, including among many others the optically interesting four-particle tetrahedron [81] and 13-particle centered icosahedron [140], are in fact robust against changes in particle shape. They can be formed by significantly non-spherical particles if the clusters are created via spherical confinement. Moreover, faceted particles within these common motifs assume a variety of contacts with their neighbors, including edge-to-edge, face-to-face, and edge-to-face. Recent work on the optical properties of different metallic nanoparticle junction types [115, 117] indicates that these clusters, although they share common geometries, may exhibit diverse and interesting optical behavior if formed from metallic nanoparticles.

Our dense magic-number clusters provide examples of structures with experimentally useful geometries that are difficult to achieve otherwise. Many magic-number clusters, especially of the less spherical shapes, have configurations that are not achievable by densely packing spheres, and could be accessible via confinement within an emulsion droplet or other spherical container. For instance, our densest cluster of 21 octahedra, a dodecahedral cage of 20 particles surrounding a central one, possesses a structure that closely-packed spheres, either within a spherical container or in bulk, do not adopt. Moreover, recent work shows that this dodecahedral geometry may

have implications for self-assembled metamaterials [141].

Finally, we found that dense packing in spherical confinement may result in multi-particle motifs that are preferred in the self-assemblies of unconfined dense fluids of hard polyhedral particles. For systems of tetrahedra, the densest found cluster in spherical confinement does appear as a common motif in the self-assembled do-decagonal quasicrystal, suggesting indeed that tetrahedron crystallization favors the formation of local structures that pack densely inside a sphere.

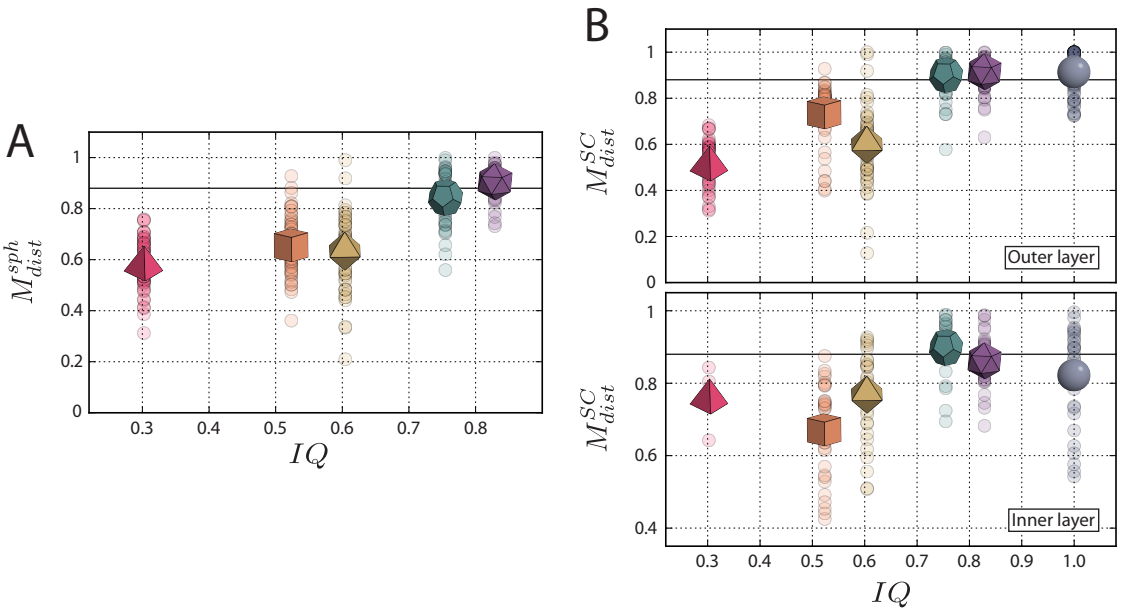


Figure 3.4: Comparison of (a) densest found clusters of the Platonic solids to densest found clusters of spheres, indicated by $M_{dist}^{sph}$, and (b) the outermost and next inner layers of densest found clusters of the Platonic solids and spheres to optimal spherical codes, indicated by $M_{dist}^{SC}$. $M_{dist}^{SC}$ for any layer is only plotted when $N_{layer} \geq 4$. Values of $M_{dist}$ for all clusters and cluster layers are plotted as a function of the isoperimetric quotient ($IQ$) of the constituent particle shape. Clusters whose value of $M_{dist}$ lies above 0.88, indicated by a horizontal line in each figure, are deemed similar to their corresponding cluster of spheres or optimal spherical code. Average values $\langle M_{dist} \rangle$, computed across the set of all densest found clusters or relevant cluster layers for each particle shape, are marked with an image of the associated shape. The more spherical polyhedra (icosahedra and dodecahedra) form clusters that increasingly resemble those of spheres, and a majority of sphere, icosahedron, and dodecahedron cluster layers match optimal spherical codes.

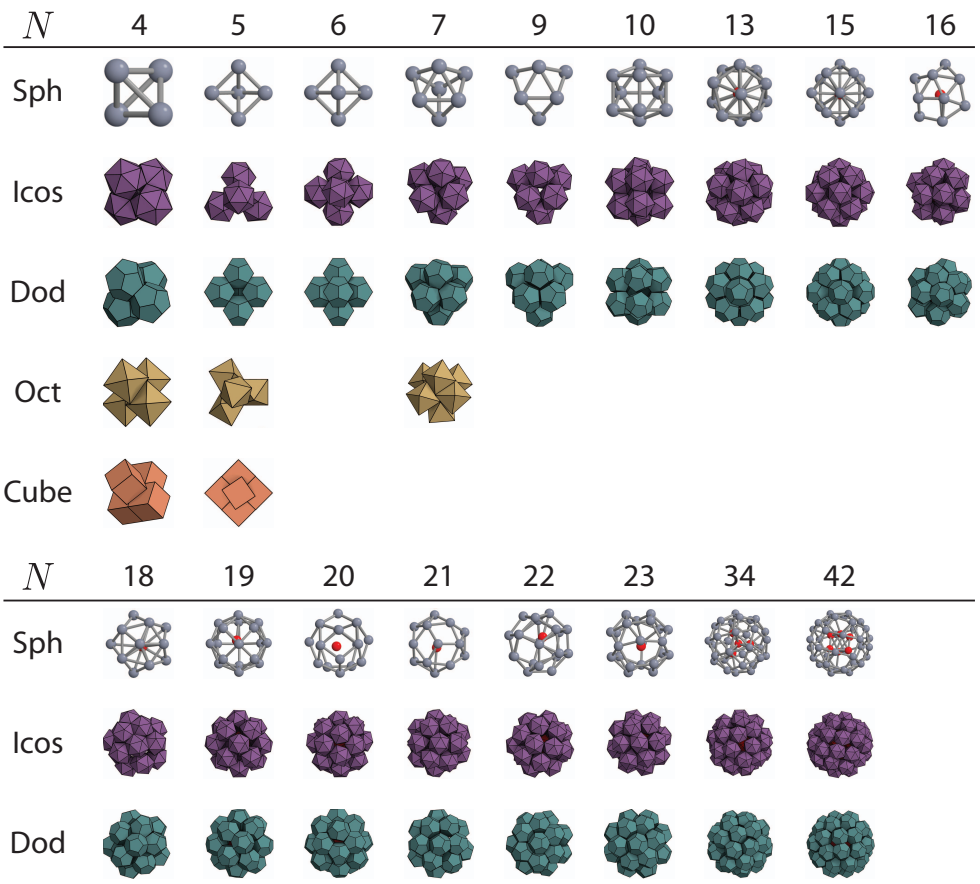


Figure 3.5: Common cluster structures across multiple particle types. $N$ indicates the number of particles in each cluster, and rows labeled Sph show the positions of the centroids of the corresponding sphere clusters. Rows labeled Icos, Dod, Oct, and Cube show corresponding clusters of icosahedra, dodecahedra, octahedra, and cubes respectively. Clusters of Platonic solids are similar to these sphere clusters, and included in this table, if $M_{dist}^{sph} > 0.88$. At $N = 5$ the sphere, dodecahedron, and cube clusters are a square pyramid, while the icosahedron and octahedron clusters are the $N = 5$ optimal spherical code, a triangular bipyramid.

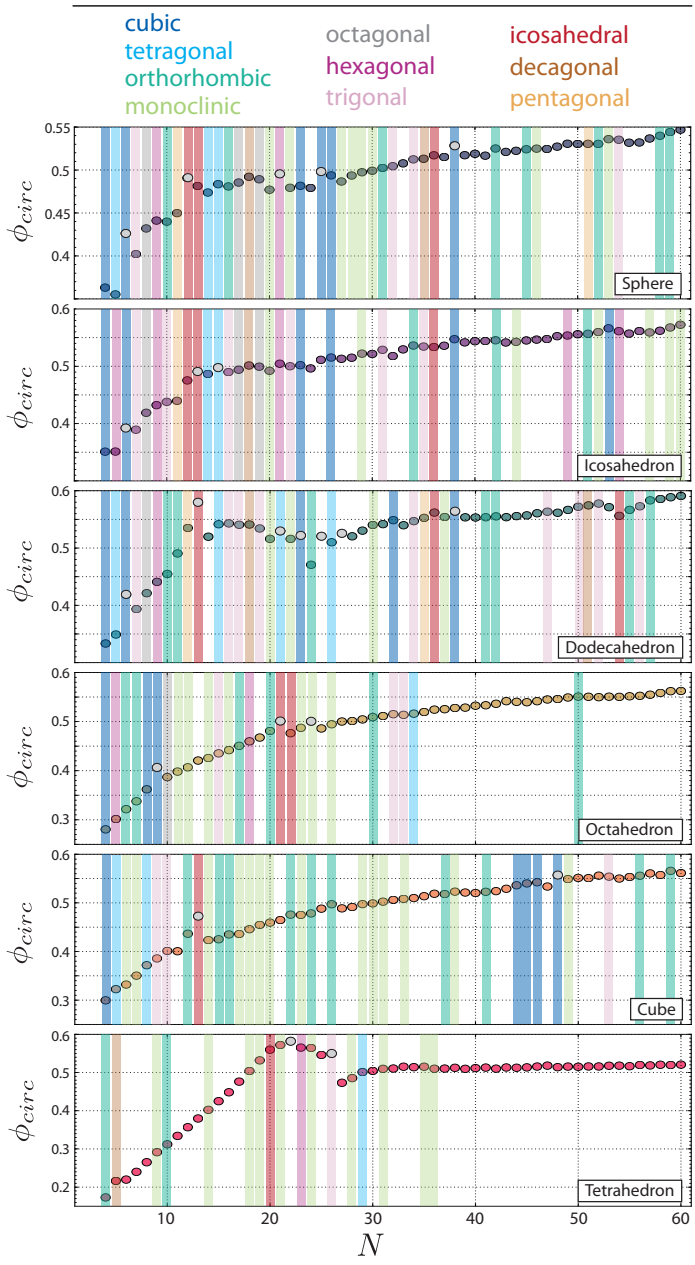


Figure 3.6: $\phi_{circ}$ with respect to particle number for all densest clusters found. Colored bars indicate the crystal system of each outer cluster layer. Identically colored bars for clusters of different shapes denote the same crystal system. Gray data points are those deemed to be "magic-number" clusters.

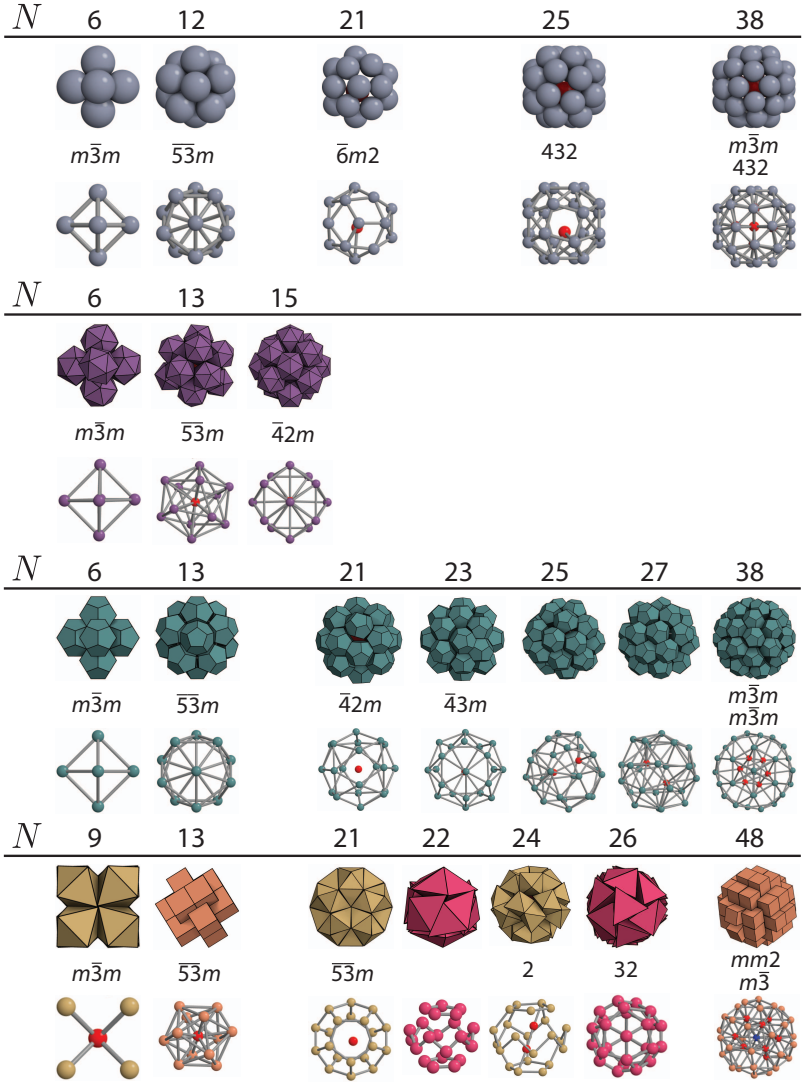


Figure 3.7: All magic-number clusters for the spheres and polyhedra studied. Headers above each row of images show the particle number $N$ of each cluster. Cluster snapshots and centroid skeletons are shown. Included with each set of cluster images are the symmetry point groups of its layers. When multiple symmetries are shown, the topmost symmetry belongs to the inner cluster layer.

# CHAPTER IV

# Local structure in hard particle glass-formers

This chapter is adapted from Ref. [142], a publication authored by E.G. Teich, G. van Anders, and S.C. Glotzer that is currently under review.

## 4.1 Local structure and glass formation: the search for a causal link

A universally accepted explanation for why liquids sometimes vitrify rather than crystallize remains hotly pursued, despite the ubiquity of glass in our everyday lives, utilization of the glass transition in rewritable data storage devices [23], fiber optic networks [24], and other technologies, and nearly a century of theoretical and experimental investigation. Researchers generally agree on the phenomenological behavior of liquids as they are supercooled. However, the underlying mechanism of the glass transition remains in contention, and while dynamical glass-forming signatures including caging, cooperative string-like motion, and dynamical heterogeneity [143, 144] are well-characterized and established within the community, structural signatures of glass formation (if indeed they exist at all [145]) have yet to be fully elucidated. Among the most compelling hypothesized structural mechanisms underlying glass formation is the development in the fluid phase of local structures that somehow prevent crystallization [26, 27, 146, 147]. What these local structures are, why

they form, and how exactly they prevent long-range ordering are central, unanswered questions.

The search for local structure in various model and experimental glass-formers, essentially to answer the first question just posed, is an ongoing endeavor. A great many investigations have focused on local ordering in isolated model and experimental glass-formers, including systems of binary Lennard-Jones particles [52, 148–152], particles interacting via a Dzugotov-like potential [153, 154], polydisperse hard spheres [155–159], polydisperse hard disks [160], colloidal gels [161], metallic glasses [162–167], patchy particles [168], and even a system of two-dimensional kites [169].

In parallel to this structural classification, the establishment of a causal structural mechanism for dynamical arrest remains a holy grail for those in the glass community, with countless paradigms proposed over the decades to do just that. Thermodynamical theories of Goldstein [170], Adam and Gibbs [171], and the random first-order transition theory of Kirkpatrick, Thirumalai and Wolynes [172] have all posited that localized structural rearrangements are responsible for dynamical signatures related to relaxation in glass-formers, though none firmly specify what those rearranging structures might look like. Frustration-limited domain theory [146] is more specific, asserting that liquids are characterized by "locally favored structures," or motifs that are locally optimal but do not tile space. Thus, growth of these domains is geometrically frustrated and limited by strain, leading ultimately to vitrification. A more recent pool of studies [35, 147, 158, 160, 173–175] views vitrification more explicitly as the structural frustration of emerging crystalline order. In this context, local bond orientational ordering and possibly multiple medium-range crystalline orderings may compete and cause crystallization failure. Recent developments indicate that this competition results in a higher structural difference between the liquid phase and any possible crystal phase, and manifests in a larger interfacial penalty between those phases [174, 175]. These different types of order can be mechanisms of crystallization

in other systems that are closely related to the glass-former.

Our work draws inspiration from these latter studies: we systematically investigate structural competition between different types of crystalline ordering in a full two-dimensional landscape of related systems, and provide a link, for multiple glass-formers in a unified manner, between vitrification and the existence of nearby self-assembled crystalline structures. We show that glass-forming fluids of hard polyhedral shapes contain local structures that are favored in crystals formed from particles of slightly altered shape; that is, from neighboring shapes in alchemical "shape space" [40, 113]. Rather than arrange into a crystal, particles self-organize due to directional entropic forces [37, 38] into two or more local motifs that are accessible and thermodynamically preferred in crystallizing systems comprised of particles that are nearby in shape space. These motifs exist in each glass-forming fluid at ratios that prevent crystallization into any one crystal structure. This local structural competition creates an "identity crisis" in the fluid and promotes vitrification.

## 4.2 Assembly failure in a shape landscape

Previous work [38, 127, 176, 177] has shown that changing the truncation of polyhedral particles along various symmetry axes is an effective means of systematically and controllably altering self-assembled structure in monatomic systems of these particles. van Anders et al. [37] showed that slight changes to particle shape caused by truncation have the ability to significantly influence local structure in dense fluids of these particles, by changing the entropic advantage systems gain via locally dense particle packing and free volume exchange. These ideas are explored further in Chapter 1.3. Changes in local structure in the dense fluid, brought on by changes to particle shape, shift densities necessary for crystallization, and can even suppress crystallization altogether [38, 176]. Thus, the exploration of a family of monatomic systems composed of polyhedral particles that are related to each other via contin-

uous truncations along certain symmetry axes is an ideal vehicle through which to explore the relationship between local structure in the dense fluid and crystallization failure.

We performed hard particle Monte Carlo (HPMC) [45] simulations of model glass and crystal-formers comprised of hard polyhedra contained in the spheric triangle invariant 323 family [113], a set of convex polyhedra formed by truncating the vertices and edges of a tetrahedron by sets of planes at varying radial distances from the polyhedron center (Fig. 4.1A). The two-dimensional 323 family of polyhedra allows us to investigate shape perturbations in a tractable manner, since in principle the more general space of all possible particle shapes is infinite-dimensional. We use a convention employed previously [177] and define truncation parameters $\alpha_a$ and $\alpha_c$ such that the corners of the shape space are formed by $(\alpha_a, \alpha_c) = (1, 1)$, denoting a cube, $(\alpha_a, \alpha_c) = (0, 0)$, denoting an octahedron, and $(\alpha_a, \alpha_c) = (0, 1)$ and $(1, 0)$, both denoting a tetrahedron. This family is identical under reflection across the line $\alpha_a = \alpha_c$. It was discovered previously [176] that systems in certain regions of this shape space assemble into a rich variety of colloidal crystals. Particles within this family with large tetrahedrally-coordinated facets and smaller facets due to edge or vertex truncation self-assemble into a dodecagonal quasicrystal [38, 138, 176]. With increasing truncation, eventually a region of shape space is reached where cubic diamond or a lower-symmetry diamond derivative is stabilized [38, 176]. Close to the diagonal of the shape family, where particles possess octahedral symmetry, body-centered cubic and face-centered cubic structures are stable, with the exception of a region of shape space for which the complex high-pressure Lithium structure is often observed [38, 127, 176, 177]. More complicated $\gamma$-brass, $\beta$-Mn, and bc8 structures are also observed to assemble from shapes in select, narrow regions of this shape space [176]. Systems comprised of particles in other regions of shape space remain disordered at densities ranging from $\phi = 0.50$ to 0.65 [176]. We independently reproduced

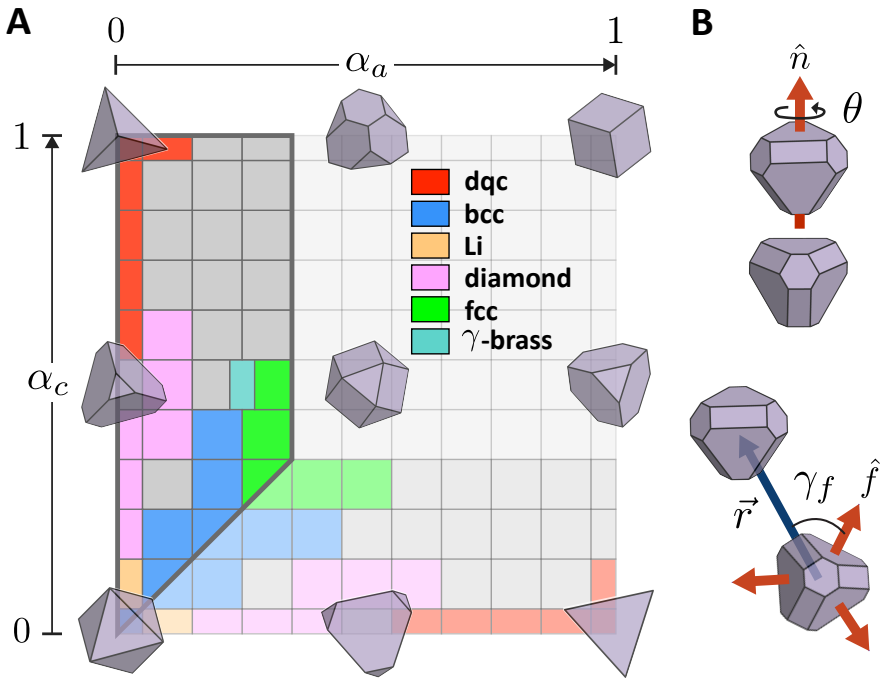


Figure 4.1: Simulation space and analysis methods. (A) The spheric triangle invariant 323 family, with the portion of the shape space explored in this study outlined. The remaining region is colored a light gray; for details on self-assembly behavior in this region, see Damasceno *et al.* [38] and Klotsa *et al.* [176]. Sample particle shapes are overlaid above corresponding regions of shape space, and regions are colored according to the assembled structure of the corresponding particle shape at densities between $\phi = 0.48$ and $\phi = 0.64$. At $(\alpha_a, \alpha_c) = (0, 0.2)$, the system assembles into a compressed derivative of diamond with lower symmetry, but that region is colored identically to the other (cubic) diamond-formers to emphasize the similarity of these structures. At $(\alpha_a, \alpha_c) = (0.3, 0.3)$, assembly into *bcc* occurs at $\phi = 0.64$, while assembly into *fcc* occurs at lower densities; we color this region by the structure it assembles at the lowest density. For a broad swath of the highlighted landscape, colored gray, assembly fails to occur at any investigated density. (B) Characterization of local pairwise motifs. $\theta$ denotes the minimal angle associated with the rotation (about $\hat{n}$) that orients a particle identically to its nearest neighbor. $\gamma$ denotes the minimal angle associated with the projection of $\vec{r}$ onto the set of unit vectors pointing to some feature of the non-truncated version of the particle shape. In this example, vectors point to centers of the faces of the non-truncated particle shape, and $\gamma_f$ is the angle associated with the projection onto $\hat{f}$.

these findings for $\{0 \leq \alpha_a \leq 0.3, \quad 0 \leq \alpha_c \leq 1\}$ at a shape space grid resolution of $\Delta\alpha = 0.1$, finding the assembly of the $\gamma$-brass structure at finer resolution at $(\alpha_a, \alpha_c) = (0.25, 0.5)$.

Fig. 4.2A shows the critical packing fraction, or lowest packing fraction at which crystallization was observed, across the shape landscape. Also shown in Fig. 4.2B are crystallization times at the critical packing fraction. We define crystallization time, or so-called nucleation incubation time [178], as the first frame after which approximately all crystalline particle fractions measured over the trajectory are greater than 0.1. Crystalline particles were identified according to an environment matching scheme detailed in Chapter 6.1. If the crystalline fraction never surpasses 0.1, the system did not crystallize. For nucleation of the dodecagonal quasicrystal, we estimated the crystallization time by eye, corroborating our observations by calculating pressure over the simulation trajectory (using volume perturbation methods discussed in Section 4.11.3) when that data was available, and confirming that pressure begins to drop to its crystal value around the estimated crystallization time.

For a more detailed map of the critical packing fraction across this shape landscape, see Klotsa et al [176].

## 4.3 Dynamical characterization of disordered systems

Those systems failing to crystallize despite excessively long simulation runs exhibit all of the usual characteristic dynamics of glass formers [143, 144], and we note that dynamical glass-forming characteristics of several one-component systems of hard polyhedra have been reported elsewhere [179].

For each system, we calculated the following order parameters at logarithmic timescales: the mean-squared displacement $\langle \Delta r^2(t) \rangle$ of all particles in the system, the self-part of the intermediate scattering function $F_s(\boldsymbol{k}, t)$, computed for the $k$-value associated with the first peak of the static structure factor, the non-Gaussian

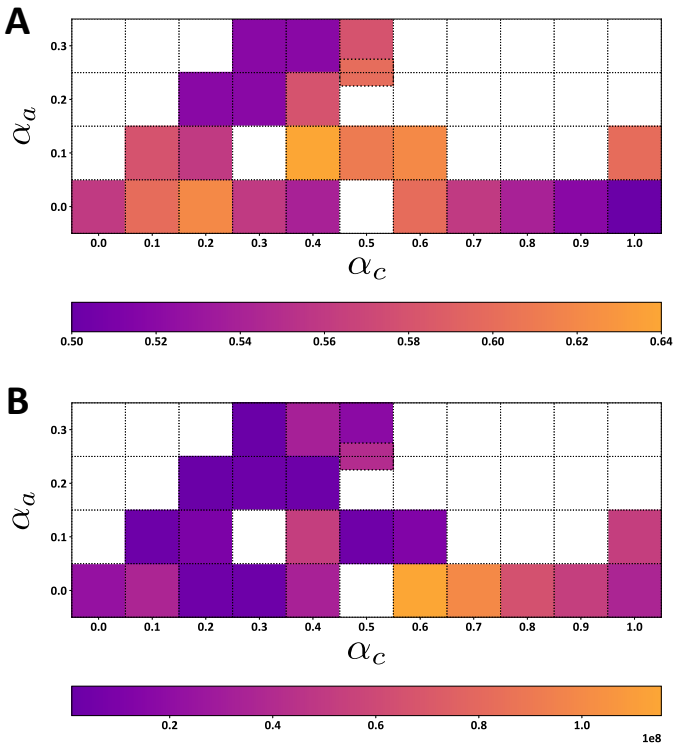


Figure 4.2: (A) Critical packing fraction and (B) crystallization time at the critical packing fraction across the shape landscape. Color bars below each panel show relevant limits and scales. Squares are left uncolored if crystallization was not observed at any density at the corresponding location in shape space, or if the location in shape space is outside the bounds studied in this paper.

parameter $\alpha(t)$ [180], and the self-part of the four-point susceptibility $\chi_4^{SS}(t)$ [181, 182]. These quantities are defined as follows:

$$\langle \Delta r^2(t) \rangle \equiv \frac{1}{N} \left\langle \sum_{j=1}^{N} (\Delta \boldsymbol{r}_j(t))^2 \right\rangle \tag{4.1}$$

$$F_s(\boldsymbol{k}, t) \equiv \frac{1}{N} \left\langle \sum_{j=1}^{N} e^{i\boldsymbol{k}\cdot\Delta\boldsymbol{r}_j(t)} \right\rangle \tag{4.2}$$

$$\alpha(t) = \frac{3\left\langle \Delta r^4(t) \right\rangle}{5\left\langle \Delta r^2(t) \right\rangle^2} - 1 \tag{4.3}$$

$$\begin{aligned} \chi_4^{SS}(t) &= N\left[\left\langle Q_S^2(t)\right\rangle - \left\langle Q_S(t)\right\rangle^2\right] \\ Q_S(t) &= \frac{1}{N}\sum_{j=1}^{N} H\left(a - |\Delta \boldsymbol{r}_j(t)|\right) \ . \end{aligned} \tag{4.4}$$

In all definitions above, $\Delta \boldsymbol{r}_j(t) \equiv \boldsymbol{r}_j(t) - \boldsymbol{r}_j(0)$. In the final expression, $H$ is the Heaviside step function: $H(x) = 1$ for $x > 0$ and 0 otherwise. $a$ is a length-scale associated with the self-overlap of any particle in the system; in this paper we took $a$ to be the inscribing sphere radius of the particle shape for each system. In all cases, angle brackets indicate ensemble averages. We determined that relaxation in most systems is complete by about 10 million MC sweeps; thus, we broke each trajectory into 10 windows and took appropriate ensemble averages over these windows. Error bars were determined through either error propagation or jackknife resampling.

We computed $F_s(\boldsymbol{k}, t)$ at every pertinent lagtime $t$ by averaging over computed values of $F_s(\boldsymbol{k}, t)$ for 10 randomly generated vectors with magnitude $k$ in a similar

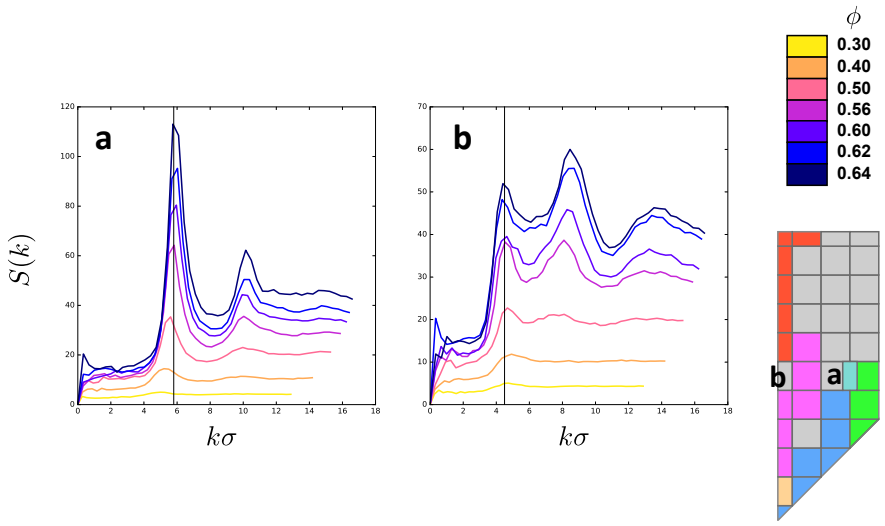


Figure 4.3: Static structure factors for the systems identified by letters in shape space. Vertical lines through each plot indicate the position of the first peak, used for calculation of the self-intermediate scattering function in the main text. These positions are $k\sigma = 5.8, 4.5$ for $(\alpha_a, \alpha_c) = (0.2, 0.5)$, $(0, 0.5)$ respectively.

manner to that described elsewhere [179]. We did this to speed up our calculations, as $F_s(\boldsymbol{k}, t) = F_s(k, t)$ in an isotropic medium. We computed $F_s(\boldsymbol{k}, t)$ for the $k$ value corresponding approximately to the location of the first peak of the static structure factor of each system, as shown in Fig. 5.2. The static structure factor is defined as $S(\boldsymbol{k}) \equiv \frac{1}{N}\langle\sum_{j,l=1}^{N} e^{i\boldsymbol{k}\cdot(\boldsymbol{r}_l - \boldsymbol{r}_j)}\rangle$. We found $S(\boldsymbol{k})$ via the squared FFT of the number density $\rho(\boldsymbol{r})$ of the system, Gaussian-blurred for smoothness, since $S(\boldsymbol{k}) = \frac{1}{N}\left|\langle\int d\boldsymbol{r}\rho(\boldsymbol{r})e^{i\boldsymbol{k}\cdot\boldsymbol{r}}\rangle\right|^2$. We then found $S(k)$ by assuming that the system is isotropic, and spherically averaging $S(\boldsymbol{k})$ using a channel-sharing method [183]. The static structure factors we show here were calculated for the first frame of the trajectory only. They are given as functions of $k\sigma$, where $\sigma$ is a length scale that characterizes the particle size of each system: $\sigma^3 = v_p$, where $v_p$ is the particle volume (1 in all cases).

In glass-forming systems generally, $\langle\Delta r^2(t)\rangle$ and $F_s(\boldsymbol{k}, t)$ increasingly display three regimes as density increases or temperature decreases: a regime at short timescales in

which particles move without colliding with any others, a caging regime at intermediate timescales in which particles are caged by their neighbors and relaxation slows, and a regime at long timescales in which particles escape the confines of their cages and eventually diffuse through the system. $\alpha(t)$ gives a measure of the degree to which the distribution of particle displacements in the system deviates from a Gaussian distribution. It typically has a peak in glass-forming systems at times of large dynamical heterogeneity [184, 185], when some particle motions are cooperative and therefore a subset of particle displacements is higher than that given by the expected Gaussian distribution. $\chi_4^{SS}(t)$ gives a direct measure of the dynamical heterogeneity of the system, as it is the scaled variance of the 2-point self-correlation function $Q_S(t)$: $\chi_4$ grows from zero as heterogeneity in the dynamics of the system increases over a time window $t$, and decreases back to zero at long times in the dense fluid.

The glass-forming behavior of the systems $(\alpha_a, \alpha_c) = (0, 0.5)$ and $(\alpha_a, \alpha_c) = (0.2, 0.5)$ is summarized in Fig. 4.4. For all state points studied, plateaus in the mean-squared displacement $\langle \Delta r^2(t) \rangle$ and the real part of the self-intermediate scattering function $F_s(k, t)$ indicate caging, and relaxation associated with escaping this regime corresponds to peaks in the non-Gaussian parameter $\alpha(t)$ and the self-part of the four-point susceptibility $\chi_4^{SS}(t)$. Thus, we find that our systems display canonical behavior associated with glass formation. One notable difference between our system and other glass-forming models simulated via molecular dynamics (MD) appears in the non-Gaussian parameter: for systems simulated via MD, $\alpha$ goes to zero as $t$ goes to zero because the system is Gaussian at short times. As expected for an MC simulation, however, we find that $\alpha$ does not go to zero at short times, and instead increases as $t$ decreases in the short time regime. This behavior is due to the discrete nature of particle moves during MC sampling. As $t$ goes to zero our probability distribution of particle positions can be thought of as that of a random walk in which just one step is attempted, and a back-of-the-envelope calculation of $\alpha$ in an associated toy model

gives values that are comparable to those we see at short times in our system. See Appendix C for more detail.

## 4.4 Disordered systems are super-compressed

We first discuss results of stability tests for candidate crystal structures in our example glass-forming systems. We systematically changed the shape of particles comprising crystal structures near these glass-formers in shape space, transforming the particle shape incrementally into the glass-forming shape, and measured melting density and pressure as a function of particle shape. We found that, at each investigated glass-forming location in shape space, select crystals remain stable in density regimes for which we observed no crystallization from the fluid. This strongly suggests that these glass-forming fluids are "super-cooled," or more accurately, super-compressed.

Figs. 4.5 and 4.6 summarize our results, and show plots of melting density as a function of particle shape for several candidate crystal structures. Melting plots show the solidus line, or lowest density at which systems remain fully crystallized, and the liquidus line, or lowest density at which crystals coexist with the fluid. In all cases, the densities shown are the highest found across all replicates, since our method establishes a lower bound for melting density. Highest liquidus or solidus densities across replicates thus represent the most restrictive lower bound. Each solidus line is labeled by the crystal structure that is stable above the line. In some cases, systems undergo phase transitions during the melting process to other solids. Whether the system passes through a fluid phase during that process or undergoes a solid-solid phase transition is not shown here, because our method is not rigorous enough to determine the nature of these transitions. Instead, we simply show stability lines for all observed structures. Some crystal structures observed in the melting process were identical to those self-assembled from the fluid. Otherwise, we describe them below.

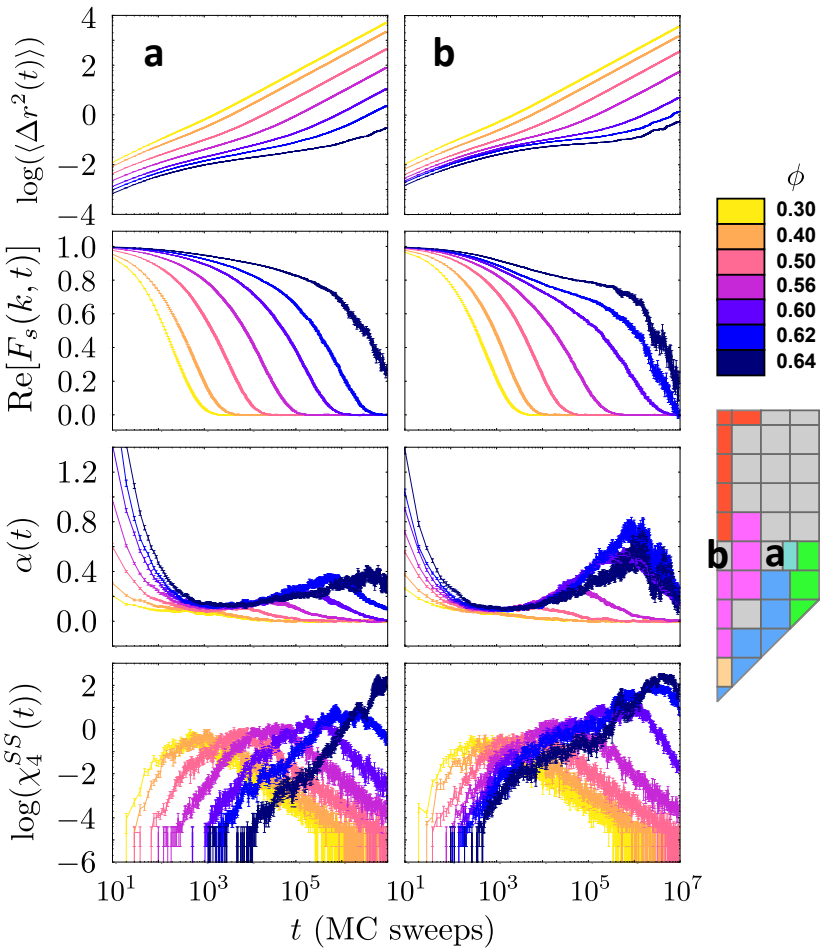


Figure 4.4: The mean-squared displacement $\langle \Delta r^2(t) \rangle$, the real part of the self-intermediate scattering function $F_s(k,t)$, the non-Gaussian parameter $\alpha(t)$, and the four-point susceptibility $\chi_4^{SS}(t)$, measured at a variety of densities for two disordered state points in our shape space. Signatures in all four order parameters indicate that these systems are glass-formers. The increase in $\alpha(t)$ as $t$ goes to zero is due to the discrete nature of Monte Carlo sampling; see Appendix C for more detail.

The "hR6-SbSn/hR6/oC4" melting line shows the stability of three interrelated phases, whose delineation was often not clear during the melting process itself. "hR6-SbSn" is a lower (hexagonal) symmetry diamond derivative, featuring a coordination number of 4 for all particles and squashed tetrahedral local environments. Its Pearson symbol is hR6, and its space group is $R\bar{3}m$, number 166. We use the short-hand hR6-SbSn because compounds of Sb and Sn have been found to crystallize into this structure [186]. "hR6" is a slightly distorted version of hR6-SbSn, with the same space group. Next nearest neighbor distances are shifted closer to each particle, such that there is no clear peak in the radial distribution function corresponding to four nearest neighbors, and instead the structure could be described with a larger coordination number of 14. "oC4" is a related structure of lower symmetry with coordination number 12. Its Pearson symbol is oC4, and its space group is $Cmcm$, number 63.

The "bcc (OO)" melting line corresponds to orientationally-ordered *bcc*, featuring all particles oriented in the same direction. The "bcc (OD)" melting line corresponds to orientationally-disordered *bcc*, featuring plastic-like particle orientations. Equations of state indicate a phase transition between these two phases, so we mark them distinctly. For more information regarding orientational phase transitions in hard particle systems, see Karas *et al.* [187].

The "distorted/tetragonal diamond" melting line describes systems that shear and distort, occasionally managing to form a lower symmetry tetragonal diamond derivative, when melted from cubic diamond at higher $\alpha_c$. This signature appears in the pressure and indicates a phase transition between this strained or lower symmetry phase and (cubic) diamond at lower densities. Because we keep the box cubic, the phase transition is not clean, and strain occurs; however, "floppy box" simulations in these $\alpha_c$ regimes, in which we allow the box aspect ratio and box shear to change randomly and independently (while keeping box volume fixed), do show clear phase transitions between a lower symmetry diamond derivative phase at high pack-

ing fraction and cubic diamond at lower packing fraction. This phase transition in these systems was first observed by Cersonsky *et al.* [188]. The lower-density (cubic) diamond structure melts at approximately the same density in these floppy box simulations as it does in the simulations in which we keep the box fixed and cubic.

We also used floppy box Monte Carlo to investigate the melting of the other crystals shown in these figures at identical locations in shape space; we did not observe any qualitatively different behavior in the melting lines or the stable structures exhibited by each system with decreasing density.

Our melting lines are in the spirit of other phase diagrams calculated as functions of various system control parameters [175, 189]. In those cases, it was observed that good glass-formers appear near eutectic points in these phase diagrams, when the stable crystal structure undergoes a cross-over. We find evidence of eutectic points near our glass-forming state points, although at each glass-forming location in shape space, there is a crystal structure that is more stable than the others investigated and whose stability easily extends into the fluid density regime. The glass-former at $(\alpha_a, \alpha_c) = (0, 0.5)$, in particular, appears to be at a location in shape space for which the nearby diamond crystal is actually more stable than in the region for which diamond self-assembles. Thus, we argue that a close examination of the fluid phase itself, and especially its structural make-up, is necessary for a complete understanding of crystallization failure in these systems.

## 4.5 Identity crisis in alchemical space

Fig. 4.7 displays the local structural motifs we observe for two example glass-forming systems at a variety of densities and crystals nearby in shape space at $\phi = 0.62$ and $\phi = 0.6$. We define motifs as pairwise configurations of each particle and its nearest neighbor, and classify them by their connection type (face, edge or vertex) and relative particle misorientation $\theta$ as detailed in Chapter 2.2.1 and shown in Fig.

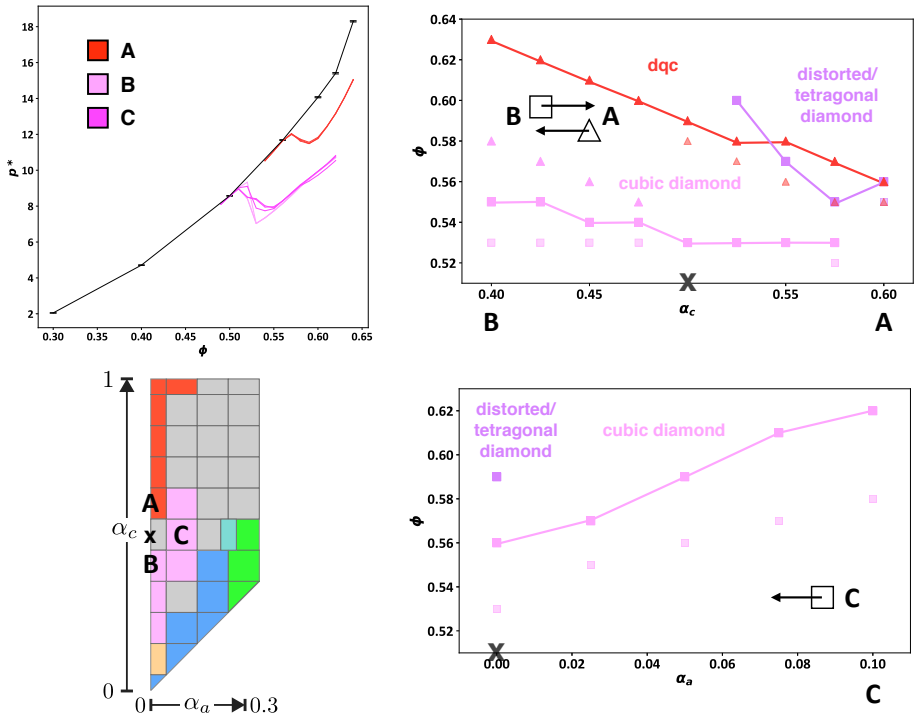


Figure 4.5: Stability testing of crystal structures near the glass-forming state point at $(\alpha_a, \alpha_c) = (0, 0.5)$. Crystal structures tested are (A) the dodecagonal quasicrystal self-assembled at $(\alpha_a, \alpha_c) = (0, 0.6)$ as a function of decreasing $\alpha_c$, (B) the diamond structure self-assembled at $(\alpha_a, \alpha_c) = (0, 0.4)$ as a function of increasing $\alpha_c$, and (C) the diamond structure self-assembled at $(\alpha_a, \alpha_c) = (0.1, 0.5)$ as a function of decreasing $\alpha_a$. The upper left panel shows the equation of state of the super-compressed fluid at $(\alpha_a, \alpha_c) = (0, 0.5)$ in black, and the melting equations of state of the indicated crystal structures at $(\alpha_a, \alpha_c) = (0, 0.5)$. Melting line plots show the stability of the structures initialized in each crystal as a function of $\alpha_a$ or $\alpha_c$. Symbols at each value of $\alpha$ indicate the structure in which the system was initialized, as indicated by the legends embedded in the figures. Solidus lines are indicated by opaque, larger symbols, and liquidus lines are indicated by semi-transparent, smaller symbols. Symbols are colored by phase, and each phase is labeled by text above the solidus line in a matching color.

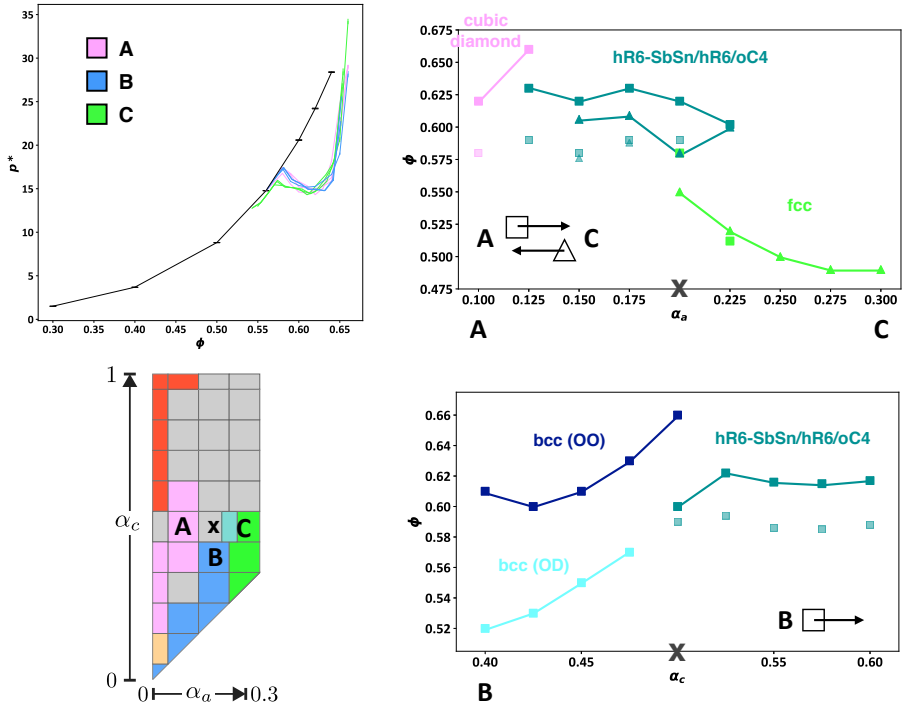


Figure 4.6: Stability testing of crystal structures near the glass-forming state point at $(\alpha_a, \alpha_c) = (0.2, 0.5)$. Crystal structures tested are (A) the diamond structure self-assembled at $(\alpha_a, \alpha_c) = (0.1, 0.5)$ as a function of increasing $\alpha_a$, (B) the *bcc* structure self-assembled at $(\alpha_a, \alpha_c) = (0.2, 0.4)$ as a function of increasing $\alpha_c$, and (C) the *fcc* structure self-assembled at $(\alpha_a, \alpha_c) = (0.3, 0.5)$ as a function of decreasing $\alpha_a$. The upper left panel shows the equation of state of the super-compressed fluid at $(\alpha_a, \alpha_c) = (0.2, 0.5)$ in black, and the melting equations of state of the indicated crystal structures at $(\alpha_a, \alpha_c) = (0.2, 0.5)$. Melting line plots show the stability of the structures initialized in each crystal as a function of $\alpha_a$ or $\alpha_c$. Symbols at each value of $\alpha$ indicate the structure in which the system was initialized, as indicated by the legends embedded in the figures. Solidus lines are indicated by opaque, larger symbols, and liquidus lines are indicated by semi-transparent, smaller symbols. Symbols are colored by phase, and each phase is labeled by text above the solidus line in a matching color.

4.1B. Connection types are calculated with respect to the faces, edges, and vertices of equivalent non-truncated tetrahedra for all particles in the 323 family. Note that due to particle symmetry, $\theta = 90°$ is the maximum possible relative misorientation for all pairwise configurations. Our analysis reveals that every competing motif in the investigated glass-formers is characteristic of a nearby ordered structure. These characteristic motifs compete in each disordered fluid at stoichiometries that impede crystallization into any one particular crystal structure.

Panels show probabilities of observing certain pairwise configurations, $P_{obs}(c, \theta)$, and negative logs of the distributions normalized with respect to an ideal gas, $-\log P(c, \theta)$. The brown curves indicate $P_{rand}(c, \theta)$, and other curves are colored according to their location in shape space. Motifs that are characteristic of nearby crystal structures and that exist in significant number in the glass-forming fluid are shown in insets in the top row of figures, while motifs that are characteristic of nearby crystal structures and that do not exist in significant number in the glass-forming fluid are shown in images in the bottom row of figures. Ranges of $\theta$ that characterize motifs are shown as small black bars, with symbols that represent the motif between them. The symbols are colored according to the crystals in which each is dominant. Circles indicate vertex-connection, squares indicate edge-connection, and triangles indicate face-connection. Heterogeneous connections are possible, where one member of the pair has one connection type, and the other has another connection type. Motifs in ordered systems were calculated at $\phi = 0.62$, with the exception of the $\gamma$-brass crystal, for which motifs were calculated at $\phi = 0.6$.

Fig. 4.7A shows the glass-former at the location $(\alpha_a, \alpha_c) = (0, 0.5)$ in shape space, sandwiched between shapes that form the diamond structure and shapes that form a dodecagonal quasicrystal. We find that the glass-former is increasingly dominated by face-connected particles as density increases. Vertex connection is heavily suppressed, even at lower densities around $\phi = 0.5$, and edge connection is increasingly suppressed

with increasing density. The function $(-\log P(f,\theta))$ for the disordered system shows two distinct basins, around $\theta = 90°$ and $\theta = 70°$, and the depth of both basins increases with density. The nearby dodecagonal quasicrystal shows a corresponding basin around $\theta = 70°$, while the nearby diamond structure shows a basin at $\theta = 90°$. By inspection, the basin around $\theta = 70°$ corresponds to an "aligned" motif (drawn in red) consisting of two particles face-to-face and rotated such that their truncated vertices are aligned; a perfectly-constructed pair with this configuration has a misorientation $\theta \sim 70.53°$. The basin at $\theta = 90°$, by contrast, corresponds to a "twisted" motif (drawn in pink) consisting of two particles face-to-face and twisted such that the edge midpoints of one particle align with the truncated vertices of the other. Thus, these motifs coexist in the glass-forming fluid, and each motif is dominant in a nearby crystal. The aligned motif is abundant in the nearby dodecagonal quasicrystal and absent in the nearby diamond structure, while the twisted motif is abundant in the nearby diamond structure and absent in the nearby quasicrystal. We will show that these motifs exist in the glass-forming fluid at ratios that prevent crystallization into either structure, and thus that these motifs compete in the glass-forming fluid.

Fig. 4.7B shows results for the second example glass-forming shape, located at $(\alpha_a, \alpha_c) = (0.2, 0.5)$ and surrounded in shape space by shapes that self-assemble into a dodecagonal quasicrystal, the diamond crystal, a *bcc* crystal, an *fcc* crystal, and a $\gamma$-brass crystal structure. This competition is more complicated, due to the multiple competing nearby crystal structures, and the fact that some nearby crystal structures are characterized by multiple pairwise motifs. Each crystal structure, however, does have particular pairwise configurations that are more probable for that structure than any other structure and more probable than in the random gas; we will take these as the motifs that are characteristic of each crystal structure.

We find that vertex-connection is heavily suppressed in the glass-forming system at all investigated densities. This connection type is characteristic of the nearby *bcc*

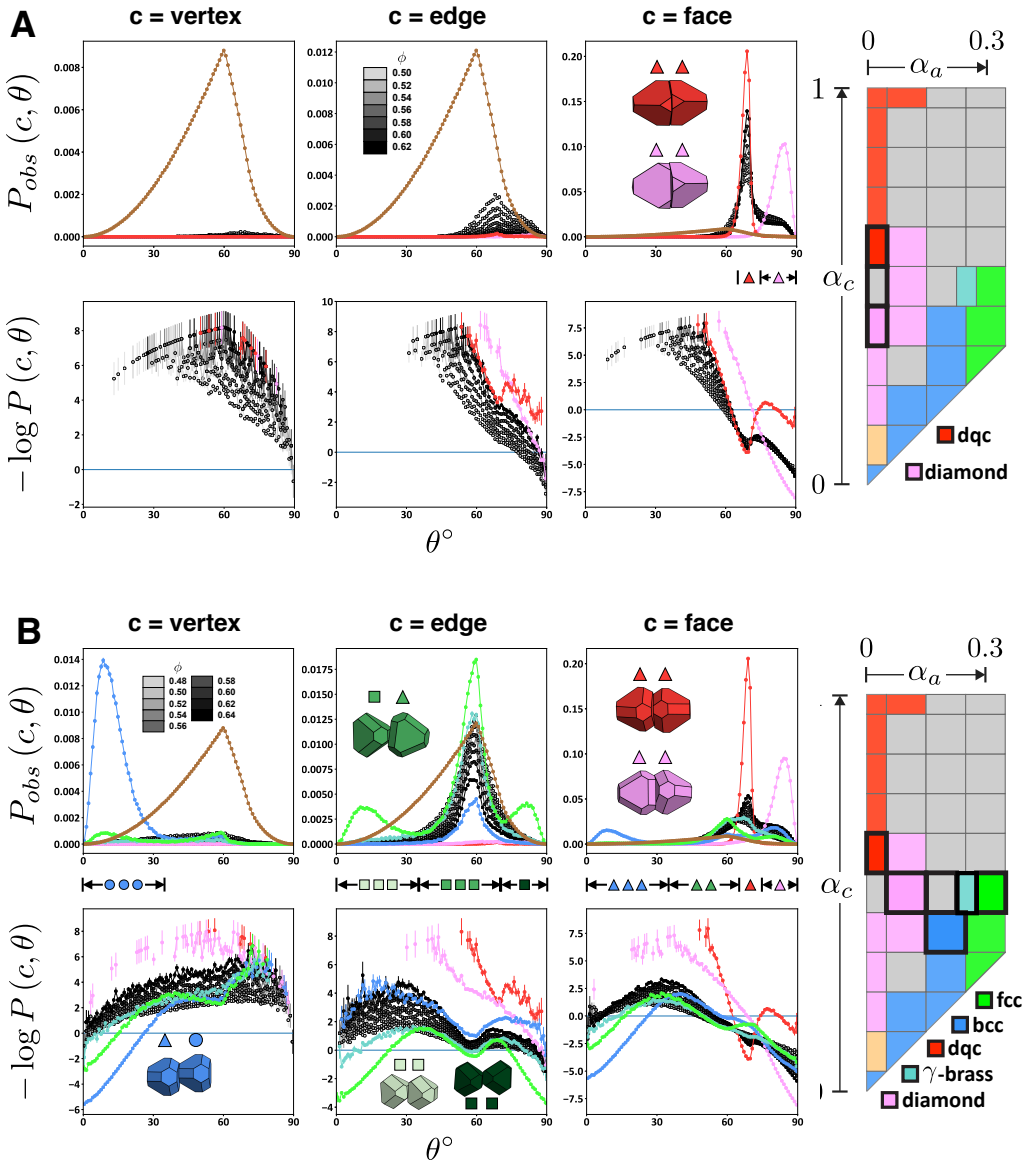


Figure 4.7: Pairwise motifs in example glass-formers compete, and are found to dominate in ordered structures self-assembled from shapes nearby in shape space. Figures show probabilities of observing certain pairwise configurations, $P_{obs}(c,\theta)$, and the negative log of the normalized distributions, $-\log P(c,\theta)$, for disordered systems at the indicated densities and nearby crystals at $\phi = 0.62$ (or $\phi = 0.6$ for $\gamma$-brass). (A) Competition between face-connected aligned and twisted motifs at $(\alpha_a, \alpha_c) = (0, 0.5)$. Motifs are prevalent in nearby diamond and dodecagonal quasicrystal (dqc) structures. (B) Competition between face-connected aligned and twisted motifs and a face-edge connected motif at $(\alpha_a, \alpha_c) = (0.2, 0.5)$. Motifs are prevalent in nearby diamond, dodecagonal quasicrystal (dqc), *fcc*, and $\gamma$-brass structures.

crystal; more specifically, the *bcc* crystal is characterized by the pairwise motif (drawn in blue) consisting of two particles with a face-vertex connection and a misorientation $\theta = 0°$. Regarding edge-connection, the disordered system has a local basin in $-\log P(e, \theta)$ around 58° that persists at all densities, although the number of edge-connections in the disordered system decreases as density increases. This basin is characteristic of the nearby *fcc* crystal, and corresponds by inspection to the pairwise motif drawn in green, consisting of an edge-face connection in which the edge of one particle bisects the face of its nearest neighbor. A perfectly-constructed pair with this configuration has misorientation $\theta \sim 54.74°$. (The *fcc* structure also shows basins in $-\log P(e, \theta)$ around $\theta = 0°$ and $\theta = 90°$. By inspection, these basins correspond to the pairwise configurations drawn in dark green and light green. They do not appear with any significance in the dense fluid at any density, however.) In terms of face-connection, the disordered system shows a basin in $-\log P(f, \theta)$ around 58°, which becomes less significant as density increases, and basins around 70° and 90°, which become more significant as density increases. The basin around 58° corresponds to the other half of the aforementioned face-edge connected motif that is characteristic of *fcc* and drawn in green. The basin around 70° corresponds to the face-connected aligned pairwise configuration, drawn in red, that is characteristic of the nearby dodecagonal quasicrystal. The basin around 90° corresponds to the face-connected twisted pairwise configuration, drawn in pink, that is characteristic of the nearby diamond structure. Thus, motifs that are characteristic of nearby crystal structures are shown to coexist in the disordered fluid at all investigated densities.

## 4.6 Local structure in fluids across the shape landscape

We next consider the varying abundance, across the entire shape space, of the motifs we identified in the previous section as important structural characteristics of select glass-formers and nearby crystals. We examine motif fractions in pre-cursor and

disordered fluids only. We find that motifs are generally more abundant in disordered or pre-cursor fluids in regions of shape space in which fluids tend to self-assemble into the crystals associated with those motifs. Thus, (i) the motifs associated with *bcc* are strongly suppressed in all fluids except near the $\alpha_a = \alpha_c$ line, where vertex truncation is highest, (ii) motifs associated with *fcc* are more abundant in regions with higher $\alpha_a$, or edge truncation, (iii) the quasicrystal motif is more abundant near the $(\alpha_a, \alpha_c) = (0, 1)$ corner of shape space corresponding to a non-truncated tetrahedron, and (iv) the diamond motif is more abundant near the $(\alpha_a, \alpha_c) = (0, 0.35)$ location in shape space that corresponds to a vertex-truncated tetrahedron.

Figs. 4.8 and 4.9 show fractions of these motifs across the shape landscape in disordered or pre-cursor fluids at densities of $\phi = 0.56$ and $\phi = 0.6$, respectively. We identified pre-cursor fluids in all cases as all frames of self-assembling trajectories prior to the nucleation incubation time, discussed previously. As density increases, the regions in which the *bcc* and *fcc* motifs are abundant become smaller and more concentrated near the $\alpha_a = \alpha_c$ line and at higher $\alpha_a$ values respectively. Conversely, the regions of quasicrystal and diamond structure motif abundance grow as density increases, and they grow in directions in which the corresponding crystals still self-assemble at higher density. The behavior of all regions as density increases makes sense in the context of locally dense packing arguments in hard particle fluids [37]: vertex/edge connected motifs only appear in systems in which particle vertex/edge truncation is significant, and these connection types are suppressed as density increases because face connection is enhanced as density increases. Face connection provides higher locally dense packing of particle pairs.

Note that particles on the diagonal of the shape landscape, where $\alpha_a = \alpha_c$, have octahedral symmetry rather than tetrahedral symmetry. Thus, their set of possible misorientation angles is different: in particular, it is not possible for particles with this symmetry to have misorientation angles between $\sim 65°$ and $90°$, so systems of these

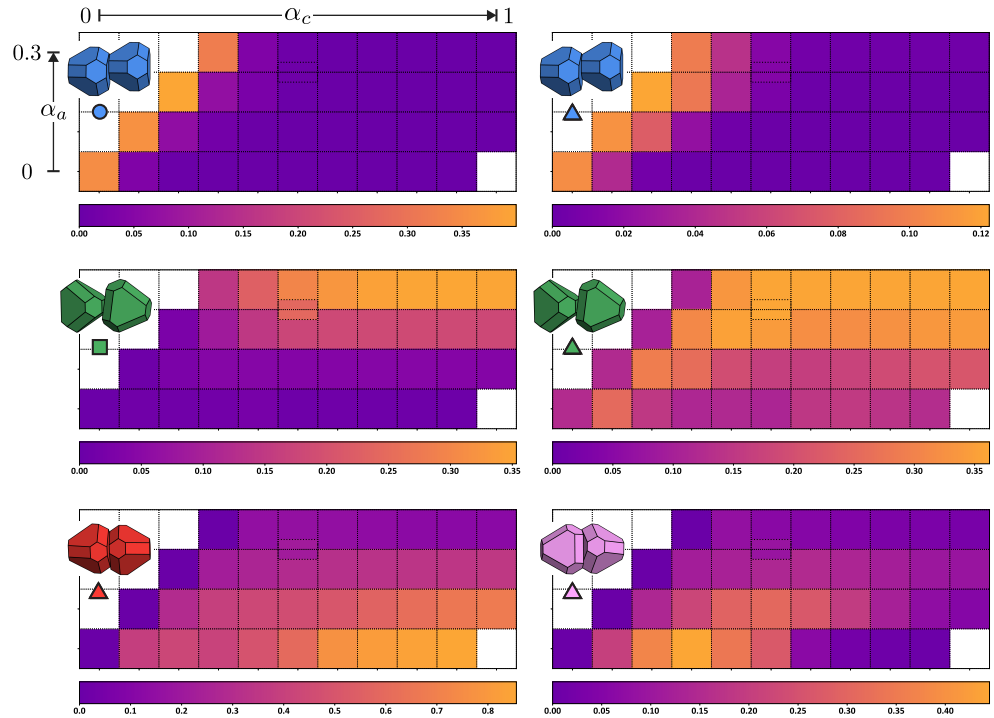


Figure 4.8: Motif fractions in disordered or pre-cursor fluids across the shape landscape at $\phi = 0.56$. Color bars below each panel show corresponding motif fraction limits. The motif whose abundance is displayed in each panel is drawn in its upper left corner, with a symbol below it indicating its connection type. $\alpha_a$ and $\alpha_c$ limits are shown for the upper left panel, and apply to all other panels. Regions of shape space are left un-filled if data at the centers of those regions is not available at $\phi = 0.56$.

particles somewhat artificially display zero motifs associated with the dodecagonal quasicrystal or diamond structure.

### 4.6.1 Local structure near glass-forming state points

The above analysis demonstrates that different motifs are abundant in fluids in distinct regions of shape space, each of which has a tendency to self-assemble into a characteristic crystal structure. Glass-forming fluids lie approximately between these regions, and thus contain not-insignificant motif fractions corresponding to multiple crystals.

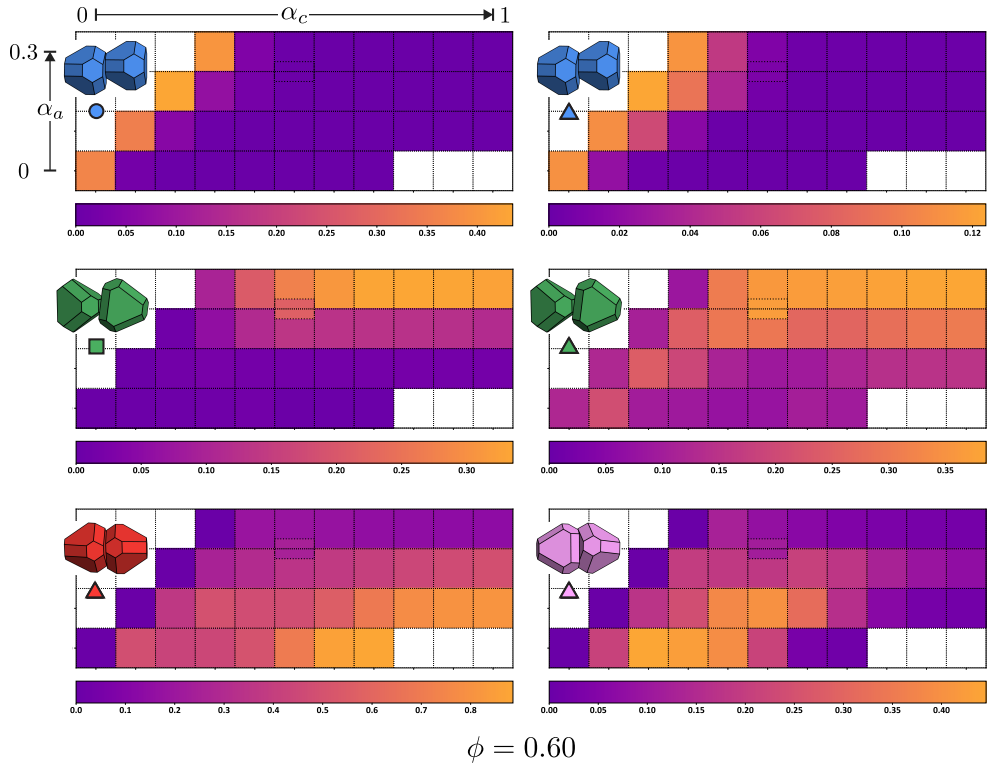


Figure 4.9: Motif fractions in disordered or pre-cursor fluids across the shape landscape at $\phi = 0.6$. Color bars below each panel show corresponding motif fraction limits. The motif whose abundance is displayed in each panel is drawn in its upper left corner, with a symbol below it indicating its connection type. $\alpha_a$ and $\alpha_c$ limits are shown for the upper left panel, and apply to all other panels. Regions of shape space are left un-filled if data at the centers of those regions is not available at $\phi = 0.6$.

We now tighten our focus, and consider the structural differences between the glass-forming fluids at $(\alpha_a, \alpha_c) = (0, 0.5)$ (Fig. 4.11) and $(\alpha_a, \alpha_c) = (0.2, 0.5)$ (Fig. 4.12) and pre-cursor fluids that form crystals nearby in shape space. Fig. 4.11 shows motif fractions as a function of density for the glass-forming fluid at $(\alpha_a, \alpha_c) = (0, 0.5)$ and the nearby (pre-cursor) crystal-forming fluids at $(\alpha_a, \alpha_c) = (0, 0.4)$, $(\alpha_a, \alpha_c) = (0, 0.6)$, and $(\alpha_a, \alpha_c) = (0.1, 0.5)$. The fluid at $(\alpha_a, \alpha_c) = (0, 0.4)$ coexists with the diamond structure at $\phi = 0.54$, and assembles solely the diamond structure at $0.56 \leq \phi \leq 0.62$. The fluid at $(\alpha_a, \alpha_c) = (0, 0.6)$ assembles into the dodecagonal quasicrystal at $\phi = 0.6$; shown here is a trajectory at the same state point that did not assemble into the quasicrystal on the time scale of our simulation, but for which we collected ample data in the fluid regime. We believe that, at long enough times, the system shown here would assemble into the quasicrystal, since (i) assembly was observed in a system that differed from this one only by its random initial conditions, (ii) the assembled quasicrystal was found to be stable at densities as low as $\phi = 0.56$ according to the melting studies detailed earlier, and (iii) the assembled quasicrystal has a motif stoichiometry that is very similar to the fluid one shown here. Fig. 4.10 compares motif stoichiometry and system pressure for the fluid shown here and the assembled dqc at this state point. Fig. 4.12 shows motif fractions as a function of density for the glass-forming fluid at $(\alpha_a, \alpha_c) = (0.2, 0.5)$ and the nearby pre-cursor crystal-forming fluids at $(\alpha_a, \alpha_c) = (0.1, 0.5)$, $(0.2, 0.4)$, $(0.25, 0.5)$, and $(0.3, 0.5)$. The fluid at $(\alpha_a, \alpha_c) = (0.1, 0.5)$ assembles into diamond at $0.62 \leq \phi \leq 0.64$. The fluid at $(\alpha_a, \alpha_c) = (0.2, 0.4)$ assembles into *bcc* at $0.58 \leq \phi \leq 0.64$, although at $\phi = 0.64$ it is still assembling into *bcc* at the end of our simulation. The fluid at $(\alpha_a, \alpha_c) = (0.25, 0.5)$ assembles into $\gamma$-brass at $\phi = 0.6$. The fluid at $(\alpha_a, \alpha_c) = (0.3, 0.5)$ assembles into *fcc* at $0.58 \leq \phi \leq 0.6$.

We ran three or four replicate simulations at each density for the $(\alpha_a, \alpha_c) = (0, 0.4)$, $(0.1, 0.5)$, $(0.2, 0.4)$, $(0.25, 0.5)$, and $(0.3, 0.5)$ systems, to collect more statistics in the

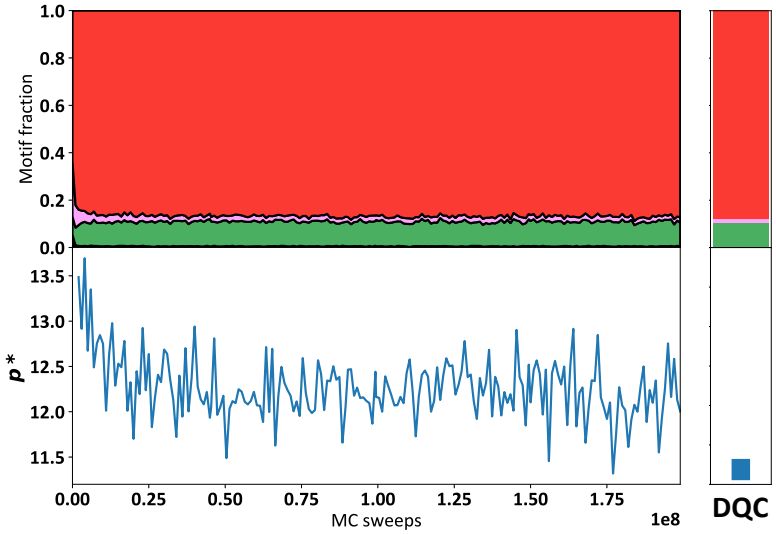


Figure 4.10: Dimensionless pressure and motif fraction for a trajectory at $(\alpha_a, \alpha_c, \phi) = (0, 0.6, 0.6)$ which did not crystallize, and a crystallized dodecagonal quasicrystal (DQC) at this state point. Pressure and motif fraction for the DQC are shown in the right-most panel. Error bars in the pressure of the DQC are smaller than the marker size. Motif fractions of the DQC are very similar to those of the non-assembling trajectory, and pressure is lower in the crystallized system.

pre-cursor fluid regime. Motif fractions are ensemble-averaged over all fluid frames and shown with error bars indicating the associated standard deviation of the mean. For the crystal-forming fluids, motif fractions are plotted both for the pre-cursor fluid stage of those trajectories and for the crystalline stage of those trajectories, when applicable. In the case of the crystalline stage, motif fractions are ensemble-averaged over the final 5 frames of all crystallizing replicates and shown with error bars indicating the associated standard deviation of the mean. Frames in all trajectories are written at a frequency of once per 1 million MC sweeps.

Fig. 4.11 is rather straight-forward, and shows that at densities relevant to crystallization, the disordered fluid at $(\alpha_a, \alpha_c) = (0, 0.5)$ contains fewer motifs associated with the diamond structure than nearby fluids that assemble into diamond, and fewer motifs associated with the dodecagonal quasicrystal than the nearby fluid that is capable of assembling into the dodecagonal quasicrystal. Thus, the disordered fluids are structurally different than nearby fluids that assemble into crystal structures, and reflect a higher competition between the face-to-face twisted (pink) motif associated with the diamond structure and the face-to-face aligned (red) motif associated with the dodecagonal quasicrystal. In both panels (B) and (C), at high enough densities, the fraction of twisted face-to-face pairwise motifs shown in dashed pink triangles is high enough to promote self-assembly into the diamond structure, at which point the aligned face-to-face motif shown in dot-dash red triangles is strongly suppressed in favor of the twisted face-to-face motif shown in dot-dash pink triangles. We observe some portion of the particles in the motif indicated by green triangles, associated with the *fcc* structure, in all systems at all densities. However, plots of $P_{obs}(f, \theta)$ for these systems show that this is essentially just an artifact of imposing cut-offs on the misorientation angle to define our motifs- these systems do not have any special spike in probability near 58°, the misorientation angle associated with the face-edge connected *fcc* motif.

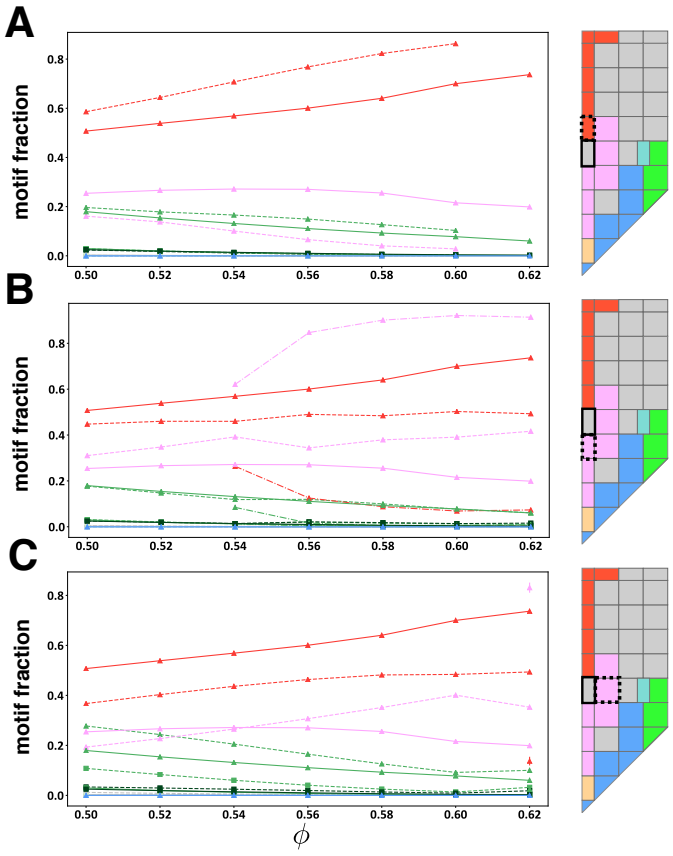


Figure 4.11: Motif fraction as a function of packing fraction for the disordered fluid at $(\alpha_a, \alpha_c) = (0, 0.5)$ and nearby crystal-formers. Solid lines indicate motif fractions for disordered systems, dashed lines indicate motif fractions in fluids of nearby crystal-forming systems, and dot-dash lines, where shown, indicate motif fractions in assembled crystals of nearby crystal-forming systems. The location of each disordered system is outlined in a solid line in the shape space image to the right of each panel, and the location of the crystal-forming system is outlined in a dashed line. Plots show that disordered fluids and crystal-forming fluids contain different ratios of motifs in all cases, with crystal-forming fluids in general containing higher fractions of the motifs that dominate in the assembled structures. Motif fractions are shown for the disordered system at $(\alpha_a, \alpha_c) = (0, 0.5)$ and crystal-formers at (A) $(\alpha_a, \alpha_c) = (0, 0.6)$ (although this trajectory did not self-assemble into the quasicrystal during our simulation, an identical state point with different random initial conditions did; see the main text for more detail), (B) $(\alpha_a, \alpha_c) = (0, 0.4)$, and (C) $(\alpha_a, \alpha_c) = (0.1, 0.5)$.

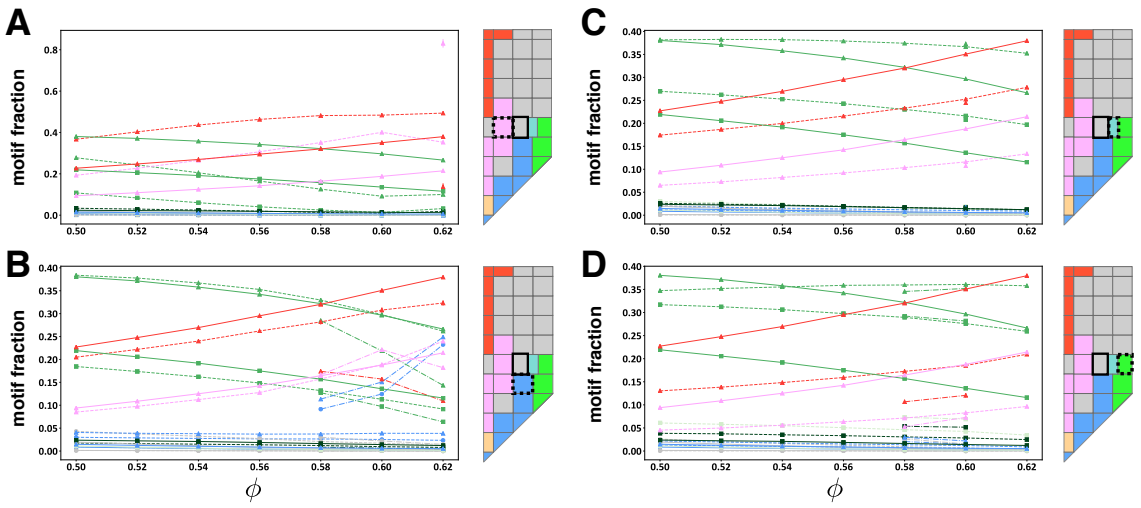


Figure 4.12: Motif fraction as a function of packing fraction for the disordered fluid at $(\alpha_a, \alpha_c) = (0.2, 0.5)$ and nearby crystal-formers. Solid lines indicate motif fractions for disordered systems, dashed lines indicate motif fractions in fluids of nearby crystal-forming systems, and dot-dash lines, where shown, indicate motif fractions in assembled crystals of nearby crystal-forming systems. The location of each disordered system is outlined in a solid line in the shape space image to the right of each panel, and the location of the crystal-forming system is outlined in a dashed line. Plots show that disordered fluids and crystal-forming fluids contain different ratios of motifs in all cases, with crystal-forming fluids in general containing higher fractions of the motifs that dominate in the assembled structures. Motif fractions are shown for the disordered system at $(\alpha_a, \alpha_c) = (0.2, 0.5)$ and crystal-formers at (A) $(\alpha_a, \alpha_c) = (0.1, 0.5)$, (B) $(\alpha_a, \alpha_c) = (0.2, 0.4)$, (C) $(\alpha_a, \alpha_c) = (0.25, 0.5)$, and (D) $(\alpha_a, \alpha_c) = (0.3, 0.5)$.

Fig. 4.12 is more complicated, due to the presence of more types of pairwise motifs in systems in this region of shape space, but nevertheless portrays a similar story to Fig. 4.11. At densities relevant to crystallization, the disordered system at $(\alpha_a, \alpha_c) = (0.2, 0.5)$ contains fewer motifs associated with the diamond structure than the nearby fluid that assembles into diamond, fewer motifs (almost none in this case) associated with the *bcc* structure than the nearby fluid that assembles into bcc, and fewer motifs associated with the *fcc* structure than the nearby fluids that assemble into $\gamma$-brass and *fcc*. (Whether the system assembles into $\gamma$-brass or *fcc* seems to depend on the precise cocktail of motifs in the pre-cursor fluids at appropriate densities.) We also point out that the disordered system contains about half as many motifs associated with the dodecagonal quasicrystal than the fluid at $(\alpha_a, \alpha_c) = (0, 0.6)$, which is capable of assembling the quasicrystal. Thus, the disordered fluids are structurally different than nearby fluids that assemble into crystal structures, and reflect a higher competition between the face-to-face twisted (pink) motif associated with the diamond structure, the edge-to-face (green) motifs associated with the fcc structure, and the face-to-face aligned (red) motif associated with the nearby quasicrystal. (In panel (D), we also note the non-negligible presence in the *fcc*-forming fluid of the edge-connected motifs shown as light and dark green squares, also associated with the *fcc* structure. These motifs are more suppressed in the disordered fluid at all densities.)

## 4.7 Doping simulations

We next demonstrate that the incompatible motifs found in the glass-forming fluid at $(\alpha_a, \alpha_c) = (0, 0.5)$ compete with one another sufficiently to hinder crystallization. Evidently, the fraction of particles forming twisted motifs in the pre-cursor diamond-forming fluid is high enough to drive crystallization into diamond at appropriate densities, and the fraction of particles forming aligned motifs in the pre-cursor quasicrystal-forming fluid is high enough to drive self-assembly into the dodecagonal

quasicrystal at appropriate densities. By contrast, the glass-forming fluid exhibits a significant fraction of both motifs, preventing either crystal from forming.

We verified that the twisted motif fraction shown in the pre-cursor fluid of the diamond-former was necessary for crystallization into diamond via a set of "doping simulations" in which we artificially inserted the face-connected aligned motif (associated with the quasicrystal) into the diamond-forming fluid at $(\alpha_a, \alpha_c) = (0, 0.4)$, and the twisted motif (of the diamond crystal) into disordered fluids at $(0, 0.5)$ and $(0, 0.55)$. For these simulations, we rigidly connected a fraction $\eta_d$ of particles in each dense fluid into pairs to form the relevant dimer motifs, and ran simulations at densities $\phi = 0.54$ and $\phi = 0.56$ for $\eta_d$ ranging from 0.05 to 1.0. Via this mechanism, we were able to either artificially enhance or suppress the fraction of particles forming twisted pairwise motifs, and observe consequent assembly or non-assembly behavior. Our results are summarized in Fig. 4.13A, which shows twisted motif fraction as a function of packing fraction for (pre-cursor) fluids of doped and undoped systems. Symbols are colored pink if the system self-assembles into diamond on the time scales of our simulation at that state point. Pink symbols only appear at twisted motif fractions above the threshold established by the diamond-forming undoped system at $(\alpha_a, \alpha_c) = (0, 0.4)$, indicated by circles connected by a black line, for all investigated locations in shape space and doping schemes. At the point in shape space $(\alpha_a, \alpha_c) = (0, 0.4)$, introduction of the aligned motif of the quasicrystal causes assembly failure in the would-be diamond-former when $\eta_d \geq 0.25$. For the doping schemes in which crystallization is thwarted, the fraction of particles in the twisted motif is observed to be below the threshold shown by the diamond-forming undoped system. At $(\alpha_a, \alpha_c) = (0, 0.5)$ and $(\alpha_a, \alpha_c) = (0, 0.55)$, introduction of the twisted motif of diamond to the disordered fluids causes crystallization into diamond at $\eta_d \geq 0.25$ and $\eta_d \geq 0.75$, respectively. For these crystallization-inducing doping schemes, the fraction of particles in the twisted motif is observed to be above the threshold established

by the diamond-forming undoped system at $(\alpha_a, \alpha_c) = (0, 0.4)$. Previous studies have additionally shown that systems composed entirely of aligned motifs made of non-truncated tetrahedra [190] and tetrahedra with a slightly modified vertex truncation [191] assemble the dodecagonal quasicrystal at long times under various simulation strategies. This provides some evidence that the aligned motif is capable of promoting self-assembly into the dodecagonal quasicrystal. Thus, the competition between the high fractions of twisted and aligned face-to-face motifs in the glass-forming fluid at $(\alpha_a, \alpha_c) = (0, 0.5)$ seems to be responsible for its failure to crystallize, since this competition can be artificially tuned to promote self-assembly in systems that may otherwise vitrify, or suppress self-assembly in systems that may otherwise crystallize. (Note that some schemes, even though they impose high twisted motif fractions above the threshold, do not result in assembly into diamond. This is due probably to longer relaxation times associated with polydisperse systems and systems containing extended rigid bodies.) Fig. 4.13B shows a phase diagram summarizing the results of all doping simulations.

We also attempted to dope systems near $(\alpha_a, \alpha_c) = (0, 0.5)$ with the aligned motif, to coax them into forming the dodecagonal quasicrystal, and to dope systems at $(\alpha_a, \alpha_c) = (0.2, 0.5)$ with motifs dominant in nearby *bcc*, *fcc*, and diamond structures, to manipulate them into forming those crystals. However, we were unsuccessful in those attempts, indicating perhaps that appropriate local structure is a necessary but not sufficient condition for crystallization, at least on the time- and size-scales of our simulations.

## 4.8 Alchemical Monte Carlo

We provide additional evidence that an identity crisis in alchemical space promotes glass formation in hard particle fluids by allowing disordered systems to explore their surrounding shape space through alchemical Monte Carlo (Alch-MC) sampling [40],

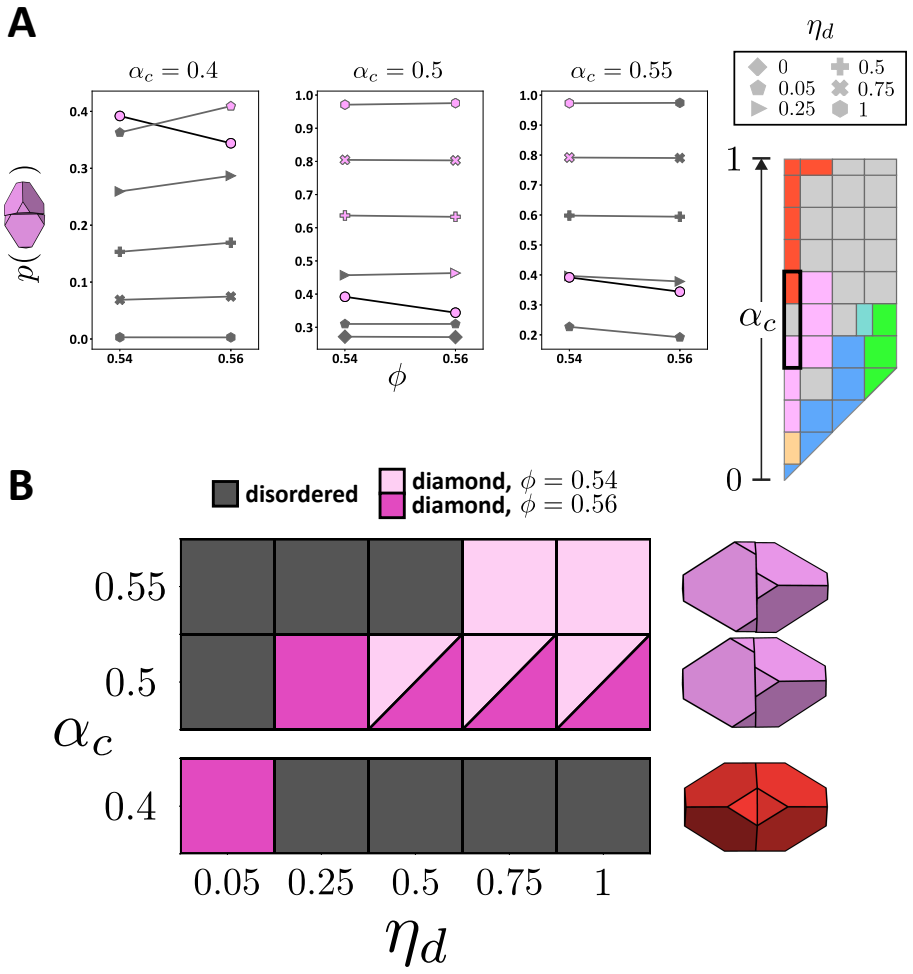


Figure 4.13: Disordered fluids and crystal-forming fluids are structurally different, and this fluid structure can be tuned to promote or suppress crystallization. Systems are identified by $\alpha_c$, indicating their location in shape space at $(\alpha_a, \alpha_c) = (0, \alpha_c)$, and the relevant location in shape space is outlined in black in the image to the right of the plots. (A) Doping via the introduction of rigid local structural motifs into dense fluids influences assembly behavior, causing crystallization for systems that might otherwise vitrify, and vitrification for systems that otherwise crystallize. Panels show twisted motif fraction for (pre-cursor) fluids during doping experiments at different locations in shape space. Symbols indicate different dopant fractions $\eta_d$. The dopant dimer is the twisted motif for $\alpha_c = 0.5$ and $\alpha_c = 0.55$, in which case doping promotes self-assembly into the diamond structure. For $\alpha_c = 0.4$, the dopant dimer is the aligned motif, in which case doping disrupts self-assembly into the diamond structure. Symbols are colored pink if the system self-assembles into diamond on the time scales of our simulation. The threshold for assembly established by the undoped system at $(\alpha_a, \alpha_c) = (0, 0.4)$ is indicated by circles connected by a black line. (B) A phase diagram summarizes results of our doping simulations. The associated dopant dimer configuration is shown to the right of each row of doping results. Boxes are colored according to whether simulations remain disordered at both $\phi = 0.54$ and $\phi = 0.56$, assemble into diamond at $\phi = 0.54$, or assemble into diamond at $\phi = 0.56$.

as detailed in Chapter II. In this technique, particle shape (defined in this case by the truncation parameters $\alpha_a$ and $\alpha_c$) is treated as a thermodynamic variable, and allowed to fluctuate in a generalized thermodynamic ensemble at constant (zero) conjugate alchemical potential. In each simulation, all particle shapes were identical and sampled simultaneously. We sampled disordered systems at $(\alpha_a, \alpha_c) = (0, 0.5)$ and $(0.2, 0.5)$ via Alch-MC at a range of densities between $\phi = 0.52$ and $\phi = 0.64$. At each density, we ran simulations in which we allowed only the vertex truncation parameter $\alpha_c$, only the edge truncation parameter $\alpha_a$, or both to fluctuate. We constrained systems to only explore the area inside a square of side length $\Delta\alpha = 0.2$ centered at their initial position in shape space by imposing appropriate limits on each $\alpha$ parameter during sampling.

Figure 4.14 shows results for alchemical sampling in both example glass-forming systems. All simulations shown are at $\phi = 0.62$, except the case of edge truncation sampling at $(\alpha_a, \alpha_c) = (0.2, 0.5)$, which is shown at $\phi = 0.60$ (the equivalent Alch-MC simulation at $\phi = 0.62$ failed to crystallize on the time scale of our simulations). Instead of forming a glass, each disordered system now crystallizes into a "nearby" ordered structure by slightly altering its particle shape and accordingly adopting a larger fraction of the associated crystalline pairwise motif. Thus we see that, given the thermodynamic choice, these hard particle fluids escape schizophrenic regions of shape space, and assemble into nearby crystalline structures typically dominated by one motif.

## 4.9 The identity crisis in the 423 family

Finally, we show that our identity crisis hypothesis is independent of particle symmetry and adjacent crystal structure by investigating another glass-forming system in a different shape space, defined by the spheric triangle invariant 423 family [113, 176]. This glass-former consists of hard particles with octahedral symmetry,

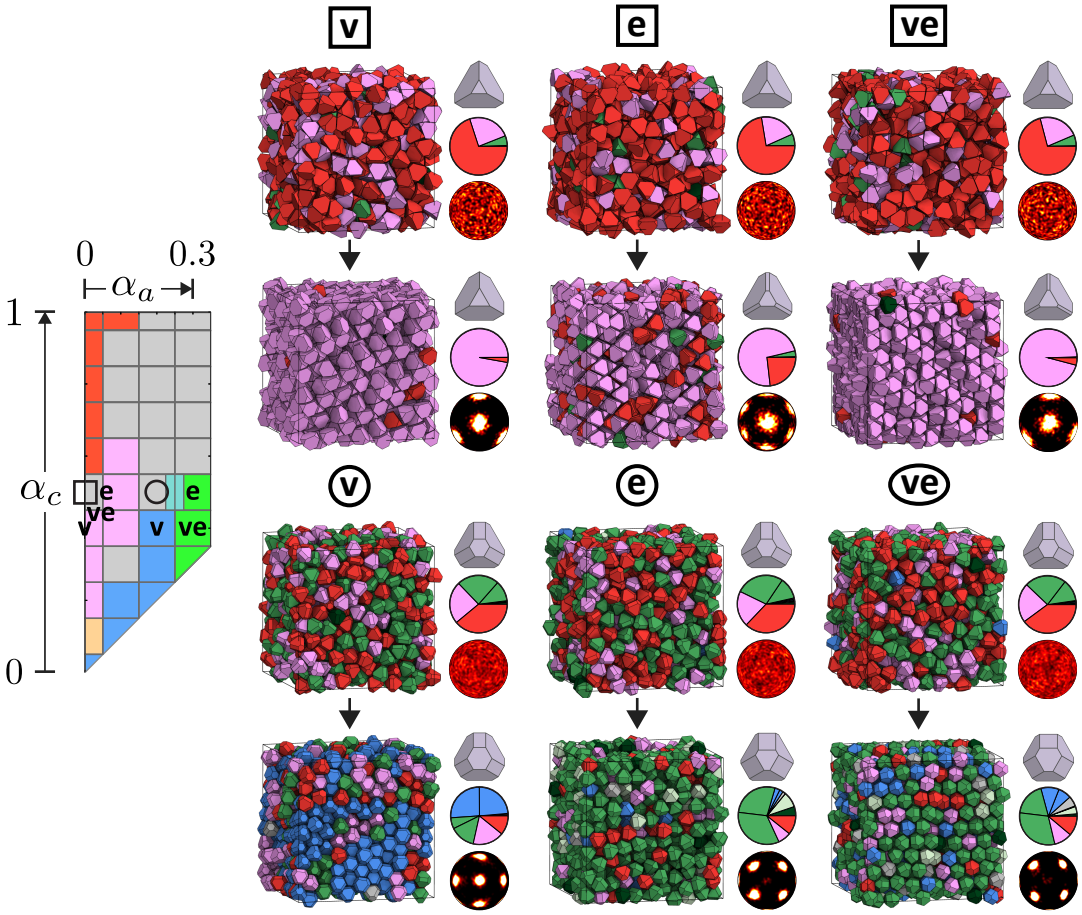


Figure 4.14: Would-be glass-formers escape their identity crisis and crystallize when allowed to explore their surrounding shape space via alchemical Monte Carlo simulation. Squares indicate simulations at the glass-forming state point $(\alpha_a, \alpha_c) = (0, 0.5)$, while circles correspond to simulations at $(\alpha_a, \alpha_c) = (0.2, 0.5)$. Empty symbols overlaid above the shape space indicate system position at the start of Alch-MC sampling, and letters indicate system position after 20-30 million MC sweeps of vertex truncation (**v**), edge truncation (**e**), or both vertex and edge truncation (**ve**) sampling. System snapshots, particle shapes, pie charts of pairwise motif fractions, and bond-order diagrams are shown for initial and final frames of each Alch-MC simulation. Pie chart wedges are colored according to the motifs identified in Fig. 4.7. Wedges colored gray represent (connection type, $\theta$) regimes that were not identified with any crystal structure. Pie chart wedges colored identically represent motifs characteristic of the same crystal structure that differ only by connection type. In those cases, the motif with face connection is always drawn second, proceeding in a counter-clockwise fashion. The hexagonal bond-order diagram resulting from edge Alch-MC sampling at $(\alpha_a, \alpha_c) = (0, 0.5)$ is a consequence of wurtzite-like structural motifs due to the presence of stacking faults in the system. Crystalline structures resulting from edge and vertex-edge Alch-MC sampling at $(\alpha_a, \alpha_c) = (0.2, 0.5)$ contain multiple grains and stacking faults; associated bond-order diagrams show the local environment of particles in just a single grain. In all cases shown, disordered dense fluids avoid vitrification and instead form crystals dominated by a single pairwise motif.

located in a shape space region surrounded by shapes that form either *bcc* or a high-pressure Lithium phase that is likely metastable to *bcc* [176]. As expected from the above findings, we observed two competing motifs in this glass-former, each dominant in the nearby *bcc* or metastable high-pressure Lithium structures. We allowed the glass-former to explore its immediate surroundings in shape space through Alch-MC sampling, and observed that it escaped its identity crisis by adopting a nearby particle shape that forms *bcc*.

The spheric triangle invariant 423 family of polyhedra is formed by truncating the vertices and edges of an octahedron by sets of planes at varying radial distances from the polyhedron center. As we did for the 323 family, we define truncation parameters $\alpha_a$ and $\alpha_c$ such that $(\alpha_a, \alpha_c) = (0, 0)$, denoting a cuboctahedron, $(\alpha_a, \alpha_c) = (0, 1)$, denoting a cube, $(\alpha_a, \alpha_c) = (1, 1)$, denoting a rhombic dodecahedron, and $(\alpha_a, \alpha_c) = (1, 0)$, denoting an octahedron, form the corners of this shape space. Fig. 4.15A shows the full shape space, with representative polyhedra superimposed above their corresponding positions in the space. It was previously found that at certain locations in this shape space near the octahedron corner $(\alpha_a, \alpha_c) = (1, 0)$, systems failed to assemble into any ordered structure at densities ranging from $\phi = 0.50$ to 0.65, while at nearby locations, *bcc* or occasionally high-pressure Lithium formed only at high packing fractions at or above $\phi = 0.6$ [176].

We investigated the region near the octahedral corner of this shape space using Monte Carlo methods identical to those described in Section 4.11.1. Our results are shown in Fig. 4.15A. They agree generally with the aforementioned previous results; we found that three state points failed to assemble on the 100 million MC sweep time scale of our simulations, for densities $\phi = 0.56, 0.58, 0.6, 0.62$, and 0.64. At four state points, also simulated at $\phi = 0.56, 0.58, 0.6, 0.62$, and 0.64, only *bcc* formed at $\phi \geq 0.6$. At the remaining two state points, those that were previously found to assemble into high-pressure Lithium at $\phi = 0.61$[176], we ran five replicate simulations each at

$\phi = 0.6$, 0.61, and 0.62, and indeed found that high-pressure Lithium occasionally formed at these state points only at $\phi = 0.61$. For $\phi = 0.6$ and 0.62, only *bcc* formed. At $(\alpha_a, \alpha_c) = (0.9, 0.05)$, Lithium formed in three of the five replicate simulations at $\phi = 0.61$, and transitioned to *bcc* over the course of the simulation in two of those three cases. The remaining replicate simulations assembled into *bcc* outright. At $(\alpha_a, \alpha_c) = (0.95, 0.05)$, Lithium formed in two of the five replicate simulations at $\phi = 0.61$, and transitioned to *bcc* over the course of the simulation in both cases. Two of the remaining three replicates formed *bcc* outright, while the final replicate remained disordered.

We tested for the stability of the high-pressure Lithium structure at every investigated state point by running melting simulations in which we initialized our systems in the Lithium structure at packing fractions ranging from $\phi = 0.56$ to 0.64, and subsequently sampled in the isochoric ensemble for 39 to 61 million MC sweeps or until melting into *bcc* occurred. We ran three replicate simulations at each state point and each density. We additionally ran one corresponding simulation at each state point and density in which we tested for the stability of *bcc* in an identical manner. We found that, on these time scales, *bcc* was stable at all densities for all state points, and Lithium was stable at a subset of (higher) densities for all state points. We found that Lithium was stable at $\phi \geq 0.58$ for $(\alpha_a, \alpha_c) = (0.85, 0.05)$, $(0.9, 0.05)$, $(0.95, 0.05)$, and $(0.95, 0.1)$; at $\phi \geq 0.6$ for $(\alpha_a, \alpha_c) = (0.85, 0.1)$, $(0.9, 0.1)$, $(0.9, 0.15)$, and $(0.95, 0.15)$; and at $\phi \geq 0.62$ for $(\alpha_a, \alpha_c) = (0.85, 0.15)$. At other densities, all replicates of Lithium melted into *bcc*. The trend is clear: as edge and vertex truncation generally increase, and thus $\alpha_a$ decreases and/or $\alpha_c$ increases, Lithium is only stable at higher and higher densities.

These assembly and melting simulations demonstrate that high-pressure Lithium can form and remain stable in this region of shape space, especially at small edge and vertex truncations, but Lithium appears generally metastable to *bcc*.

Fig. 4.15B shows the results of pairwise motif identification for the disordered system at $(\alpha_a, \alpha_c) = (0.9, 0.1)$ and $\phi = 0.62$, as well as surrounding crystal structures. Motif fractions were found by averaging across all snapshots (separated by 1 million MC sweeps) for which systems were fully crystallized, or all snapshots in the case of the disordered system. The disordered system is dominated by two motifs, colored light and dark purple, that are each prevalent in nearby *bcc* (at $\phi = 0.62$) and Lithium (at $\phi = 0.61$) structures respectively. In direct parallel to the motifs that dominate the diamond structure and the dodecagonal quasicrystal within the 323 shape family, we call these the "twisted" and "aligned" motifs, respectively. The "aligned" motif, detailed in row 5 in Fig. 4.15B, dominates in a nearby Lithium structure and consists of two truncated octahedra face-to-face and rotated such that their truncated vertices are aligned. The "twisted" motif, detailed in row 4 in Fig. 4.15B, dominates in a nearby *bcc* structure and consists of two truncated octahedra face-to-face and rotated such that they have the same orientation, and thus their bonded faces are twisted 60° with respect to each other.

Fig. 4.15C shows a subset of results for alchemical Monte Carlo (Alch-MC) sampling at the disordered state point $(\alpha_a, \alpha_c) = (0.9, 0.1)$, at densities ranging from $\phi = 0.52$ to 0.64. We constrained each system to only explore the area inside a square of side length $\Delta\alpha = 0.1$ centered at its initial position in shape space. Self-assembly on our simulation time scales occurred at $\phi = 0.6$ when we allowed only vertex truncation $\alpha_a$ to fluctuate, at $\phi = 0.6$ and $\phi = 0.62$ when we allowed only edge truncation $\alpha_c$ to fluctuate, and at $\phi = 0.6$ when we allowed both $\alpha_a$ and $\alpha_c$ to fluctuate. In these simulations, disordered systems escaped into regions of larger truncation and assembled into *bcc*, with a larger fraction of their particles accordingly adopting the twisted motif.

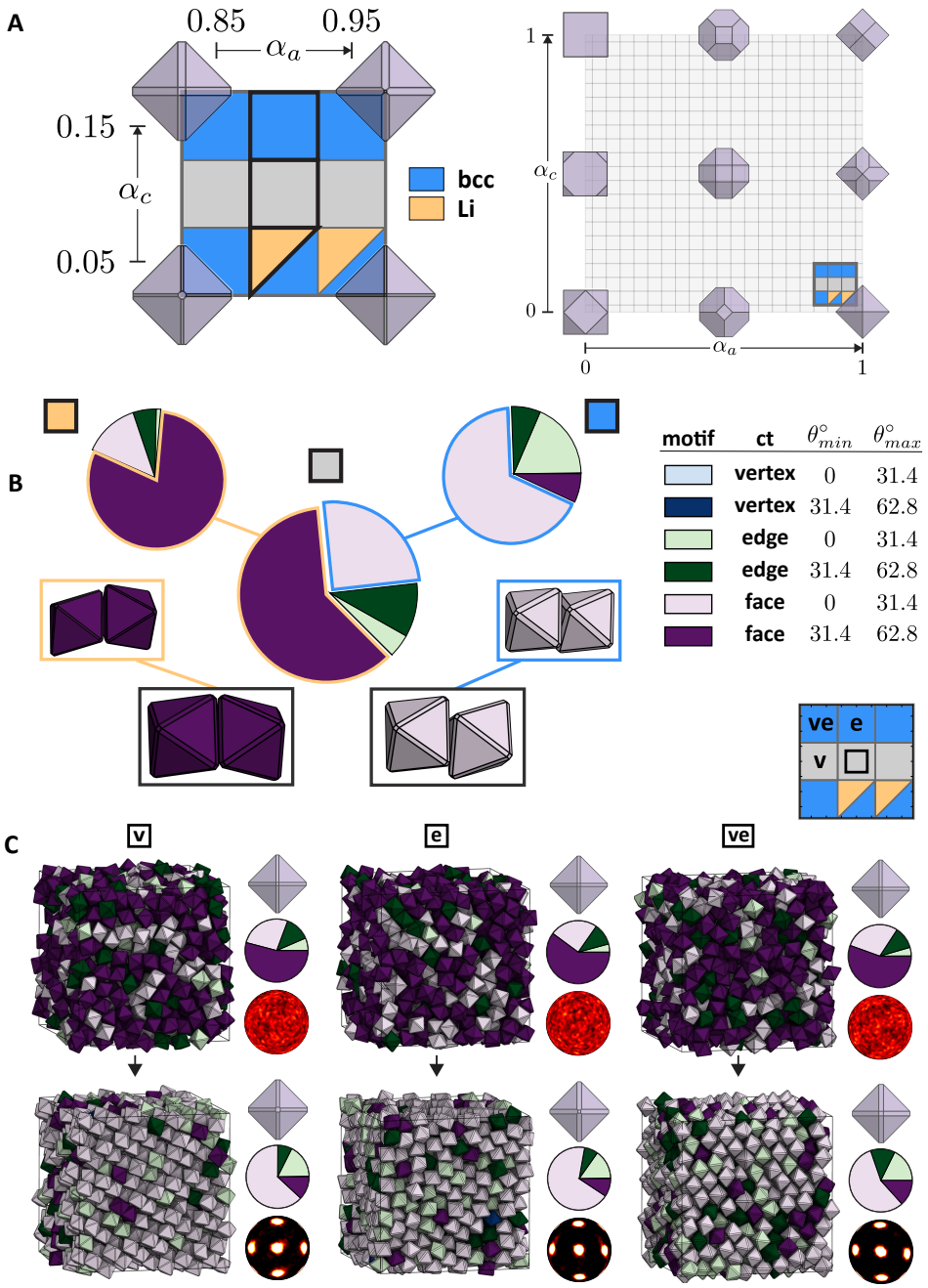


Figure 4.15: An identity crisis in the 423 shape family leads to disorder. (A) The full spheric triangle invariant 423 family, with the portion of the shape space explored in this study outlined. That portion is shown in greater detail, with sample particle shapes overlaid above corresponding regions of shape space, and regions colored according to their assembled structure. (B) Pairwise motifs in the disordered system at $(\alpha_a, \alpha_c) = (0.9, 0.1)$ compete, and are found to dominate in nearby ordered structures in shape space. Relevant locations in shape space are outlined in black in panel A. Motifs are listed in tabular form and color-coded according to their connection type **ct** and $\theta$ range. (C) The disordered system escapes its region of identity crisis and crystallizes when allowed to explore its surrounding shape space via Alch-MC. The empty square in the shape space diagram to the upper right indicates system position in shape space at the start of Alch-MC sampling, and letters indicate system position after 30-40 million MC sweeps of vertex truncation (**v**) sampling at $\phi = 0.6$, edge truncation (**e**) sampling at $\phi = 0.62$, or both vertex and edge truncation (**ve**) sampling at $\phi = 0.6$. System snapshots, particle shapes, pie charts of pairwise motif fractions, and bond-order diagrams are shown for initial and final frames of each Alch-MC simulation.

## 4.10 The identity crisis in context

Our results show that the concept of alchemical space is a useful lens through which to understand the vitrification of hard particle fluids. Crystallization fails in these systems due to the presence of multiple local structures, each of which is preferred in crystals formed by particles nearby in shape space. These structures compete by existing at ratios in the glass-formers that impede crystallization into any one crystal. Thus the entropic colloidal glass transition is caused by an identity crisis in shape space in which the glass-formers are unable to settle on any one particular set of local motifs consistent with a single crystal structure. In relation to other studies of local structures in glassy liquids, our findings most closely align with the results of Tanaka *et al.* [35, 175, 192], who posit that multiple types of ordering compete and suppress crystallization via the literal suppression of crystalline pre-cursors in supercooled liquids. Ref. [175] is especially relevant here: in that work, coauthors found that glass-forming ability is positively correlated with increased competition between multiple types of crystalline ordering, found near eutectic points when either the size ratio of a binary hard disk system or the strength of tetrahedrality in a modified Stillinger-Weber [193] model system is varied. Our results expand on these ideas in the context of hard-particle glass-formers: we find glass formation via multiple types of competing crystalline order on a very local level, each prevalent in nearby ordered structures in a two-dimensional alchemical landscape. Slightly modified particles have correspondingly modified preferences for assuming various local structural motifs, and thus serve as indicators of the competing preferences of the system under investigation.

The alchemical framework considered in this work may also be useful for understanding glass-formers in different contexts. Many previous studies have manipulated degrees of freedom in glass-forming systems to relieve or increase frustration. Stoichiometry in binary Lennard-Jones systems [194], polydispersity in two [160, 175] and

three[157] dimensions, salt concentration in a water-salt mixture [195], bias towards five-fold local ordering in two [173] and three [196] dimensions, bond tetrahedrality [175, 189], and even the curvature of three-dimensional space [197] have been tuned in pursuit of turning a glass-former into a crystal-former or vice-versa. In those cases, results typically show that local structures in frustrated glass-formers are related to local structures in one or more corresponding non-frustrated crystals. Considering these degrees of freedom as alchemical parameters, and their "tuning" as controlled exploration of alchemical space, may provide a useful unifying perspective.

## 4.11 Methods and protocols

### 4.11.1 Assembly simulations

To explore the self-assembly behavior of particles in the spheric triangle invariant 323 family, we sampled equilibrium behavior in the isochoric ensemble over a range of densities between $\phi = 0.48$ and $\phi = 0.64$. Simulations of 4,096 particles were run for about 100 million MC sweeps or until self-assembly was observed. Self-assembled phases were identified by eye and quantified by the bond-order diagram [198], radial distribution function, and diffraction pattern. At all state points corresponding to $\alpha_a < 0.3$ and $\alpha_c > 0.4$ for which self-assembly was not observed, we also simulated smaller systems of 2,624 particles for about 70-100 million MC sweeps. At one state point, $(\alpha_a, \alpha_c, \phi) = (0, 0.6, 0.6)$, self-assembly was observed around 120 million MC sweeps. To reach each density, we initialized our system in a sparse cubic array inside a cubic box, randomized the system by running isochoric Monte Carlo sampling for 10,000 MC sweeps, and progressively rescaled box vectors by a scale factor of 0.9995 until the target density was reached. After every rescaling step, isochoric Monte Carlo sampling proceeded until all particle-particle overlaps were eliminated. During the compression process, the translational trial move size was identical to its value during

equilibrium sampling, but the rotational trial move size was larger in order to facilitate the removal of overlaps during fast compressions to high densities. During equilibrium sampling, rotational and translational trial move sizes were constant across all systems studied, and were chosen to most efficiently structurally relax a typical system.

### 4.11.2 Dynamical characterization

To establish glass-forming behavior in our systems, we chose particle shapes that remain disordered on the long timescales of our simulations at the densities investigated to establish phase behavior, and re-sampled one-component systems of those shapes in a broader density range. We used Monte Carlo methods identical to those described in detail above. We equilibrated our systems for approximately 50 million MC sweeps, and then collected dynamical data for 100 million MC sweeps.

### 4.11.3 Crystal stability tests

To test the stability of candidate crystal structures at any location in shape space, we replaced the particles of a well-equilibrated simulation snapshot of that crystal at $\phi = 0.62$ with particles of the desired shape, while leaving particle positions and orientations unchanged. We then sampled in the isochoric ensemble to eliminate particle overlaps, isotropically enlarging the simulation box by a small scale factor every 10,000 MC sweeps if overlaps still existed. We subsequently compressed the system to some initial density between $\phi = 0.62$ and $\phi = 0.66$ in the manner detailed in Section 4.11.1, and allowed it to slowly melt. During the melting process, system densities were decreased in increments of $\Delta\phi = 0.01$ every 10 million MC sweeps. Step size tuning was performed during the melting process to maintain sampling efficiency.

Pressure was calculated using a volume perturbation technique [199–201] that extrapolates pressure in hard particle isochoric simulations through evaluations of the volume scaling needed to cause particle-pair overlaps throughout the system.

Its implementation in HOOMD-blue is detailed elsewhere [45, 202]. Melting of the crystal structures was determined by eye and corroborated by melting equations of state; for each melting event, pressure exhibited behavior characteristic of a phase transition, and often showed non-monotonic behavior in the form of Mayer-Wood loops [203, 204]. Three melting replicates were run for each state point.

Equations of state for each disordered, super-compressed fluid, shown in the upper left panel of Figs. 4.5 and 4.6, were determined from system snapshots used to calculate dynamical order parameters. At each density, pressure was calculated for 100 snapshots, taken every 1 million MC sweeps. Pressures for each snapshot were then ensemble averaged, and the equation of state shows these averages and associated standard deviations of the mean at each packing fraction. Pressure is reported in reduced units: $p^* \equiv \beta p \sigma^3$, where $\beta \equiv 1/k_B T$, $p$ is pressure, and $\sigma = 1$ is the characteristic length scale defined previously.

To test the stability of the high-pressure Lithium structure in the 423 family, we initialized in the Lithium structure via a compression scheme similar to that described in Section 4.11.1, with a few changes. We set up our particles in a high-pressure Lithium structure at very low packing fraction, then compressed quickly to the desired density with a very small translational trial move size and a much larger rotational trial move size, to ensure that the particles remained on-lattice during the compression.

### 4.11.4 Identity crisis analysis

Error bars in Fig. 4.7 were calculated as follows: histograms over $\theta$ for each connection type $c$ were accumulated for 10 frames (separated by 1 million MC sweeps), then $P_{obs}(c, \theta)$ was computed. Ensemble averages were taken over these values of $P_{obs}(c, \theta)$. These averages have an associated standard deviation that is shown as vertical error bars in plots of $P_{obs}(c, \theta)$, and that error was propagated via a first-

order Taylor series expansion of $-\log P(c,\theta)$, shown as vertical error bars in plots of $-\log P(c,\theta)$. Random distributions do not have associated error.

Motifs in ordered systems were calculated at $\phi = 0.62$, with the exception of the $\gamma$-brass crystal, for which motifs were calculated at $\phi = 0.6$. To gather statistics on motifs in relevant ordered systems at $\phi = 0.62$, we began with already well-equilibrated, self-assembled system snapshots of $N = 4,096$ particles, and sampled them in the isochoric ensemble for 100 million more MC sweeps. For several state points, we began with snapshots at lower packing fractions than $\phi = 0.62$, because they represented cleaner samples of the ordered structures of interest that assembled on the timescales of our simulations. We compressed these systems to $\phi = 0.62$ before acquiring statistics. In the case of $\gamma$-brass, motif statistics were simply collected for the last 40 million MC sweeps of the self-assembling trajectory, throughout which the crystal was fully formed.

### 4.11.5 Doping simulations

We performed doping simulations by artificially introducing select pairwise motifs into our systems and monitoring consequent assembly or non-assembly. We used isochoric Monte Carlo sampling and treated pairwise motifs as rigid bodies. Simulations were composed of 4,096 particles and run for about 100 million MC sweeps or until the system self-assembled. Overlap checks treated each rigid body as a union of convex polyhedra, and thus trial moves of pairwise motifs were rejected if either member of the pair overlapped with any other particle or pair. We employed a compression and equilibration scheme similar to that used in the hard particle MC simulations described previously, with a few differences to accommodate the larger size and aspect ratio of the dimer dopants: we thermalized the system prior to compression for 1 million MC sweeps rather than 10,000 MC sweeps, and switched rotation move size during compression to its smaller equilibration value if compression was proceeding

slowly.

### 4.11.6 Alchemical Monte Carlo simulations

For alchemical Monte Carlo sampling in the 323 family, we initialized and compressed systems of 1,000 particles to desired volume fractions in an identical manner to that described earlier for traditional isochoric MC sampling. We then equilibrated each system for 10 million MC sweeps at constant volume and constant particle shape. We finally ran Alch-MC simulations of each system for 20-30 million MC sweeps. Alchemical shape moves were attempted with a 25% probability after every MC sweep. In simulations in which both $\alpha_a$ and $\alpha_c$ were sampled, each truncation parameter had a 50% probability of being sampled during a shape move.

For alchemical Monte Carlo sampling in the 423 family, we equilibrated 1,000 particle systems for 10 million MC sweeps at constant volume and particle shape, then allowed particle shape to fluctuate for 29.7 - 40 million MC sweeps. Due to the increased computational time required for particle-particle overlap checks after every alchemical shape move attempt in these systems, we attempted shape moves with a 25% probability after every 10 MC sweeps for all vertex and vertex+edge truncation sampling simulations. During the edge truncation sampling simulations, we attempted shape moves with a 25% probability after every 10 MC sweeps for 26.2 - 28.5 million MC sweeps, and attempted shape moves with a 25% probability after every MC sweep for the remainder of the time.

# CHAPTER V

# Alchemical tuning of glass-forming ability

Consideration of the extended alchemical space in Chapter IV also allows us to explore relationships between seemingly disparate glass-forming systems at different locations in that space. In this chapter, we examine the glass-forming behavior of several systems in the 323 shape family in more depth. We find that the fragility of our glass-formers is a consequence of particle shape and consequent local structure formation, and controlled by location in shape space. We thus demonstrate that the engineering of fragility via slight changes to particle shape is possible.

Richert and Angell [205] were the first to consider that fragility might be a consequence of changes to local structure on approach to the glass transition, and variation in fragility due to changes in local structure has been previously been explored by means of tuning polydispersity [157, 160, 175, 206], isotropic pairwise potential shape [149, 207, 208], local bond-orientational ordering [173], and tetrahedrality [175, 189]. Here, we show that fragility in our hard particle systems is indeed a consequence of local structure formation, mediated by location of the particle in shape space. We find that systems are stronger as constituent particle shapes become increasingly tetrahedral, with smaller amounts of edge and vertex truncation. This corresponds to an increased preference in the system for aligned pairwise configurations characteristic of the dodecagonal quasicrystal and explored thoroughly in Chapter IV. A

periodic crystal consisting of all particles forming aligned pairwise motifs with each of their tetrahedrally coordinated neighbors is impossible due to the frustration inherent in perfect polytetrahedral ordering [209]; thus, the aligned motif is indicative of a locally preferred structure that globally frustrates against periodic ordering, but may give rise to quasiperiodic ordering when higher-order rearrangements of groups of face-to-face aligned particles occur [138]. We find that, in agreement with results [157, 160, 173] supporting a crystallization/frustration competition theory [35], systems become stronger as frustration against periodic ordering increases. Our alchemical lens puts this idea into a concrete, geographical context: systems grow stronger as they move closer to the tetrahedron in shape space.

## 5.1 Dynamical behavior and relaxation time

To examine glass-forming ability across the 323 shape landscape, we investigated dynamical behavior and measured relaxation times in four sample systems in this alchemical space. We employed Monte Carlo simulation techniques identical to those explained in detail in Section 4.11.1, and determined relaxation time by the average of all values $\{t\}$ for which $|\operatorname{Re} F_s(k,t) - \operatorname{Re} F_s(k,0)/e| < \Delta$, where $\operatorname{Re} F_s(k,t)$ is the real part of the self-intermediate scattering function and $\Delta$ is a tolerance chosen from the set $[0.01, 0.05, 0.1]$. We chose the $\Delta$ value that gave a relaxation time $\tau_\alpha$ that produced the best fit of $\operatorname{Re} F_s(k,t)$ to a Kohlrausch-Williams-Watts (KWW) [210, 211] stretched exponential functional form, $B\exp[-(t/\tau_\alpha)^\beta]$, at all densities. We varied $B$ and $\beta$ as fitting parameters. We fit the final fraction $f$ of $\operatorname{Re} F_s(k,t)$ at all densities, and chose $f$ from the set $[0.99, 0.95, 0.9, 0.8, 0.7]$ such that it produced the best fit. We only considered data for which $\operatorname{Re} F_s(k,t) > 0.01$ to avoid unnecessary fitting to long tails at zero.

Fig. 5.1 shows order parameters $\langle \Delta r^2(t) \rangle$, $F_s(k,t)$, $\alpha(t)$, and $\chi_4^{SS}(t)$ that characterize the glass-forming nature of the two additional systems investigated here that

were not explored in Chapter IV. These order parameters are detailed in depth in Section 4.3. For each system, $F_s(k,t)$ was calculated at the first peak of the static structure factor. Static structure factors of all systems are shown in Fig. 5.2 and were calculated for the first frame of each trajectory. Systems at $(\alpha_a, \alpha_c) = (0, 0.5)$, $(0, 0.6)$, and $(0, 0.7)$ display a so-called "pre-peak," or "first sharp diffraction peak," that indicates intermediate-range ordering commonly seen in network glass-formers [212–214].

Fig. 5.3 shows the self-part of the intermediate scattering function $F_s(k,t)$ rescaled by relaxation time for all systems, as well as the best KWW fit. We observe that the systems each obey a so-called "time-temperature superposition" [215] during late $\alpha$-relaxation, indicated by the curves collapsing onto each other.

## 5.2 Fragility across the shape landscape

Fig. 5.4A shows relaxation time $\tau_\alpha$ at varying densities for four systems in the 323 shape family, each with a different particle shape. Relaxation time at each state point was determined by the average of all values $\{t\}$ for which $|\operatorname{Re} F_s(k,t) - \operatorname{Re} F_s(k,0)/e| < \Delta$, as described in Section 5.1, and error bars indicate standard deviations of the mean. Error bars are smaller than the marker size in almost all cases. Note that data points in Fig. 5.4A are missing for system c ($\phi = 0.6$) and system d ($\phi = 0.56$); at these state points, crystallization into the dodecagonal quasicrystal was observed at long simulation times. We did not experiment with faster compression protocols to avoid this crystallization via deeper supercooling, and instead chose to omit these data points from our plot.

We fit our data with a modified Vogel-Fulcher-Tammann (VFT) function [215]:

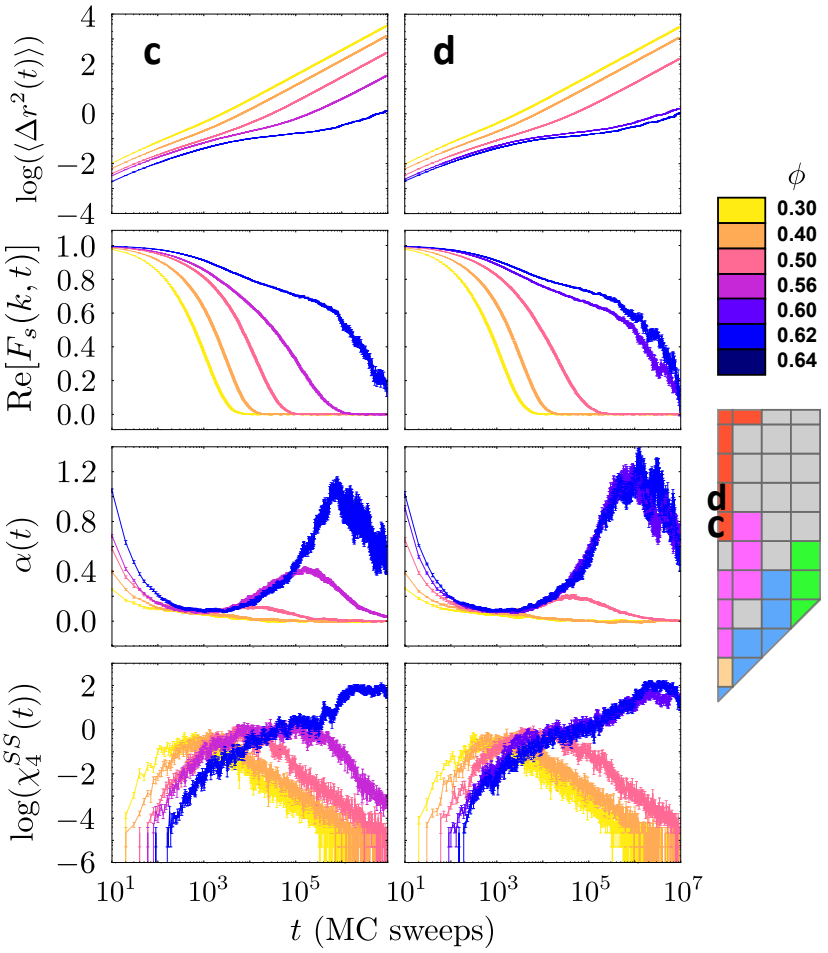


Figure 5.1: The mean-squared displacement $\langle \Delta r^2(t) \rangle$, the real part of the self-intermediate scattering function $F_s(k,t)$, the non-Gaussian parameter $\alpha(t)$, and the four-point susceptibility $\chi_4^{SS}(t)$, measured at a variety of densities for the indicated state points in our shape space. Signatures in all four order parameters indicate that these systems are glass-formers. The increase in $\alpha(t)$ as $t$ goes to zero is due to the discrete nature of our Monte Carlo sampling; see Appendix C for more detail.

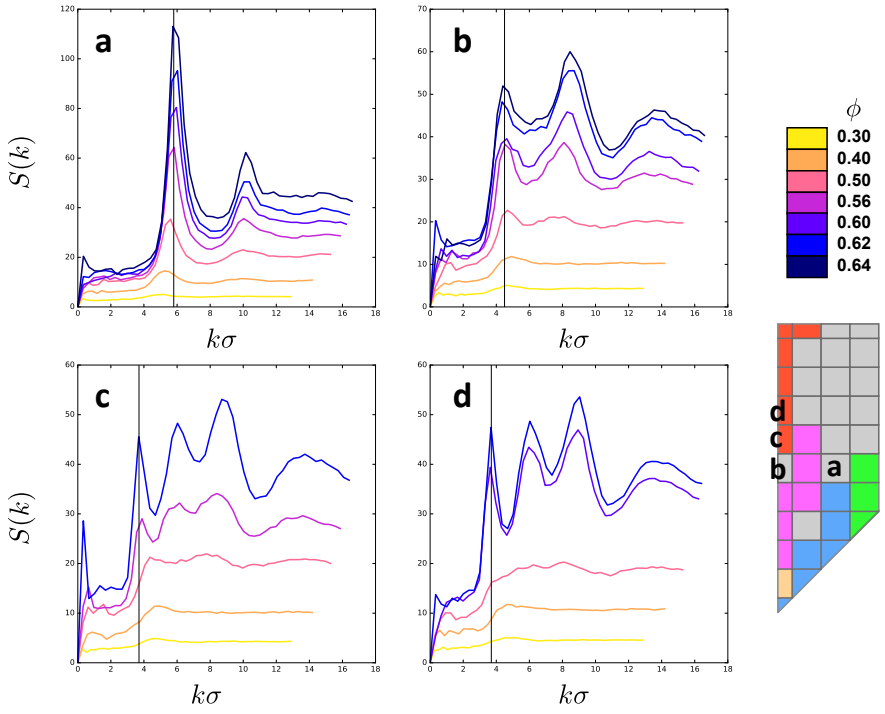


Figure 5.2: Static structure factors for all systems, identified by letters in the shape space. Static structure factors are given as functions of $k\sigma$, where $\sigma$ is a length scale that characterizes the particle size of each system: $\sigma^3 = v_p$, where $v_p$ is the particle volume. Vertical lines through each plot indicate the position of the first peak, used for calculation of the self-intermediate scattering function. These positions are $k\sigma = 5.8, 4.5, 3.7, 3.7$ for $(\alpha_a, \alpha_c) = (0.2, 0.5)$, $(0, 0.5)$, $(0, 0.6)$, and $(0, 0.7)$, respectively.

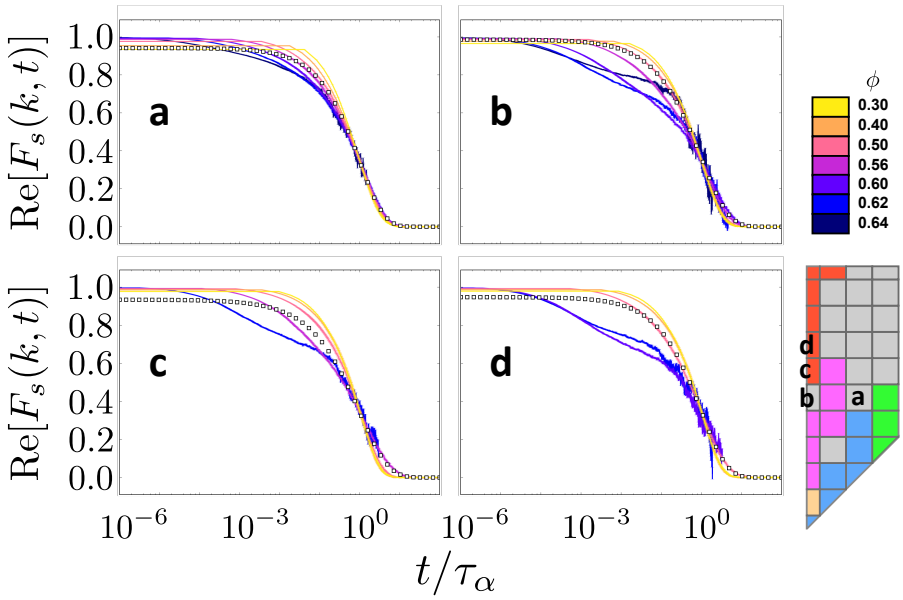


Figure 5.3: The real part of the self-intermediate scattering function as a function of rescaled time, for indicated state points. The optimal KWW fit is shown in white squares.

$$\tau_\alpha(\phi) = \tau_\infty \exp\left[\frac{A}{(\phi_0 - \phi)^\delta}\right] \tag{5.1}$$

We used $\delta = 2$ because this form has been found to accurately model relaxation times in other hard particle systems at high density [179, 216, 217]. Lines in Fig. 5.4A are VFT fits to our relaxation data. For some systems, relaxation times at high $\phi$ fall off the trend lines established by the VFT fits, in agreement with relaxation times observed in systems of hard tetrahedra in Ref. [179]. Coauthors in that paper hypothesized that this was due to higher order local structure formation in systems of tetrahedra at high density. We do not speculate on the cause of this peculiar behavior here, but merely note that as a result of this behavior, we did not include some values of $\tau_\alpha$ at high $\phi$ when fitting the VFT functional form to our data. Were we to include those values, the accuracy of the VFT fits would be greatly reduced.

Solid lines in the figure pass through the data points that were actually fit, and dotted lines indicate continuations of the fit function. Fig. 5.4A shows that VFT fits are able to qualitatively capture the relaxation behavior of all systems, although the fits begin to deviate from the data for small $\phi$.

Fig. 5.4B shows scaled relaxation time as a function of scaled density for our sample systems. $\phi$ is scaled by the factor $\phi_C$, defined for each system according to $\tau_\alpha(\phi_C) = 2e6$ MC sweeps. To determine $\phi_C$, $\tau_\alpha$ was extrapolated for each curve according to its fit by the VFT functional form. $\tau_\alpha$ is also scaled in the figure by the quantity $\kappa$, defined for each system by $\kappa^{-1} = \tau_\alpha(\phi = 0.3)$. This scaling collapses the data for small $\phi$. We performed this scaling to account for the different length scales (and thus different values of $k$ used to calculate the self-intermediate scattering function and consequent relaxation time) associated with each particle shape. Similar scaling has been performed elsewhere [179, 216, 218].

Curves for each particle shape show different slopes on approach to the glass transition, and thus different fragilities, although the trend is not very clear from the data in the main portion of Fig. 5.4B alone. To make this clearer, we quantified our observations by calculating $m \equiv \partial \log \tau_\alpha / \partial(\phi/\phi_C)$, shown in the inset of Fig. 5.4B. The glass transition limit of this quantity is known as the "$m$ fragility"[219] or "steepness index"[220]; this parameter has the advantage of indicating fragility while not relying on any fit to a theoretical model. Stronger glass-formers exhibit a less dramatic increase in $m$ with increasing density, and the inset of Fig. 5.4B clearly shows this trend for particle shapes that are more tetrahedral.

Fig. 5.4C shows the fraction of aligned pairwise motifs in each system as a function of density scaled by $\phi_C$. Stronger glass-formers are increasingly dominated by particle pairs in the aligned configuration at all densities. Regardless of fragility, the fraction of particles participating in the aligned motif increases as relaxation time increases, although less drastically for the more fragile systems due to the presence of other

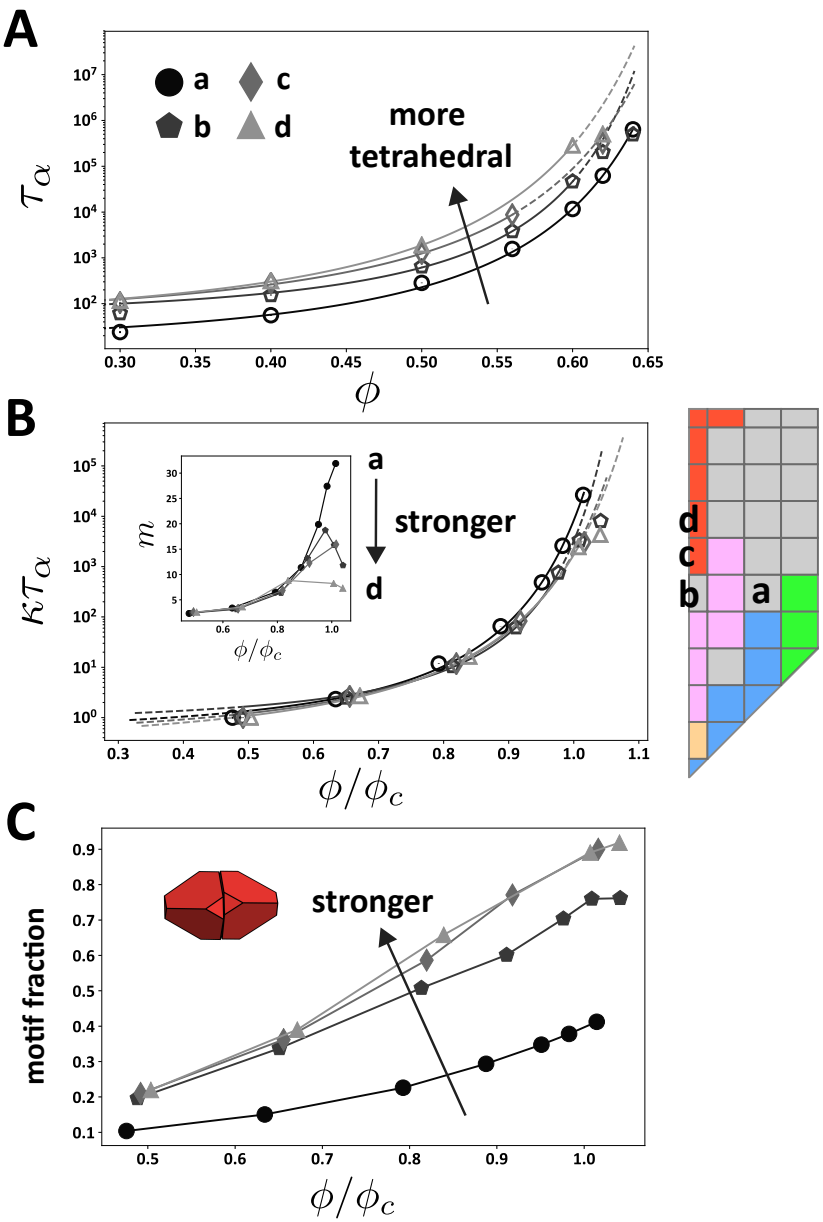


Figure 5.4: Glass-forming systems exhibit a range of fragilities, with systems becoming "stronger" as particle shapes move closer to the upper left corner of shape space, corresponding to the non-truncated tetrahedron. (A) An Angell plot of relaxation time as a function of density. Relaxation time is in units of 10 MC sweeps. Lines through the data points are VFT fits to relaxation time. (B) A scaled Angell plot, where density is scaled by $\phi_C$ and relaxation time is scaled by $\kappa$, both defined in the main text. Inset are the slopes of the logs of relaxation time as a function of scaled density. Systems of more tetrahedral particle shapes tend to be stronger. (C) Fractions of particles in the aligned pairwise motif as a function of scaled density. An example of this motif for the particle shape $(\alpha_a, \alpha_c) = (0, 0.5)$ is inset.

Table 5.1: Parameters related to VFT fits of relaxation time in our systems. $\tau_\infty$ is in units of 10 MC sweeps.

| $\alpha_a$ | $\alpha_c$ | $\phi_0$ | $\tau_\infty$ | $A$ | $\phi_C$ |
|---|---|---|---|---|---|
| 0.2 | 0.5 | 0.800 | 9.760 | 0.284 | 0.631 |
| 0.0 | 0.5 | 0.762 | 42.460 | 0.183 | 0.615 |
| 0.0 | 0.6 | 0.812 | 32.220 | 0.356 | 0.610 |
| 0.0 | 0.7 | 0.811 | 26.056 | 0.416 | 0.596 |

pairwise motifs. Aligned motif fractions were calculated in frames separated by 1e6 MC sweeps. Motif fractions were collected over groups of 10 frames each, and the mean values are plotted in Fig. 5.4C with error bars associated with the standard deviation of the mean. Error bars are smaller than marker sizes in all cases.

For completeness, we tabulate parameters associated with VFT fits to our data in Table 5.1. However, we note that due to the aforementioned discrepancies in $\tau_\alpha$ at high $\phi$ and our consequent ad hoc fitting procedure, these values may not be especially informative.

## 5.3 Conclusions

In this chapter, we used the concept of the alchemical ensemble to show that systems in shape space have glass-forming properties that are related to and dependent upon their position in this space. We found a range of fragilities over a small range of particle shapes related to the regular tetrahedron. Stronger glass-formers, with relaxation times that are closer to exponential functions of density, result when particle shape is less truncated and thus more tetrahedral. By tuning particle shape (and therefore position in shape space), we showed that we consequently tune fragility, which may be useful for applications related to phase-change memory technology [221]. This chapter is adapted from Ref. [222], a manuscript authored by E.G. Teich, G. van Anders, and S.C. Glotzer that is currently in preparation.

# CHAPTER VI

# Structural detection in other contexts

Over the course of my dissertation, the software I developed to analyze particle neighborhoods in real space (detailed in 2.2.2.1) found uses in a variety of applications. Some of these applications were published, and some are yet to be published; some were spearheaded by me, and some I had little to do with besides providing software and scripts. In this chapter I briefly outline a handful of these applications.

Analysis of particle neighborhoods in real space lends itself to two broad classes of use. The first is rather agnostic in its approach, and relies on comparisons among particle neighborhoods as its main means of gathering information. Particle neighborhoods, or environments, are determined throughout the system and compared with each other, either in a local or global manner. If the comparison is global, all particle environments are compared with all others; if the comparison is local, particle environments are only compared with other nearby environments. The latter case is especially useful for crystal grain detection, as crystal grains can be defined through this method as clusters of particles that are spatially localized with similar environments. Users may specify how the particle environments are calculated by requiring that the environments of each particle consist of either a certain number of nearest neighbors or all neighbors that lie within some cut-off distance of the particle center. Users may wish instead to be maximally agnostic by using automatically calculated

quantities associated with an ensemble-averaged first neighbor shell.

The second use-class of my environment-matching software is more directed, and involves the search for user-specified structural motifs within simulations. In this case, users may choose to compare the environment of every particle in the system against some environment of interest that they provide. This is useful in analyses in which users are especially interested in tracking specific structural motifs over the course of a simulation. For example, it may be informative to track structural motifs that are prevalent in end-game crystalline structures during the crystallization process itself. Do the structures exist in the fluid? How do they influence the crystallization process? Indeed, we already saw the usefulness of this consideration on a pairwise level when examining the glass-forming behavior of systems of hard polyhedra; the aforementioned structure-tracking is simply an extension to motifs consisting of multiple particles.

## 6.1 Crystal grain detection

Environment matching in real space is very useful for agnostically detecting crystal grains in twinned or polycrystalline systems. Fig. 6.1 shows two examples of crystal grain detection in simulations; particles are colored according to grain.

Panel A illustrates twinning detection by this method in three dimensions, in an *fcc* crystal of hard truncated octahedra. This data was provided by my labmate Chrisy Xiyu Du. Two grains exist in the system, colored blue and purple respectively, and are separated by two grain boundaries (colored red and green) due to periodic boundary conditions. Particles are colored black if their environments do not match the environments of their neighbors, or if they are members of crystalline clusters with sizes below some cut-off. Bond-order diagrams to the right of the simulation image show the local neighborhood (projected onto a unit sphere) of (top) all particles in the simulation box, (middle) only particles in the blue grain, and (bottom) only

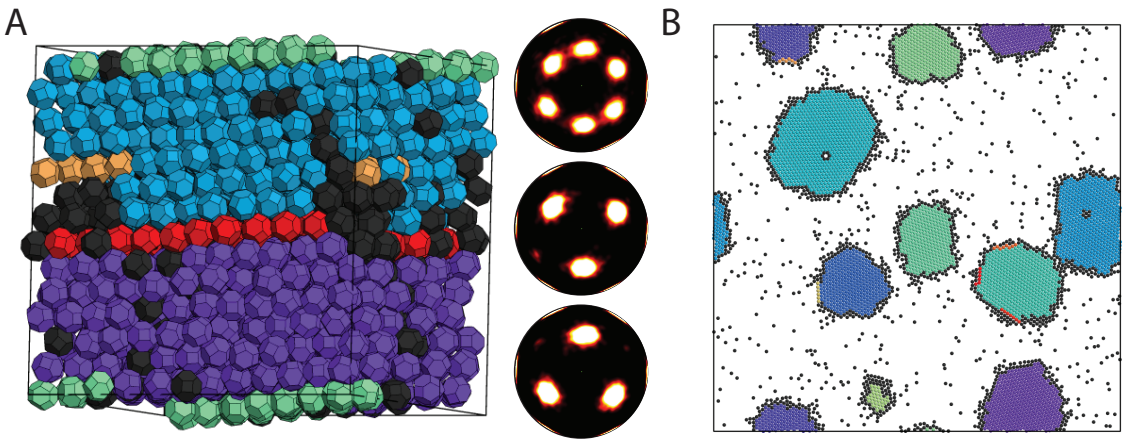


Figure 6.1: Crystal grain detection via environment matching in (A) three dimensions and (B) two dimensions. Particles are colored by cluster; black particles are not members of any crystalline cluster or belong to a crystalline cluster with a size below some cut-off.

particles in the purple grain. The bond-order diagrams are oriented along the three-fold rotational axis of symmetry of the *fcc* structure, and show that each grain has a three-fold axis that is rotated 60° with respect to the other. The superposition of these makes up the cumulative bond-order diagram.

Panel B shows crystal grain detection in two dimensions, in a system of active hexagons (rendered here as circles) that cluster into groups during a simulation. This data was provided by my labmate Shannon Moran. This example is somewhat trivial, as these groups of particles could be found via other means of spatial clustering, but it additionally shows that crystal defects and boundaries can be detected via environment matching in two dimensions. As before, particles are colored by cluster, and are colored black if they are not members of any crystalline cluster or belong to a crystalline cluster with a size below some cut-off.

Fig. 6.2 shows crystal grain detection in a more complicated case, when truncated octahedra self-assemble into a high-pressure lithium-like (Li) structure with eight unique particle environments in one unit cell. In this case, one can define the environment of a particle as the set of vectors pointing to its 11 nearest neighbors,

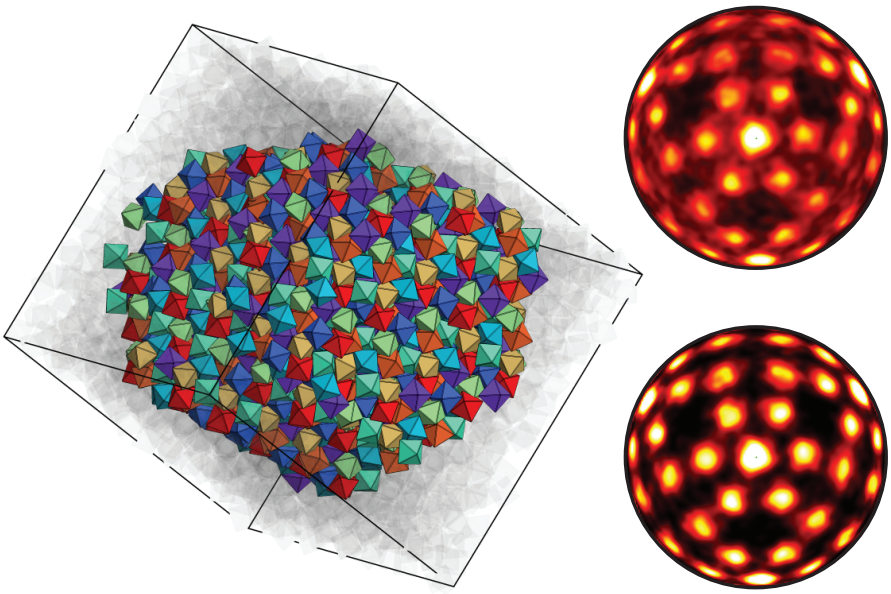

Figure 6.2: High-pressure lithium crystal grain detection in a system of hard truncated octahedra. Particles are colored by cluster; transparent black particles are not members of any crystalline cluster or belong to a crystalline cluster with a size below some cut-off.

and then search for similarity with the environments of other particles that are close by. Care must be taken to make sure that the field over which the software searches for similar neighbors is wide enough, since the unit cell is bigger and thus particles with similar environments are further away from each other. The Li grain is characterized by eight colors, corresponding to the eight unique particle environments in the high-pressure lithium structure. Other particles that are not members of any crystalline cluster or belong to a crystalline cluster with a size below some cut-off are colored black and shown transparently. Bond order diagrams to the right of the simulation image show the local environment of (top) all particles and (bottom) particles identified as the high-pressure lithium grain; the grain shows a cleaner crystalline environment.

Environment matching may also be used to track the fraction of particles found to be crystalline over the course of a simulation trajectory, and in that way to monitor

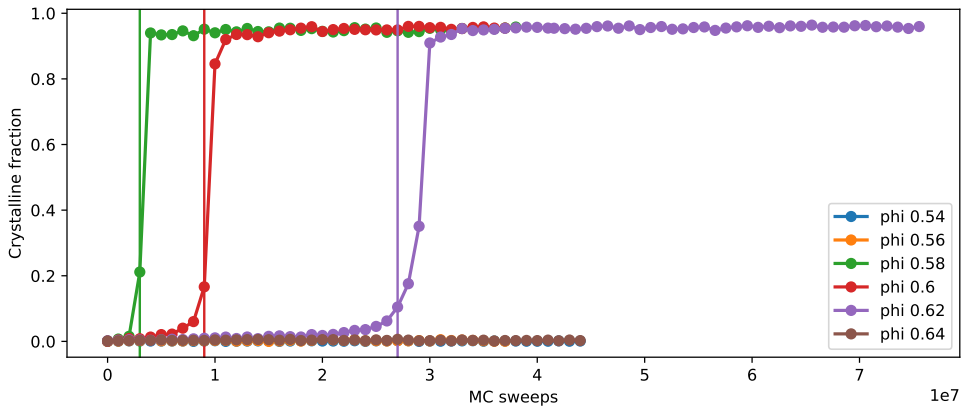


Figure 6.3: Crystallization in a system of hard truncated octahedra. Crystalline fraction is plotted as a function of time; crystallization is marked by a significant jump in crystalline fraction. Nucleation incubation times, defined in the main text, are shown as vertical lines.

the crystallization process. Fig. 6.3 shows the fraction of crystalline particles in simulations of truncated octahedra at multiple densities. These systems self-assemble into the *bcc* phase; we thus cluster particles according to common environment, searching over the 14 nearest neighbors of every particle, and label a particle as "crystalline" if it belongs to a cluster of size $s > 1$. Crystallization in these systems is marked by a nearly instantaneous (in the time resolution of our trajectory writing) jump in the fraction of crystalline particles measured in the system. We can also quantify crystallization through observables like the nucleation incubation time [178], defined in these simulations as the first frame after which approximately all measured crystalline particle fractions are greater than 0.1. Nucleation incubation times are drawn as vertical lines in the figure.

The final example of this use case augments environment-matching with information regarding particle orientations; although this is a somewhat specialized application, I include it here to illustrate the power of combining different methods of local structural detection. Fig. 6.4 shows the fraction of particles detected as bcc-like and as high-pressure Li-like as a function of time in a single trajectory of hard truncated

octahedra at packing fraction $\phi = 0.61$. In this trajectory, the high-pressure Li structure first forms, before transforming into the *bcc* structure. Plots of the crystalline fraction of each phase show this phenomenon: first the fraction of Li-like particles grows, then plummets to zero as the fraction of *bcc*-like particles grows and eventually saturates. This result supports the claim in an earlier chapter of this thesis (and our accompanying paper [142]) that the high-pressure Li phase is metastable to *bcc* at this state point.

*Bcc*-like particles are defined as those whose environment of 14 nearest neighbors matches the environments of surrounding particles within some threshold, with an additional restriction based on particle orientations. That restriction is as follows: when a crystalline cluster of particles is identified by the aforementioned environment matching scheme, the average minimal misorientation angle of all particles in that cluster with respect to their nearest neighbors must be less than or equal to 31.4°. Only then is the cluster classified as *bcc*-like. This is because, in *bcc* assemblies of octahedra, particles are oriented in the same direction, and thus have misorientations of $\sim 0°$ with respect to their nearest neighbors. The maximal misorientation of two objects of octahedral symmetry is $\sim 62.8°$; thus we use 31.4° as our cut-off. Li-like particles are defined as those whose environment of 11 nearest neighbors matches the environments of surrounding particles within some threshold, with essentially the opposite restriction based on particle orientations. When a crystalline cluster of particles is identified by this environment matching scheme, the average minimal misorientation angle of all particles in that cluster with respect to their nearest neighbors must be greater than 31.4°. Only then is the cluster classified as Li-like. In high-pressure lithium assemblies of octahedra, particles are typically (to within thermal fluctuations) oriented perfectly face-to-face with their nearest neighbors. This corresponds to a misorientation of 60°.

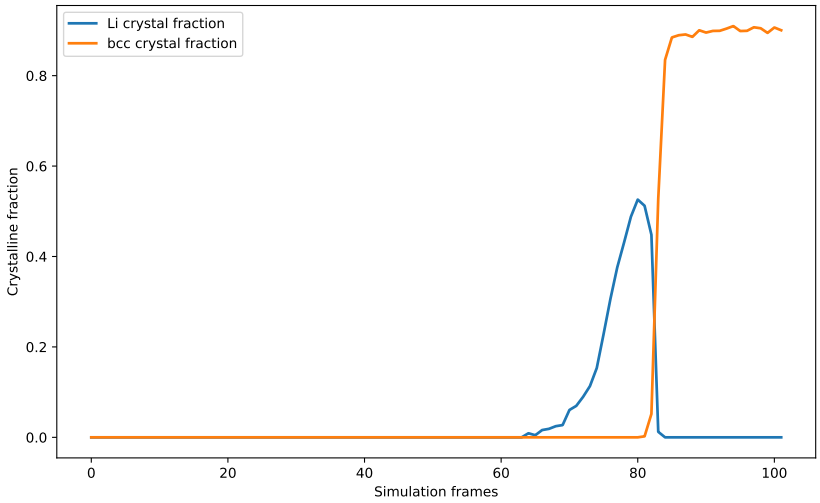


Figure 6.4: The growth of high-pressure lithium and its transformation to the *bcc* structure during a single simulation trajectory of hard truncated octahedra.

## 6.2 Motif detection

Detection of specific structural motifs over the course of a simulation via environment matching is an informative means of tracking the crystallization process, especially when said process is more complicated than homogeneous nucleation and growth. As an example, I consider the two-step nucleation and growth of a complicated clathrate-like crystal phase in systems of hard truncated tetrahedra of very specific vertex and edge truncations, shown in Fig. 6.5. My collaborator and labmate Sangmin Lee discovered this phase, and we hypothesize that its formation mechanism is two-step in nature; first a phase transition from a low-density fluid to a high-density fluid occurs in this system, and only after that process does the additional phase transition from the high-density fluid to the clathrate-like crystal occur. Julia Dshemuchadse and Michael Engel have determined that the clathrate-like phase possesses face-centered cubic symmetry, with space group $Fd\bar{3}$ and no more than 432 particles in the cubic unit cell. Fig. 6.5A shows the unit cell of 432 particles. The

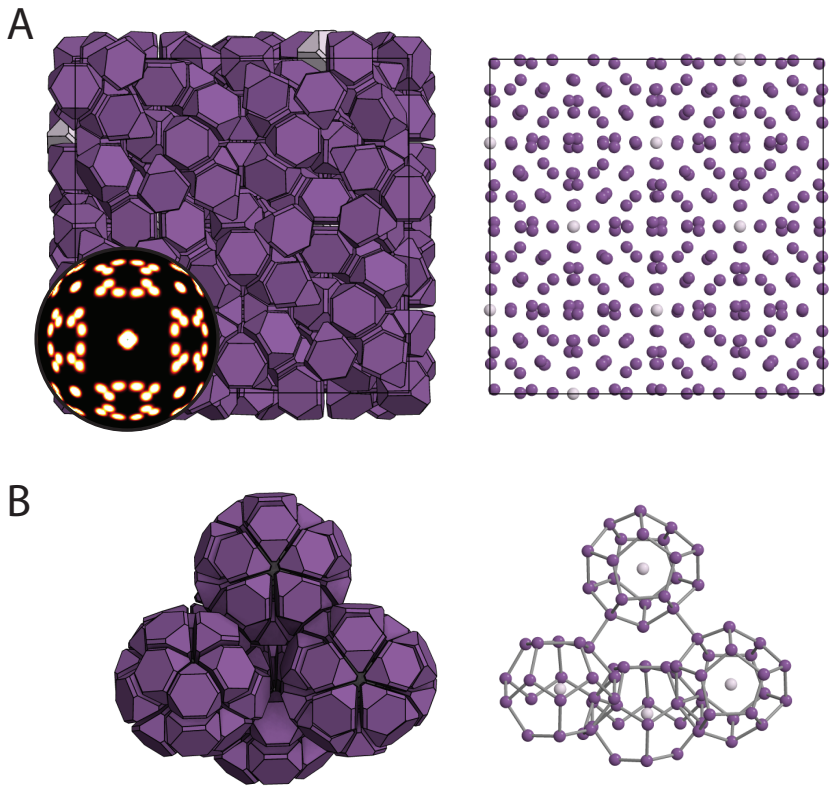


Figure 6.5: The clathrate-like phase that assembles in systems of specifically-truncated hard tetrahedra. (A) The 432-particle unit cell of this structure. (B) An example of how dodecahedral cages of twenty particles surrounding a single particle are linked throughout this structure.

image to the left also contains the bond-order diagram of the structure, and the image to the right shows particle centers of mass, more clearly depicting the symmetry of the cell. We term the structure clathrate-like because it is made up of dodecahedral cages of twenty truncated tetrahedra surrounding a central particle. These are arranged periodically in a complicated manner, with "glue" particles linking them in specific ways. Particles are colored gray if they are at the centers of these dodecahedral cages, and purple otherwise. Fig. 6.5B shows an example of how the dodecahedral cages are linked throughout this structure: it consists of four dodecahedral cages, arranged in a tetrahedral fashion. The particle centers are shown to the right, with bonds between them to guide the eye. Links can be clearly seen between the dodecahedral cages.

Dodecahedral cages are important motifs in this assembled clathrate-like structure. It is useful, then, to track dodecahedral cages during the crystallization process, from the high density fluid phase to the crystal phase. This analysis could answer questions such as: Do the dodecahedra form independently of each other, and then link up somehow, or does one dodecahedron form and then act as a seed for the growth of other dodecahedra? How does the quality of the dodecahedral cages change during crystallization? More generally, how does nucleation propagate in this complicated two-step process? Fig. 6.6 shows a first step towards answering these questions using environment matching. It consists of three simulation snapshots during the crystallization process from the high density fluid to the clathrate-like phase. Not all particles in the simulation box are shown; rather, I show only those particles with environments that are suitably dodecahedron-like. Particles are redder in hue if their environments are more similar to dodecahedra. The clear crystalline ordering of dodecahedral cages can be seen in this figure. Dodecahedral cages exist throughout the system in the snapshot to the left, before crystallization, although they are less red in hue and thus lower quality. The central snapshot shows a seed of high-quality dodecahedral cages, arranged in a manner consistent with the final crystalline structure, that ultimately gives rise to the final crystal. Bonds are drawn between particles to guide the eye, and the seed is outlined with a circle. The periodic nature of the final structure is clearly demonstrated by the right-most snapshot: the dodecahedral cages are arranged in a cubic manner, consistently with the arrangement of the crystal seed in the high-density fluid. More quantitative analysis must be performed to fully elucidate the nature of this complex crystal growth, but Fig. 6.6 indicates that motif matching to find dodecahedral environments during the crystallization process is a fruitful analytical avenue.

To generate these images, I tested particle environments (consisting of vectors pointing to 20 nearest neighbors) for similarity with an ideal dodecahedron, suitably

scaled to match the pertinent length scales of the simulation. To save time, I pre-filtered which particle environments were tested for similarity: I only tested those with an appropriate number of nearest neighbors in a shell of appropriate distance, such that they were good candidates for dodecahedral-like characteristics. Specifically, I only tested particle environments that contained between 17 and 20 nearest neighbors in a shell characterized by $1.2 < r < 1.8$, where $r$ is radial distance from the particle center. A typical dodecahedral shell in the final structure is characterized by a radial distance of $R \sim 1.45$ from the central particle to any of its twenty nearest neighbors. I then minimized the root-mean-squared displacement of these pre-filtered environments with respect to a (scaled) ideal dodecahedron, using environment matching, and calculated the number of vectors in each particle environment that were matched to the vertices of an ideal dodecahedron. Only particles with a number of matching environment vectors greater than or equal to 11 are shown, and they are colored by the number of matching environment vectors. The more red these particles are, the more environment vectors they possess that match to the vertices of an ideal dodecahedron.

## 6.3 Uses in publications and pre-prints

My environment matching software was used to detect crystalline domains in polycrystalline assemblies of binary mixtures of tetrahedra and octahedra [223] and diamond-like assemblies of truncated tetrahedra [43].

It was also used to monitor crystallization in our forthcoming paper on local structure in hard particle glass-formers, as detailed in Chapter IV.

In another forthcoming paper [224], we use this software as a way of detecting unit cells in systems of densely packed anisotropic particles.

A final forthcoming paper [225] uses environment matching to track physically relevant structural motifs during the complex two-step nucleation and growth of trun-

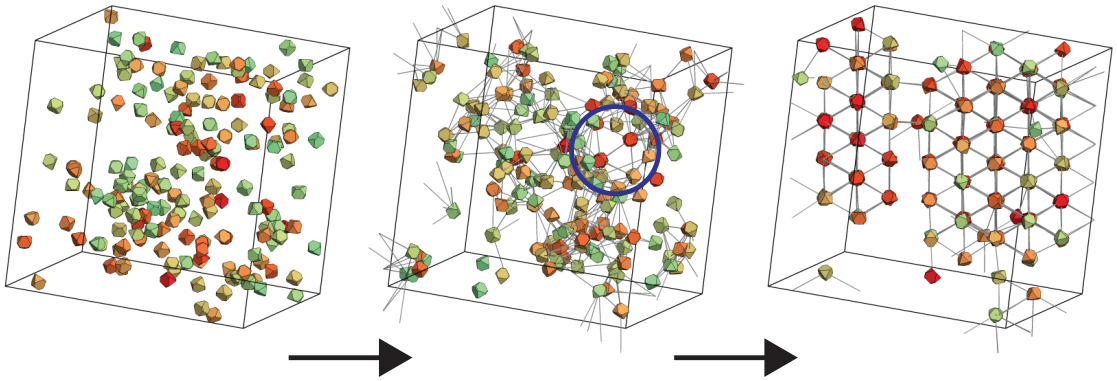

Figure 6.6: The evolution of particles with dodecahedron-like environments during crystallization into a complex clathrate-like phase. Only particles with suitably dodecahedron-like environments are shown, and particles that are redder in hue possess more dodecahedron-like environments. Three snapshots are shown from the crystallizing trajectory, and are arranged chronologically from left to right. During crystallization, dodecahedral cages are shown to arrange themselves periodically; the central image shows the seed, outlined by a circle, that gives rise to the final periodic structure.

cated tetrahedra into a clathrate-like phase, as detailed earlier.

This software is also being used to detect local environments in complex crystals for comparison against various reference motifs [187], to track local motif formation during the growth of the hard tetrahedron dodecagonal quasicrystal, and to understand the metastability of high-pressure lithium in various hard particle systems.

# CHAPTER VII

# Conclusion and outlook

This dissertation explored the role of local structure in crystallization and its failure in systems controlled solely by entropy maximization. Structure in these systems is often not easy to identify or treat theoretically, and its role in thermodynamic phase behavior has yet to be fully elucidated, due to analytical intractability and the emergent nature of entropy-driven structure formation. I studied local structure in hard particle systems through two broad computational investigations.

In the first investigation, detailed in Chapter III, I explored dense clusters of hard polyhedral particles formed through spherical confinement. In addition to numerous experimental and technological motivations unrelated to the fundamental physics of self-assembly, this work was driven by the question of how to identify multi-particle preferred motifs during the crystallization of hard particles. We hypothesized that spherical confinement may act as a zeroth-order approximation of the local environment during unconfined self-assembly, and sought to identify candidate locally dense motifs that might be important in crystallization via this confinement mechanism. We found that spherical confinement for our cluster sizes tends to actually suppress packing effects due to particle shape, causing polyhedral particles to mimic the behavior of spheres and form tightly-packed concentric layers. We also explored other interesting, unanticipated signatures in our data set, including especially dense clusters at

certain shape-dependent "magic numbers" of constituent particles, the violation of a modified Ulam's conjecture in spherical confinement, and a connection to the mathematical concept of optimal spherical codes. We also found a possible connection to preferred local structure during crystallization, by identifying the densest cluster of tetrahedra in spherical confinement as an important motif in the self-assembled dodecagonal quasicrystal of hard tetrahedra.

In a second investigation detailed in Chapters IV and V, I explored the effect of shape perturbation on local structure formation and consequent crystallization or crystallization failure. This work was motivated by the question of why crystallization fails in some hard particle systems and succeeds in other very similar systems, and how local structure formation plays a role in that phenomenon. We were additionally inspired by the glass community's ongoing endeavor to uncover the role of structure in dynamical arrest. We studied local structure and dynamical behavior across so-called "shape landscapes," or families of systems of particles of continuously interrelated shape. We found that crystallization failure in these systems can be attributed to competition in local structural motifs, each of which is prevalent in ordered phases assembled by particles of closely related shape. We showed evidence that this structural "identity crisis" in the dense fluid indeed gives rise to vitrification by artificially manipulating the local structure in various dense fluids and consequently enhancing or suppressing crystallization. We also showed that disordered systems tend to escape regions of structural competition and subsequently crystallize when allowed to explore shape space through extended Monte Carlo sampling techniques. In Chapter V, we showed that fragility, a measure of glass-forming ability extensively used in the glass community, can be tuned through slight changes to particle shape and consequent changes to the local structural makeup of the system.

I concluded my dissertation with a brief discussion of structural detection mechanisms and an implementation I developed that has found use in a range of applications.

## 7.1 Outlook

My work opened up many new avenues for investigation, and it will be a privilege to see it continued by newer generations of graduate students. My study on confinement could be enormously expanded through the consideration of different confinement mechanisms and confined particle shapes. Mesh confinement, packing about a point, different confinement geometries, or the introduction of surface tension might give rise to cluster structures that are more relevant in hard particle self-assembly. Confinement of flexible or semi-flexible polymers may be relevant for applications related to the containment of genomic material in cells and capsids [59, 226, 227], and confinement of ellipsoids may be helpful for studying the effects of cell nucleus confinement on the behavior of ellipsoidal nucleosomes and higher-order chromosome territories [58, 228, 229]. Interpolations in particle shape from highly faceted particles to spheres may be additionally informative: at what level of rounding do packing effects due to particle shape disappear in spherical confinement? Can we design particles balanced on an edge such that slight changes to particle shape trigger completely different cluster geometries? Laura Rossi and collaborators have the ability to build rounded colloidal cubes and to control the degree of particle rounding [230]; we are currently working with them to study questions of this type on both a computational and experimental front. On another note, one could ask how cluster geometry changes with system size. There must be a cross-over with size from surface-dominated packing behavior to bulk-dominated behavior, and that phenomenon has already been explored in clusters of spheres [73]. It would be interesting to see how particle shape influences this cross-over. We have begun a study of this sort with a former undergraduate in our lab, Larissa Woryk; it would be informative to continue and expand on that. Finally, I am very interested in the role of the densest tetrahedron cluster in the self-assembly of the dodecagonal quasicrystal. Is it an important motif in that crystallization process? When in the process does it appear and how does it prop-

agate during nucleation? Kwanghwi Je, a current graduate student in our group, is pursuing those questions.

My study on structural competition in colloidal glass-formers could be continued in many fascinating directions. It would be very informative to stress-test our hypothesis about local structural competition in other contexts completely divorced from the influence of hard particle shape. Russo, Romano, and Tanaka have already published a very promising work [175] in which they find that structural competition, and therefore surface tension between the dense fluid phase and any possible crystal phase, is responsible for vitrification in a binary hard disk system and a system of particles governed by a modified Stillinger-Weber potential. It would be interesting to extend those ideas to our systems and others. It would also be very interesting to more thoroughly study the relationship between structure and dynamics in our systems. For instance, which motifs are slow and which are fast? How does structure give rise, on a microscopic level, to observed dynamical heterogeneity? Can dynamical signatures be tuned on-the-fly by tuning particle shape? Finally, we found that glass-forming systems consistently crystallize when allowed to explore shape space, and a related study [231] in preparation by Paul M. Dodd in our group also supports the preliminary conclusion that the glass transition may be avoided in an extended ensemble. It would be very interesting to dive more deeply into the implications of this conclusion. Is there a physical relevance to the paths systems take when moving through extended space to form ordered structures? What is that relevance? What is the relationship between complexity and entropy in systems in this extended ensemble? What does this observation tell us about the distinct preference for simplicity that nature generally tends to have? Answering these questions, potentially in the context of information theory, would be illuminating.

I'll close by allowing a beat of Buddhism to creep into this document– I fell in love with these words many years ago, long before I discovered my passion for statistical physics and the study of the dance.

Of what is the body made? It is made of emptiness and rhythm. At the ultimate heart of the body, at the heart of the world, there is no solidity

. . . there is only the dance.

- George Leonard

# APPENDICES

# APPENDIX A

# The potential of mean force and torque

Here we consider the mathematical framework underlying the potential of mean force and torque as developed by van Anders *et al.* [36, 37]. Recall that the potential of mean force and torque (PMFT) $F_{12}\left(\Delta\xi_{12}\right)$, associated with a pairwise configuration $\Delta\xi_{12}$ between any two particles, is implicitly defined as follows:

$$Z \equiv \int d\Delta\xi_{12} e^{-\beta F_{12}(\Delta\xi_{12})} \tag{A.1}$$

$Z$ is the partition function (where we are ignoring overall constants due to integration over momentum terms and normalization by any factors proportional to Planck's constant), and $\beta \equiv 1/k_B T$. $F_{12}\left(\Delta\xi_{12}\right)$ controls the contribution of the state characterized by $\Delta\xi_{12}$ to the partition function; when it is lower, the contribution is greater, implying that the state characterized by $\Delta\xi_{12}$ contributes more microstates to Z.

Van Anders *et al.* explored the physical meaning of $F_{12}\left(\Delta\xi_{12}\right)$ by decomposing it into contributions from (i) the particle pair with configuration $\Delta\xi_{12}$ and (ii) the surrounding sea of particles. They did this by separating the partition function into sums over pair configurations and sea configurations given a fixed pairwise configuration:

$$
\begin{aligned}
Z &= \int d\boldsymbol{r}^N dq^N e^{-\beta U(\boldsymbol{r}^N, q^N)} \\
&= \int d\boldsymbol{r}_1 d\boldsymbol{r}_2 dq_1 dq_2 \int d\boldsymbol{r}^{N-2} dq^{N-2} e^{-\beta U(\boldsymbol{r}^N, q^N)} \\
&= \int d\boldsymbol{r}_1 d\boldsymbol{r}_2 dq_1 dq_2 e^{-\beta u_{12}(\Delta\xi_{12})} \int d\boldsymbol{r}^{N-2} dq^{N-2} e^{-\beta \sum^N_{\substack{i\neq j \\ i,j\neq 1,2}} u_{ij}(\Delta\xi_{ij})}
\end{aligned} \tag{A.2}
$$

Line 3 proceeds from line 2 by taking a pairwise approximation of $U$:

$$
U(\boldsymbol{r}^N, q^N) \equiv \sum_{i\neq j} u_{ij}(\Delta\xi_{ij}) \tag{A.3}
$$

It is most useful to make a change of variables $\{\boldsymbol{r}_1, \boldsymbol{r}_2, q_1, q_2\} \rightarrow \{\boldsymbol{r}_1, q_1, \boldsymbol{r}_{12}, M_{12}\}$, so that we are integrating over the relative configuration $\Delta\xi_{12}$ of particles 1 and 2; $\boldsymbol{r}_{12}$ is the relative displacement between particles 1 and 2, and $M_{12}$ is the relative misorientation between particles 1 and 2. We can make the choice of defining $\boldsymbol{r}_{12}$ and $M_{12}$ in the reference frame of particle 1 so that both quantities are invariant under global rotations and translations. There is a Jacobian associated with this change of variables under integration:

$$
d\boldsymbol{r}_1 d\boldsymbol{r}_2 dq_1 dq_2 = J(\Delta\xi_{12}) d\boldsymbol{r}_1 dq_1 d\boldsymbol{r}_{12} dM_{12} \tag{A.4}
$$

The Jacobian is written schematically as a function of the pairwise configuration $\Delta\xi_{12}$ because the relative displacement and misorientation are the only new quantities we introduced in our change of variables, so $J$ must only depend on $\Delta\xi_{12}$. More precisely,

$$J = \begin{vmatrix} \frac{\partial \boldsymbol{r}_1}{\partial \boldsymbol{r}_1} & \frac{\partial \boldsymbol{r}_1}{\partial \boldsymbol{r}_2} & \frac{\partial \boldsymbol{r}_1}{\partial q_1} & \frac{\partial \boldsymbol{r}_1}{\partial q_2} \\ \frac{\partial q_1}{\partial \boldsymbol{r}_1} & \frac{\partial q_1}{\partial \boldsymbol{r}_2} & \frac{\partial q_1}{\partial q_1} & \frac{\partial q_1}{\partial q_2} \\ \frac{\partial \boldsymbol{r}_{12}}{\partial \boldsymbol{r}_1} & \frac{\partial \boldsymbol{r}_{12}}{\partial \boldsymbol{r}_2} & \frac{\partial \boldsymbol{r}_{12}}{\partial q_1} & \frac{\partial \boldsymbol{r}_{12}}{\partial q_2} \\ \frac{\partial M_{12}}{\partial \boldsymbol{r}_1} & \frac{\partial M_{12}}{\partial \boldsymbol{r}_2} & \frac{\partial M_{12}}{\partial q_1} & \frac{\partial M_{12}}{\partial q_2} \end{vmatrix}$$
$$= \begin{vmatrix} \frac{\partial \boldsymbol{r}_{12}}{\partial \boldsymbol{r}_2} & 0 \\ 0 & \frac{\partial M_{12}}{\partial q_2} \end{vmatrix} \tag{A.5}$$

$\frac{\partial \boldsymbol{r}_{12}}{\partial \boldsymbol{r}_2}$ is shorthand for a $3 \times 3$ matrix whose $ij$-th element is the derivative of the $i$-th component of $\boldsymbol{r}_{12}$ with respect to the $j$-th component of $\boldsymbol{r}_2$. $\frac{\partial M_{12}}{\partial q_2}$ is similarly defined and also a $3 \times 3$ matrix, since any orientation can be defined by three components. The Jacobian is generally not straightforward to compute, so I will not explore it further in any specific sense, but will rather consider its associated physical intuition. We can write:

$$Z = \int d\Delta\xi_{12} J(\Delta\xi_{12}) e^{-\beta u_{12}(\Delta\xi_{12})} \int d\boldsymbol{r}^{N-1} dq^{N-1} e^{-\beta \sum_{\substack{i \neq j \\ i,j \neq 1,2}}^{N} u_{ij}(\Delta\xi_{ij})} \tag{A.6}$$

We have absorbed the integral over $d\boldsymbol{r}_1 dq_1$ into the integral over the remaining particles. Now, this partition function has been separated into a term that depends only on relative pairwise configuration, given entirely by the position and orientation of particle 2 in the reference frame of particle 1, and a term that depends on all other particles aside from particle 2. We can define a free energy, $\tilde{F}_{12}(\Delta\xi_{12})$, associated with this latter term. It is the free energy of the sea particles given the fixed configuration $\Delta\xi_{12}$. Then:

$$Z = \int d\Delta\xi_{12} J(\Delta\xi_{12}) e^{-\beta u_{12}(\Delta\xi_{12})} e^{-\beta \tilde{F}_{12}(\Delta\xi_{12})}$$

$$\int d\Delta\xi_{12} e^{-\beta F_{12}(\Delta\xi_{12})} = \int d\Delta\xi_{12} J(\Delta\xi_{12}) e^{-\beta u_{12}(\Delta\xi_{12})} e^{-\beta \tilde{F}_{12}(\Delta\xi_{12})}$$

$$F_{12}(\Delta\xi_{12}) = u_{12}(\Delta\xi_{12}) - k_B T \log\left[J(\Delta\xi_{12})\right] + \tilde{F}_{12}(\Delta\xi_{12}) \tag{A.7}$$

Finally, the competition between the particle pair and the sea becomes clear: the Jacobian encodes the contribution to the PMFT (associated with the pairwise configuration $\Delta\xi_{12}$) from the pair of particles in isolation. The Jacobian is a term that scales the phase space volume associated with the relative pairwise configuration $\Delta\xi_{12}$, such that it corresponds to an actual phase space volume in terms of absolute particle positions and orientations. When the Jacobian is large, then the phase space volume associated with $\Delta\xi_{12}$ is large, meaning that more pairs of absolute particle positions and orientations correspond to the relative configuration $\Delta\xi_{12}$. Higher $J$ lowers $F_{12}$, as it should, since a larger phase space volume associated with $\Delta\xi_{12}$ means higher configurational entropy for the particle pair. $\tilde{F}_{12}$, on the other hand, generally grows larger in hard particle systems as $J$ grows larger, since a higher configurational entropy for a pair of particles usually means a lower accessible free volume for the surrounding sea of particles. This effect, however, is density or pressure-dependent. Thus, $F_{12}$ at any density is minimized by some $\Delta\xi_{12}$ according to a trade-off between increasing $J(\Delta\xi_{12})$ and decreasing $\tilde{F}_{12}(\Delta\xi_{12})$. Through the prism of local dense packing, $F_{12}$ is minimized by an arrangement of particles 1 and 2 that is dense enough such that it gives free volume to the surrounding sea, thereby lowering $\tilde{F}_{12}$, but not too dense, such that $J$ is not too small.

# APPENDIX B

# Cluster compression and configuration space at intermediate pressures: the case of 7 cubes

When generating dense clusters of cubes via spherical confinement, we compared our results for $N = (4 - 20)$ cubes to dense cube clusters obtained in Ref. [107] and noticed one significant discrepancy. The densest cluster of 7 cubes found in Ref. [107], a central cube surrounded by 6 cubes in face-face contact with it (Fig. B.1a), is denser than our densest 7 cube cluster (Fig. B.1b) by $\Delta\phi_{circ} \sim 4.4 \times 10^{-2}$. This value is about 15 times larger than the next largest value of $\Delta\phi_{circ}$. We were surprised by this high value of $\Delta\phi_{circ}$, and unable to achieve the denser cluster in 1000 replicate runs using our compression protocol. In this appendix, we explore this discrepancy and its implications for cluster generation via spherical confinement and compression.

We hypothesize that the discrepancy is due to the limited phase space available to the cluster in its denser configuration in an intermediate pressure range during our compression. If that is the case, then accordingly the denser cluster is statistically less likely to be generated via our compression scheme. By the end of the compression, at high pressure and small container volume, the system has settled into a configuration that corresponds to a local free energy minimum. It cannot rearrange itself into the

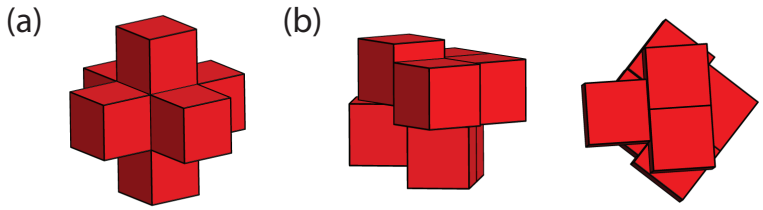


Figure B.1: Comparison of the densest cluster found in the literature of 7 cubes inside a sphere, and the less dense cluster found by our methods. (a) The denser packing (DP) of 7 cubes, found in Ref. [107]. (b) Two views of the less dense packing (LDP) of 7 cubes, which is the densest cluster found via our compression scheme.

denser cluster and reach the lower free energy minimum, due to high pressure and the presence of the container; it is trapped in a local free energy basin.

To test this hypothesis, we first ran 50 compression simulations in which we artificially increased the likelihood of forming the denser configuration (hereafter called the DP, or denser packing), to check that our compression scheme could in fact find the DP with a little help. We fixed a central cube in the center of the container, and did not move it over the course of the simulation, while allowing the other 6 cubes to move freely. We then compressed the container identically as before. We found that the DP formed 50/50 times in this case, providing evidence that one cube moving to the center of the cluster is the barrier to formation of the DP via our compression scheme.

To analyze this barrier more quantitatively, we constructed the DP by hand, and melted it via an expansion protocol that was exactly our compression protocol in reverse. We also melted the densest cluster we found (hereafter called the LDP, or less dense packing) in the same fashion. We melted each cluster 50 times, and used data from these melting simulations to investigate the phase space available to each cluster at intermediate and high pressures (see Fig. B.2, explained in detail in the following paragraphs). It is a subtle point, but we should note that during our melting

simulations we *did not* tune translation, rotation, or box resize move sizes to maintain constant acceptance ratios, as we did during the compression simulations. Rather, we kept move sizes fixed and identical across all melting simulations. We did this in order to accurately compare MC statistics across simulations.

We considered the DP to be fully melted at the pressure at which its central cube escaped the cage of the six particles surrounding it, and all particles could explore phase space equally. To approximate this pressure for the DP, we plotted the position variance $\sigma_{r_0}^2 \equiv \left\langle (\boldsymbol{r_0} - \langle \boldsymbol{r_0} \rangle)^2 \right\rangle$ as a function of reduced pressure, where $\boldsymbol{r_0}$ is the position of the center of mass of the central particle and brackets indicate ensemble averaging over all 50 simulation replicates at each pressure. It is the red dotted line in Fig. B.2a. We also plotted $\sigma_r^2 \equiv \frac{1}{7}\sum_i \sigma_{r_i}^2$ for both the DP and the LDP. $\sigma_r^2$ is the average position variance $\sigma_{r_i}^2$ for all seven particles in the cluster. $\sigma_{r_0}^2$ rises from zero and converges to the average position variance at a pressure of about $p^* \sim 1.72$, indicated by a vertical black line in Fig. B.2a. At this pressure the central cube escapes the cage of the six cubes surrounding it.

At intermediate pressures above $p^* \sim 1.72$, we hypothesize that the DP explores less phase space than the LDP, resulting in a lower probability that the seven cubes will condense into the DP via the caging of the central particle. Note, however, that the DP is nevertheless denser than the LDP, and is necessarily entropically favored over the LDP at infinite pressures. Therefore, the DP should explore more phase space than the LDP at the highest pressures in our melting simulations. This is already indicated by the plot of $\sigma_r^2$ for both the DP and LDP. The inset of Fig. B.2a, a close-up view of the plots at high pressure, shows that the average position variance for the DP is higher than that for the LDP for pressures higher than $p^* \sim 80$. By $p^* \sim 90$ this difference in average position variances cannot be explained by the error affiliated with either value. It is small (as a reference point consider that the circumsphere radius of a single cube is 1 in our simulations), but consistently present.

Our hypothesis, that the DP explores less phase space than the LDP at intermediate pressures above $p^* \sim 1.72$, is bolstered by comparing particle move acceptance ratios during the DP and LDP melting simulations. Since our trial move sizes in all simulations are identical, we may regard our simulation as a numerical MC volume integration in which the particle move acceptance ratio is proportional to the free volume available to the particles at a particular pressure. This technique for the calculation of available free volume to particles in a cluster was used in Ref. [129], albeit for the contiguous free volume available to a single particle at thermal equilibrium. Here, we compare particle move acceptance ratios as a function of pressure for both the DP and the LDP, to approximately compare the free volume available to all particles in each cluster. Fig. B.2b shows $\langle \Delta acc \rangle \equiv \langle acc_{LDP} - acc_{DP} \rangle$, where $acc$ is the particle move acceptance ratio for the melting of a given cluster, and brackets indicate ensemble averaging over all 50 simulation replicates at each pressure. A vertical line at $p^* \sim 1.72$, at which the central particle in the DP escapes the cage of the six particles surrounding it, is also shown for reference. Below $p^* \sim 1.72$, $\Delta acc$ is usually within error of zero, indicating that the free volume available to the particles in each cluster is approximately equal. Note, however, that $\Delta acc$ is distinctly higher than zero for a range of pressures above $p^* \sim 1.72$, indicating that there is more free volume available to the particles in the LDP at these pressures. $\Delta acc$ distinctly drops below zero at the highest pressures, however, indicating that the DP is entropically favored over the LDP at pressures approaching infinity, as it must be.

We believe this evidence strongly indicates that the DP, although entropically favorable at pressures approaching infinity, is entropically unfavorable in an intermediate pressure regime in which the central particle is caged by its six neighbors. This may explain why our compression scheme could not find the DP even in 1000 tries. However, our compression scheme did find other dense packings in which a central particle is surrounded by several neighboring particles. Notably, we found a dense

packing of 9 octahedra consisting of a central octahedron surrounded by eight neighbors all face-to-face contacted with it (see Fig. 3.7 in Section III for an illustration). Our compression scheme found this packing once in 50 attempts. We aren't sure why we were able to find this packing and not the 7 cube DP; we wonder if we simply got lucky or if there is some difference in the free volume available to each cluster as it forms during our compression. A more thorough investigation will be required to fully elucidate this matter.

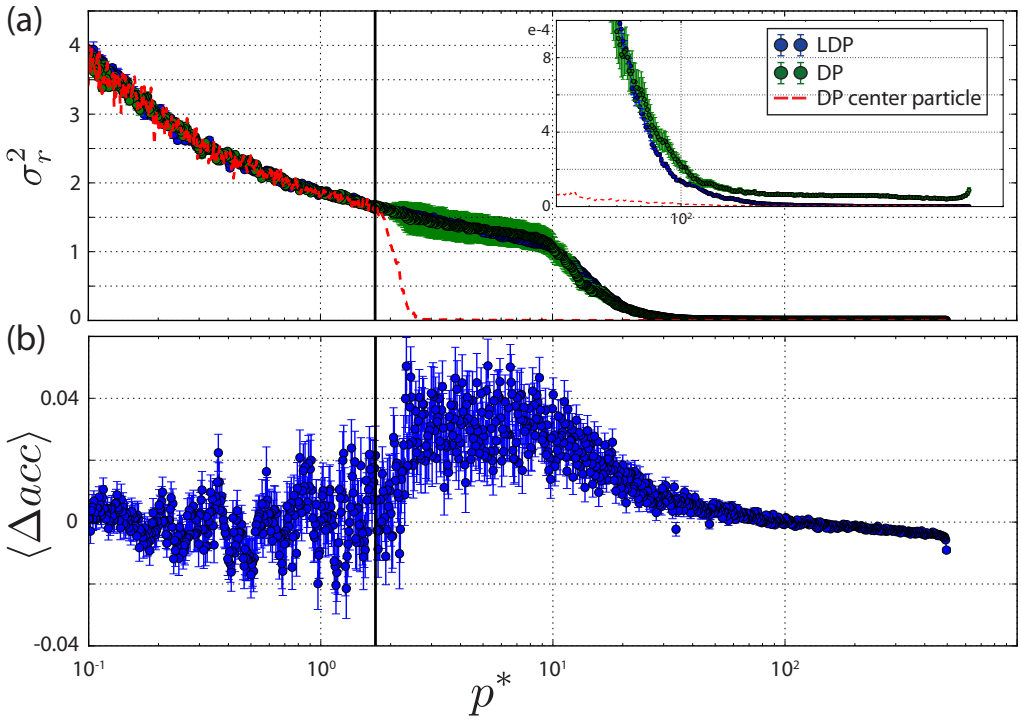


Figure B.2: Evidence that the densest cluster found in the literature, although entropically favorable at pressures approaching infinity, is entropically unfavorable in an intermediate pressure regime in which its central particle is caged by its six neighbors. (a) $\sigma_r^2$, position variance per particle, of our dense cluster of 7 cubes (LDP, plotted in blue) and the denser cluster of 7 cubes from Ref. [107] (DP, plotted in green). Error bars indicate the variance of the position variance across all 7 particles. The red dotted line is the position variance of the central particle of the DP; it converges from a value of zero to the average across all particles when the central cube escapes from the cage of the six particles around it. A black vertical line indicates the approximate pressure at which this occurs, $p^* \sim 1.72$. The inset is a close-up view of this plot at high pressures; note that the position variance of the DP remains higher than that of the LDP, indicating that it is entropically favorable as pressure tends toward infinity. (b) $\langle \Delta acc \rangle \equiv \langle acc_{LDP} - acc_{DP} \rangle$, the difference between the average particle move acceptance ratio for all LDP melting simulations and that for all DP simulations. Note that for a range of pressures above the vertical line at $p^* \sim 1.72$, $acc_{LDP} > acc_{DP}$, indicating that there is more free volume available to the particles in the LDP at these pressures. At the highest pressures, however, $acc_{DP} > acc_{LDP}$, indicating that the DP is entropically favored over the LDP here.

# APPENDIX C

# Non-Gaussianity of Monte Carlo sampling at short times

Here we provide some justification for the measured increase at short times of the non-Gaussian parameter $\alpha(t)$ in the glass-forming systems of hard polyhedra detailed in Section IV. We used Monte Carlo simulations to explore dynamical behavior in these systems; Monte Carlo methods can simulate a diffusive process if only local moves are made. In this case, the simulation is effectively a random walk, which becomes a Gaussian distribution as the number of steps taken on the walk goes to infinity. As the number of steps taken goes to zero, however, the system becomes decidedly non-Gaussian, and $\alpha > 0$.

To show this, we idealize the MC process, and compute $\alpha$ exactly in a toy model. First let's start in one dimension, and give our MC sampling method three options: particles can either remain in place with probability $s$, move to $+L$ with probability $m/2$, or move to $-L$ with probability $m/2$, with $m + s = 1$. This is technically a trinomial distribution. We will follow the treatment of a random walk in Nelson's *Biological Physics* [232]:

Let the displacement of step $j$ be $k_j L$, where $k_j = 0$ with probability $s$, and

$k_j = \pm 1$ with probability $m/2$. Then consider all possible trajectories of $N$ steps:

$$\begin{aligned}\left\langle x_N^2 \right\rangle &= \left\langle (x_{N-1} + k_N L)^2 \right\rangle \\ &= \left\langle x_{N-1}^2 \right\rangle + 2L \left\langle x_{N-1} k_N \right\rangle + L^2 \left\langle k_N^2 \right\rangle \\ &= \left\langle x_{N-1}^2 \right\rangle + L^2 m \ . \end{aligned} \tag{C.1}$$

To get from line 2 to line 3 above, note that $\langle k_N^2 \rangle = 0s + m/2 + m/2 = m$, and that $\langle x_{N-1} k_N \rangle$ evaluates to zero. This is because $x_{N-1}$ and $k_N$ are uncorrelated, so we can split that average of a product into a product of averages, and $\langle k_N \rangle = 0$. As another explanation, note that for every value of $x_{N-1}$, there are 3 contributions to the ensemble average: $k_N = 0$ with probability $s$, $k_N = 1$ with probability $m/2$, and $k_N = -1$ with probability $m/2$. These average to zero.

We can compute that $\langle x_1^2 \rangle = \langle x_0^2 \rangle + L^2 m = L^2 m$, and then use the recursion relation to determine that:

$$\left\langle x_N^2 \right\rangle = N m L^2 \ . \tag{C.2}$$

We can also consider $\langle x_N^4 \rangle$:

$$\begin{aligned}\left\langle x_N^4 \right\rangle &= \left\langle (x_{N-1} + k_N L)^4 \right\rangle \\ &= \left\langle x_{N-1}^4 \right\rangle + 4L \left\langle x_{N-1}^3 k_N \right\rangle \\ &+ 6L^2 \left\langle x_{N-1}^2 k_N^2 \right\rangle + 4L^3 \left\langle x_{N-1} k_N^3 \right\rangle + L^4 \left\langle k_N^4 \right\rangle \\ &= \left\langle x_{N-1}^4 \right\rangle + L^4 m + 6L^2 m \left\langle x_{N-1}^2 \right\rangle \\ &= \left\langle x_{N-1}^4 \right\rangle + L^4 m \left(1 + 6m(N-1)\right) \ . \end{aligned} \tag{C.3}$$

To get from line 2 to line 3, first note that $\langle k_N^4 \rangle = 0s + m/2 + m/2 = m$. The terms that contain odd powers of $k_N$ go to zero as per our previous argument involving

$\langle x_{N-1}k_N\rangle$. Then, to evaluate $\left\langle x_{N-1}^2 k_N^2\right\rangle$, we can again note that $x_{N-1}$ and $k_N$ are uncorrelated, and $\langle k_N^2\rangle = m$, so $\left\langle x_{N-1}^2 k_N^2\right\rangle = m\left\langle x_{N-1}^2\right\rangle$. Line 4 proceeds from line 3 by the previous result: $\left\langle x_{N-1}^2\right\rangle = (N-1)mL^2$.

We can compute that $\langle x_1^4\rangle = \langle x_0^4\rangle + L^4 m = L^4 m$, and use the recursion relation to determine that:

$$\left\langle x_N^4\right\rangle = L^4 m\left(N + 6m\sum_{n=1}^{N}(n-1)\right) \tag{C.4}$$

$$\begin{aligned}\sum_{n=1}^{N}(n-1) &= \sum_{n=0}^{N} n - \sum_{n=1}^{N} 1 \\ &= \frac{N}{2}(N+1) - N \\ &= \frac{N}{2}(N-1)\ .\end{aligned} \tag{C.5}$$

To get from line 1 to line 2, note that the first sum can be broken into pairs, $(0+N)+(1+N-1)+\ldots$. If N is odd, there are exactly $\frac{N+1}{2}$ of these pairs, for a total sum of $N\frac{N+1}{2}$. If N is even, there are exactly $\frac{N}{2}$ of these pairs, and there is a left-over term $\frac{N}{2}$ that also contributes to the sum, for a total sum of $N\frac{N}{2} + \frac{N}{2} = \frac{N}{2}(N+1)$. Thus,

$$\begin{aligned}\left\langle x_N^4\right\rangle &= L^4 m\left(N + 6m\frac{N}{2}(N-1)\right) \\ &= L^4 m\left(3mN^2 + N(1-3m)\right)\ .\end{aligned} \tag{C.6}$$

As $N\to\infty$, the first term dominates the expression, and $\left\langle x_N^4\right\rangle / \left\langle x_N^2\right\rangle^2 \to 3m^2L^4/m^2L^4 = 3$, a result that can be proven to be true for the Gaussian distribution in 1D. Let's

set $N = 1$ (to mimic the short time limit in our MC simulation):

$$\begin{aligned} \frac{\langle x_1^4 \rangle}{\langle x_1^2 \rangle^2} &= \frac{L^4 m}{L^4 m^2} \\ &= \frac{1}{m} \, . \end{aligned} \tag{C.7}$$

As $m \to 0$, or the probability of moving becomes increasingly unlikely, this expression diverges, and the distribution consequently gets increasingly "tail-heavy."

We now move to 3D by employing a few tricks:

$$\begin{aligned} \left\langle r_1^2 \right\rangle &= \left\langle x_1^2 + y_1^2 + z_1^2 \right\rangle \\ &= 3 \left\langle x_1^2 \right\rangle \\ &= 3L^2 m \, , \end{aligned} \tag{C.8}$$

and

$$\begin{aligned} \left\langle r_1^4 \right\rangle &= \left\langle \left( x_1^2 + y_1^2 + z_1^2 \right)^2 \right\rangle \\ &= \left\langle x_1^4 + y_1^4 + z_1^4 + 2x_1^2 y_1^2 + 2x_1^2 z_1^2 + 2y_1^2 z_1^2 \right\rangle \\ &= 3 \left\langle x_1^4 \right\rangle + 6 \left\langle x_1^2 \right\rangle^2 \\ &= 3L^4 m + 6L^4 m^2 \\ &= 3L^4 m(1 + 2m) \, , \end{aligned} \tag{C.9}$$

Thus,

$$\begin{aligned} \frac{\langle r_1^4 \rangle}{\langle r_1^2 \rangle^2} &= \frac{3L^4 m(1 + 2m)}{9L^4 m^2} \\ &= \frac{1}{3m} + \frac{2}{3} \, . \end{aligned} \tag{C.10}$$

The non-Gaussian parameter $\alpha$ is correspondingly:

$$\begin{aligned}\alpha &= \frac{3\left\langle r_1^4\right\rangle}{5\left\langle r_1^2\right\rangle^2} - 1 \\ &= \frac{1}{5m} - \frac{3}{5}\,. \end{aligned} \tag{C.11}$$

We can note several things about the above quantity. If $m = 1$, and a move is always made, $\langle r_1^4\rangle = \langle r_1^2\rangle^2$ and $\alpha$ is negative. The distribution resembles that of a Bernoulli distributed coin toss, which is known to have a negative excess kurtosis. If $m = 1/3$, $\alpha = 0$. For $m < 1/3$, however, $\alpha > 0$, and the system becomes increasingly tail-heavy. At the reasonable translation acceptance ratio $m = 0.1$, for example, $\alpha = 1.4$. Indeed, this number is comparable to values of $\alpha$ at small times shown in Fig. 4.4.

# APPENDIX D

## Misorientation angle distributions and spaces

Misorientation distributions have been extensively studied in the context of polycrystalline materials with distributions of grain boundary angles. In our work, notably in Section IV, we are often concerned with misorientations between anisotropic particles with various symmetries. We can leverage prior work in the polycrystallinity community to establish a theoretical framework for this problem. More specifically, let's consider how to find a distribution of misorientation *angles*, given a distribution of misorientations more generally.

Consider a misorientation $r$ between two unit quaternions $p$ and $q$, so that $p = rq$. $r$ is itself a unit quaternion, and is described fully by a rotation of angle $\omega$ about a rotation axis $\hat{n}$. Thus, it is a function of three variables, $r(\omega, \theta, \phi)$. It lives on the unit 3-sphere (with antipodal points identified with each other, since $r$ and $-r$ effect the same rotation). We can define the probability density $M(r) \equiv M(\omega, \theta, \phi)$ of observing the misorientation $r$. Then, we can compute the probability density $p(\omega)$ of observing the misorientation angle $\omega$ by integrating over the part of the hyperspherical volume element that depends on $\theta$ and $\phi$.

Let's look at the simple example of a uniform distribution of random misorientations. In this case, $M(r) = \frac{1}{2\pi^2}$, since it must be a constant everywhere and integrate

to 1 over the unit 3-sphere. (The area of the unit 3-sphere is $2\pi^2$.) Then we can find $p(\omega)$:

$$\begin{aligned} p(\omega) &= \int_0^{2\pi} \int_0^{\pi} \left(\frac{1}{2\pi^2}\right) \sin^2\left(\frac{\omega}{2}\right) \sin\theta d\theta d\phi \\ &= \frac{2}{\pi} \sin^2\left(\frac{\omega}{2}\right) \end{aligned} \tag{D.1}$$

The above integral is over the unit 3-sphere; the volume element of the unit 3-sphere is derivable by noting that an a unit quaternion of rotation angle $\omega$ and rotation axis $\hat{n}$ can by identified as a vector in the direction of $\hat{n}$ pointing to a spot on the surface of a 2-sphere of radius $\sin\left(\frac{\omega}{2}\right)$. Thus, an integral over $\hat{n}$, given a value of $\omega$, is a surface integral over a sphere of radius $\sin\left(\frac{\omega}{2}\right)$.

We can check that indeed $p(\omega)$ found above does integrate to 1 over the range of $\omega \in [0, \pi]$. This distribution goes to zero as $\omega$ goes to zero, since there are fewer and fewer unique misorientations corresponding to smaller and smaller misorientation angles.

The situation becomes more complicated, however, when crystalline grains (or particles, in our case) have symmetry; in that case, there is a set of equivalent orientations for each grain/particle, and misorientations between grains or particles must be treated with more care. Polycrystallinity literature addresses this problem quite elegantly with the concept of the "misorientation space," or the unique set of relative orientations (or unique portion of the surface of the hypersphere) of two objects according to the crystal symmetries involved. This space can be projected down into three dimensions, in the same way that the full hypersphere can be.

Then the set of all unique misorientations of a given angle $\omega$ will be the intersection of this misorientation space and a sphere of radius $\sin\left(\frac{\omega}{2}\right)$ centered at the origin. We can call this intersection region $\Omega(\omega)$, and integrate over it to obtain the proper

probability distribution:

$$p(\omega) = \int_{\Omega(\omega)} M(\omega, \theta, \phi) \sin^2\left(\frac{\omega}{2}\right) \sin\theta d\theta d\phi \tag{D.2}$$

$p(\omega)$ is then typically a piecewise function of $\omega$, with a characteristic "sharkfin" shape in many cases. The shape of this distribution is somewhat intuitive: it again goes to zero as $\omega$ goes to zero, as in the case of the random distribution, since particles don't know they are symmetric at small misorientation angles. At larger misorientation angles, symmetry restricts the number of available unique misorientations, so $p(\omega)$ again drops to zero. See Fig. 2.1 for examples of this sharkfin-like distribution for tetrahedral and octahedral symmetry groups.

Luckily for us, the misorientation space and corresponding $p(\omega)$ distribution has already been calculated in a variety of ways for numerous crystallographic symmetries. The first distribution was calculated by Mackenzie [233] and then Handscomb [234] for cubic symmetry. Later, "generalized" Mackenzie distributions for other crystallographic groups were calculated [47, 48, 235].

# BIBLIOGRAPHY

# BIBLIOGRAPHY


[1] R. A. L. Jones, *Soft Condensed Matter* (Oxford University Press, New York, 2002).

[2] S. C. Glotzer and M. J. Solomon, Nat. Mater. **6**, 557 (2007).

[3] K. L. Young, M. L. Personick, M. Engel, P. F. Damasceno, S. N. Barnaby, R. Bleher, T. Li, S. C. Glotzer, B. Lee, and C. A. Mirkin, Angew. Chem. Int. Ed. **52**, 13980 (2013).

[4] F. Li, D. P. Josephson, and A. Stein, Angew. Chem., Int. Ed. **50**, 360 (2011).

[5] T. S. Ahmadi, Z. L. Wang, T. C. Green, A. Henglein, and M. A. El-Sayed, Science **272**, 1924 (1996).

[6] H. Song, F. Kim, S. Connor, G. A. Somorjai, and P. Yang, J. Phys. Chem. B **109**, 188 (2005).

[7] T. K. Sau and C. J. Murphy, J. Am. Chem. Soc. **126**, 8648 (2004).

[8] A. R. Tao, S. Habas, and P. Yang, Small **4**, 310 (2008).

[9] S. E. Habas, H. Lee, V. Radmilovic, G. A. Somorjai, and P. Yang, Nat. Mater. **6**, 692 (2007).

[10] F.-R. Fan, D.-Y. Liu, Y.-F. Wu, S. Duan, Z.-X. Xie, Z.-Y. Jiang, and Z.-Q. Tian, J. Am. Chem. Soc. **130**, 6949 (2008).

[11] D. Seo, J. C. Park, and H. Song, J. Am. Chem. Soc. **128**, 14863 (2006).

[12] A. Demortière, P. Launois, N. Goubet, P.-A. Albouy, and C. Petit, J. Phys. Chem. B **112**, 14583 (2008).

[13] L. Rossi, S. Sacanna, W. T. M. Irvine, P. M. Chaikin, D. J. Pine, and A. P. Philipse, Soft Matter **7**, 4139 (2011).

[14] J. Zhang, Z. Luo, B. Martens, Z. Quan, A. Kumbhar, N. Porter, Y. Wang, D.-M. Smilgies, and J. Fang, J. Am. Chem. Soc. **134**, 14043 (2012).

[15] Y. Xia, X. Xia, Y. Wang, and S. Xie, MRS Bulletin **38**, 335 (2013).

[16] W. Cai, U. K. Chettiar, A. V. Kildishev, and V. M. Shalaev, Nat. Photonics **1**, 224 (2007).

[17] A. Murugan, Z. Zeravcic, M. P. Brenner, and S. Leibler, Proc. Natl. Acad. Sci. **112**, 54 (2015), arXiv:1408.6893 .

[18] G. Katsikis, J. S. Cybulski, and M. Prakash, Nat. Phys. **11** (2015), 10.1038/nphys3341.

[19] J. L. England, Nat. Nanotechnol. **10**, 919 (2015), arXiv:arXiv:1502.07086 .

[20] J. M. A. Carnall, C. A. Waudby, A. M. Belenguer, M. C. A. Stuart, J. J.-P. Peyralans, and S. Otto, Science (80-. ). **327**, 1502 (2010).

[21] A. D. Dinsmore, M. F. Hsu, M. G. Nikolaides, M. Marquez, A. R. Bausch, and D. A. Weitz, Science **298**, 1006 (2002).

[22] M. Jamal, N. Bassik, J. H. Cho, C. L. Randall, and D. H. Gracias, Biomaterials **31**, 1683 (2010).

[23] M. Wuttig and N. Yamada, Nat. Mater. **6**, 824 (2007).

[24] F. Mitschke, *Fiber Optics: Physics and Technology* (Springer Berlin Heidelberg, 2016).

[25] J. P. Hansen and I. R. McDonald, *Theory of Simple Liquids: with Applications to Soft Matter* (Elsevier Science, 2013).

[26] C. P. Royall and S. R. Williams, Phys. Rep. **560**, 1 (2015).

[27] F. C. Frank, Proc. R. Soc. A Math. Phys. Eng. Sci. **215**, 43 (1952).

[28] Y. Q. Cheng and E. Ma, Prog. Mater. Sci. **56**, 379 (2011).

[29] D. S. Eisenberg and W. Kauzmann, *The Structure and Properties of Water* (Oxford University Press, 1969).

[30] S. Hess, Zeitschrift fur Naturforsch. - Sect. A J. Phys. Sci. **35**, 69 (1980).

[31] A. C. Mituś and A. Z. Patashinskii, Phys. Lett. A **87**, 179 (1982).

[32] A. Z. Patashinski, A. C. Mitus, and M. a. Ratner, Phys. Rep. **288**, 409 (1997).

[33] D. R. Nelson and J. Toner, Phys. Rev. B **24**, 363 (1981).

[34] D. Erdemir, A. Y. Lee, and A. S. Myerson, Acc. Chem. Res. **42**, 621 (2009).

[35] H. Tanaka, Eur. Phys. J. E **35**, 113 (2012), arXiv:1307.0621 .

[36] G. van Anders, N. K. Ahmed, R. Smith, M. Engel, and S. C. Glotzer, ACS Nano **8**, 931 (2014).

[37] G. van Anders, D. Klotsa, N. K. Ahmed, M. Engel, and S. C. Glotzer, Proc. Natl. Acad. Sci. U. S. A. **111**, E4812 (2014).

[38] P. F. Damasceno, M. Engel, and S. C. Glotzer, ACS Nano **6**, 609 (2012).

[39] J. H. Conway and N. Sloane, *Sphere Packings, Lattices and Groups*, 3rd ed. (Springer-Verlag New York, Inc, New York, NY, 1999) pp. 97-98.

[40] G. van Anders, D. Klotsa, A. S. Karas, P. M. Dodd, and S. C. Glotzer, ACS Nano **9**, 9542 (2015).

[41] D. Frenkel and B. Smit, *Understanding Molecular Simulation: From Algorithms to Applications*, 2nd ed. (Academic Press, San Diego, 2002).

[42] Y. Geng, G. van Anders, P. M. Dodd, J. Dshemuchadse, and S. C. Glotzer, (2017), arXiv:1712.02471v1, arXiv:1712.02471 .

[43] R. K. Cersonsky, G. van Anders, P. M. Dodd, and S. C. Glotzer, Proc. Natl. Acad. Sci. , 1 (2018).

[44] Y. Geng, G. van Anders, and S. C. Glotzer, (2018), arXiv:1801.06219 .

[45] J. A. Anderson, M. Eric Irrgang, and S. C. Glotzer, Comput. Phys. Commun. **204**, 21 (2015).

[46] J. K. Mackenzie, Biometrika **45**, 229 (1958).

[47] A. Morawiec, J. Appl. Crystallogr. **28**, 289 (1995).

[48] J. K. Mason and C. A. Schuh, Acta Mater. **57**, 4186 (2009).

[49] E. S. Harper, M. Spellings, J. Anderson, and S. C. Glotzer, (2016), 10.5281/ZENODO.166564.

[50] W. Kabsch, Acta Crystallogr. Sect. A **32**, 922 (1976).

[51] L. Kavraki, "Geometric methods in structural computational biology," `https://cnx.org/contents/f5c31f8e-7807-4c76-95f8-657d9251fdfb@6.3` (2007), [Online; accessed 3-July-2018].

[52] P. J. Steinhardt, D. R. Nelson, and M. Ronchetti, Phys. Rev. B **28**, 784 (1983).

[53] A. S. Keys, C. R. Iacovella, and S. C. Glotzer, J. Comput. Phys. **230**, 6438 (2011).

[54] A. S. Keys, C. R. Iacovella, and S. C. Glotzer, , 1 (2010), arXiv:1012.4527 .

[55] E. G. Teich, G. van Anders, D. Klotsa, J. Dshemuchadse, and S. C. Glotzer, Proc. Natl. Acad. Sci. U. S. A. **113**, E669 (2016).

[56] J. Balbo, P. Mereghetti, D.-P. Herten, and R. C. Wade, Biophys. J. **104**, 1576 (2013).

[57] R. Ellis, Trends Biochem. Sci. **26**, 597 (2001).

[58] T. Cremer and C. Cremer, Nat. Rev. Genet. **2**, 292 (2001).

[59] D. Marenduzzo, C. Micheletti, and E. Orlandini, J. Phys. Condens. Matter **22**, 283102 (2010).

[60] J. A. Åström and M. Karttunen, Phys. Rev. E **73**, 062301 (2006).

[61] T. Hayashi and R. W. Carthew, Nature **431**, 647 (2004).

[62] D. B. Cines, T. Lebedeva, C. Nagaswami, V. Hayes, W. Massefski, R. I. Litvinov, L. Rauova, T. J. Lowery, and J. W. Weisel, Blood **123**, 1596 (2014).

[63] M. Hifi and R. M'Hallah, Adv. Oper. Res. **2009**, 150624 (2009).

[64] G. Wäscher, H. Haußner, and H. Schumann, Eur. J. Oper. Res. **183**, 1109 (2007).

[65] A. van Blaaderen, Science **301**, 470 (2003).

[66] Y. Wang, Y. Wang, D. R. Breed, V. N. Manoharan, L. Feng, A. D. Hollingsworth, M. Weck, and D. J. Pine, Nature **491**, 51 (2012).

[67] C. L. Phillips, E. Jankowski, B. J. Krishnatreya, K. V. Edmond, S. Sacanna, D. G. Grier, D. J. Pine, and S. C. Glotzer, Soft Matter **10**, 7468 (2014).

[68] O. D. Velev, A. M. Lenhoff, and E. W. Kaler, Science **287**, 2240 (2000).

[69] V. N. Manoharan, M. Elsesser, and D. Pine, Science **301**, 483 (2003).

[70] S. M. Klein, V. N. Manoharan, D. J. Pine, and F. F. Lange, Langmuir **21**, 6669 (2005).

[71] Y.-S. Cho, G.-G. Yi, J.-M. Lim, S.-H. Kim, V. N. Manoharan, D. J. Pine, and S.-M. Yang, J. Am. Chem. Soc. **127**, 15968 (2005).

[72] M. T. Elsesser, A. D. Hollingsworth, K. V. Edmond, and D. J. Pine, Langmuir **27**, 917 (2011).

[73] B. de Nijs, S. Dussi, F. Smallenburg, J. D. Meeldijk, D. J. Groenendijk, L. Filion, A. Imhof, A. van Blaaderen, and M. Dijkstra, Nat. Mater. **14**, 56 (2015).

[74] J. Guzowski and P. Garstecki, Phys. Rev. Lett. **114**, 188302 (2015).

[75] L. M. Liz-Marzán, Langmuir **22**, 32 (2006).

[76] C. Noguez, J. Phys. Chem. C **111**, 3806 (2007).

[77] J. B. Pendry, D. Schurig, and D. R. Smith, Science **312**, 1780 (2006).

[78] F. De Angelis, M. Patrini, G. Das, I. Maksymov, M. Galli, L. Businaro, L. C. Andreani, and E. Di Fabrizio, Nano Lett. **8**, 2321 (2008).

[79] N. Fang, H. Lee, C. Sun, and X. Zhang, Science **308**, 534 (2005).

[80] M. W. Klein, C. Enkrich, M. Wegener, and S. Linden, Science **313**, 502 (2006).

[81] Y. A. Urzhumov, G. Shvets, J. A. Fan, F. Capasso, D. Brandl, and P. Nordlander, Opt. Express **15**, 14129 (2007).

[82] S. N. Sheikholeslami, H. Alaeian, A. L. Koh, and J. A. Dionne, Nano Lett. **13**, 4137 (2013).

[83] A. S. Urban, X. Shen, Y. Wang, N. Large, H. Wang, M. W. Knight, P. Nordlander, H. Chen, and N. J. Halas, Nano Lett. **13**, 4399 (2013).

[84] J. A. Schuller, E. S. Barnard, W. Cai, Y. C. Jun, J. S. White, and M. L. Brongersma, Nat. Mater. **9**, 193 (2010).

[85] P. Kalpaxis and G. Rickayzen, Molecular Physics **80**, 391 (1993).

[86] J. Henzie, M. Grünwald, A. Widmer-Cooper, P. L. Geissler, and P. Yang, Nat. Mater. **11**, 131 (2011).

[87] J.-F. Camenen, Y. Descantes, and P. Richard, Phys. Rev. E **86**, 061317 (2012).

[88] M. Marechal and H. Löwen, Phys. Rev. Lett. **110**, 137801 (2013).

[89] V. Thapar, T. Hanrath, and F. A. Escobedo, Soft Matter **11**, 1481 (2015).

[90] G. T. Pickett, M. Gross, and H. Okuyama, Phys. Rev. Lett. **85**, 3652 (2000).

[91] M. Z. Yamchi and R. K. Bowles, Phys. Rev. Lett. **115**, 025702 (2015).

[92] A. Mughal, H. K. Chan, and D. Weaire, Phys. Rev. Lett. **106**, 115704 (2011).

[93] N. M. Blachman, Am. Math. Mon. **70**, 526 (1963).

[94] T. Gensane, Electron. J. Comb. **11**, 1 (2004).

[95] E. Lauga and M. P. Brenner, Phys. Rev. Lett. **93**, 238301 (2004).

[96] R. M'Hallah, A. Alkandari, and N. Mladenovic, Comput. Oper. Res. **40**, 603 (2013).

[97] M. Hifi, L. Yousef, and Z. Zhou, Cogent Eng. **2**, 994257 (2015).

[98] H. Pfoertner, "Densest Packing of Spheres in a Sphere," `http://www.randomwalk.de/sphere/insphr/spheresinsphr.html` (2013), [Online; accessed 27-Mar-2015].

[99] T. Gensane and P. Honvault, Forum Geom **14**, 371 (2012).

[100] S. I. Galiev and M. S. Lisafina, Comput. Math. Math. Phys. **53**, 1748 (2013).

[101] J. Kallrath and S. Rebennack, J. Glob. Optim. **59**, 405 (2014).

[102] P. Honvault, *About the density of optimal packings of ellipses in a square*, Tech. Rep. (L.M.P.A., 2015).

[103] J. Bennell, G. Scheithauer, Y. Stoyan, and T. Romanova, Ann. Oper. Res. **179**, 343 (2010).

[104] C. Uhler and S. J. Wright, SIAM Rev. **55**, 671 (2013), arXiv:1204.0235 .

[105] J. Kallrath, J. Glob. Optim. , 1 (2015).

[106] E. G. Birgin, R. D. Lobato, and J. M. Martínez, J. Glob. Optim. , 1 (2015).

[107] T. Gensane and P. Ryckelynck, Discrete Math. **308**, 5230 (2008).

[108] U. Betke and M. Henk, Comput. Geom. **16**, 157 (1999).

[109] A. Donev, I. Cisse, D. Sachs, E. A. Variano, F. H. Stillinger, R. Connelly, S. Torquato, and P. M. Chaikin, Science **303**, 990 (2004).

[110] S. Torquato and Y. Jiao, Nature **460**, 876 (2009).

[111] E. R. Chen, M. Engel, and S. C. Glotzer, Discrete Comput. Geom. **44**, 253 (2010).

[112] J. de Graaf, R. van Roij, and M. Dijkstra, Phys. Rev. Lett. **107**, 155501 (2011).

[113] E. R. Chen, D. Klotsa, M. Engel, P. F. Damasceno, and S. C. Glotzer, Phys. Rev. X **4**, 011024 (2014).

[114] R. Osserman, Bull. Am. Math. Soc. **84**, 1182 (1978).

[115] B. Gao, G. Arya, and A. R. Tao, Nat. Nanotechnol. **7**, 433 (2012).

[116] Y. J. Lee, N. B. Schade, L. Sun, J. A. Fan, D. R. Bae, M. M. Mariscal, G. Lee, F. Capasso, S. Sacanna, V. N. Manoharan, and G.-R. Yi, ACS Nano **7**, 11064 (2013).

[117] J. Henzie, S. C. Andrews, X. Y. Ling, Z. Li, and P. Yang, Proc. Natl. Acad. Sci. **110**, 6640 (2013).

[118] O. Echt, K. Sattler, and E. Recknagel, Phys. Rev. Lett. **47**, 1121 (1981).

[119] T. L. Beck, J. Jellinek, and R. S. Berry, J. Chem. Phys. **87**, 545 (1987).

[120] J. P. Doye and D. J. Wales, Chem. Phys. Lett. **247**, 339 (1995).

[121] T. Chen, Z. Zhang, and S. C. Glotzer, Proc. Natl. Acad. Sci. **104**, 717 (2007).

[122] A. B. Hopkins, F. H. Stillinger, and S. Torquato, J. Math. Phys. **51**, 043302 (2010).

[123] A. B. Hopkins, F. H. Stillinger, and S. Torquato, Phys. Rev. E **83**, 011304 (2011).

[124] N. Sloane, "Spherical Codes," `http://neilsloane.com/packings/` (2015), [Online; accessed 31-Mar-2015].

[125] M. Ester, H. Kriegel, J. Sander, and X. Xu, in *Proceedings of the 2nd International Conference on Knowledge Discovery and Data Mining* (AAAI Press, Portland, OR, 1996) pp. 226–231.

[126] F. Pedregosa, G. Varoquaux, A. Gramfort, V. Michel, B. Thirion, O. Grisel, M. Blondel, P. Prettenhofer, R. Weiss, V. Dubourg, J. Vanderplas, A. Passos, D. Cournapeau, M. Brucher, M. Perrot, and E. Duchesnay, Journal of Machine Learning Research **12**, 2825 (2011).

[127] A. P. Gantapara, J. de Graaf, R. van Roij, and M. Dijkstra, Phys. Rev. Lett. **111**, 015501 (2013).

[128] D. Kottwitz, Acta Crystallogr. A **47**, 158 (1991).

[129] C. L. Phillips, E. Jankowski, M. Marval, and S. C. Glotzer, Phys. Rev. E **86**, 041124 (2012).

[130] M. Gardner, *The Colossal Book of Mathematics: Classic Puzzles, Paradoxes, and Problems*, 1st ed. (W.W. Norton & Company, Inc, New York, NY, 2001) p. 135.

[131] Y. Kallus, Adv. Math. (N. Y). **264**, 355 (2014), arXiv:arXiv:1212.2551v2 .

[132] I. A. Harris, R. S. Kidwell, and J. A. Northby, Phys. Rev. Lett. **53**, 2390 (1984).

[133] J. P. K. Doye, D. J. Wales, and R. S. Berry, J. Chem. Phys. **103**, 4234 (1995).

[134] J. P. K. Doye and D. J. Wales, Phys. Rev. Lett. **86**, 5719 (2001).

[135] J. Pillardy and L. Piela, J. Phys. Chem. **99**, 11805 (1995).

[136] C. Barrón, S. Gómez, and D. Romero, Appl. Math. Lett. **9**, 75 (1996).

[137] J. P. K. Doye, M. A. Miller, and D. J. Wales, J. Chem. Phys. **110**, 6896 (1999).

[138] A. Haji-Akbari, M. Engel, A. S. Keys, X. Zheng, R. G. Petschek, P. Palffy-Muhoray, and S. C. Glotzer, Nature **462**, 773 (2009).

[139] J. E. Millstone, S. J. Hurst, G. S. Métraux, J. I. Cutler, and C. A. Mirkin, Small **5**, 646 (2009).

[140] J. Fontana, W. J. Dressick, J. Phelps, J. E. Johnson, R. W. Rendell, T. Sampson, B. R. Ratna, and C. M. Soto, Small **10**, 3058 (2014).

[141] M. Fruhnert, S. Mühlig, F. Lederer, and C. Rockstuhl, Phys. Rev. B **89**, 075408 (2014).

[142] E. G. Teich, G. van Anders, and S. C. Glotzer, (2018), under review.

[143] S. C. Glotzer, J. Non. Cryst. Solids **274**, 342 (2000), arXiv:0066-426X .

[144] M. D. Ediger, Annu. Rev. Phys. Chem. **51**, 99 (2000), arXiv:0066-426X .

[145] D. Chandler and J. P. Garrahan, Annu. Rev. Phys. Chem. **61**, 191 (2010), arXiv:0908.0418 .

[146] G. Tarjus, S. A. Kivelson, Z. Nussinov, and P. Viot, J. Phys. Condens. Matter **17**, R1143 (2005).

[147] H. Tanaka, J. Non. Cryst. Solids **351**, 3371 (2005).

[148] H. Jónsson and H. C. Andersen, Phys. Rev. Lett. **60**, 2295 (1988).

[149] D. Coslovich and G. Pastore, J. Chem. Phys. **127** (2007), 10.1063/1.2773716, arXiv:arXiv:0705.0626v2 .

[150] U. R. Pedersen, T. B. Schrøder, J. C. Dyre, and P. Harrowell, Phys. Rev. Lett. **104**, 105701 (2010).

[151] A. Malins, J. Eggers, C. P. Royall, S. R. Williams, and H. Tanaka, J. Chem. Phys. **138** (2013), 10.1063/1.4790515.

[152] A. Malins, J. Eggers, H. Tanaka, and C. P. Royall, Faraday Discuss. **167**, 405 (2013), arXiv:1306.2983 .

[153] M. Dzugutov, Phys. Rev. A **46**, 2984 (1992).

[154] M. Dzugutov, S. I. Simdyankin, and F. H. M. Zetterling, Phys. Rev. Lett. **89**, 195701 (2002).

[155] J. F. Sadoc, J. Dixmier, and A. Guinier, J. Non. Cryst. Solids **12**, 46 (1973).

[156] P. N. Pusey and W. van Megen, Nature **320**, 340 (1986).

[157] T. Kawasaki and H. Tanaka, J. Phys. Condens. Matter **22**, 232102 (2010).

[158] M. Leocmach and H. Tanaka, Nat. Commun. **3**, 974 (2012).

[159] C. Xia, J. Li, Y. Cao, B. Kou, X. Xiao, K. Fezzaa, T. Xiao, and Y. Wang, Nat. Commun. **6**, 8409 (2015).

[160] T. Kawasaki, T. Araki, and H. Tanaka, Phys. Rev. Lett. **99**, 215701 (2007).

[161] C. P. Royall, S. R. Williams, T. Ohtsuka, and H. Tanaka, Nat. Mater. **7**, 556 (2008).

[162] P. H. Gaskell, Nature **276**, 484 (1978).

[163] T. Schenk, D. Holland-Moritz, V. Simonet, R. Bellissent, and D. M. Herlach, Phys. Rev. Lett. **89**, 075507 (2002).

[164] D. B. Miracle, W. S. Sanders, and O. N. Senkov, Philos. Mag. **83**, 2409 (2003).

[165] D. B. Miracle, Nat. Mater. **3**, 697 (2004).

[166] G. W. Lee, A. K. Gangopadhyay, T. K. Croat, T. J. Rathz, R. W. Hyers, J. R. Rogers, and K. F. Kelton, Phys. Rev. B **72**, 174107 (2005).

[167] Z. W. Wu, M. Z. Li, W. H. Wang, and K. X. Liu, Nat. Commun. **6**, 6035 (2015).

[168] C. Mondal, S. Karmakar, and S. Sengupta, J. Phys. Chem. B **119**, 10902 (2015).

[169] K. Zhao and T. G. Mason, Proc. Natl. Acad. Sci. **112**, 12063 (2015).

[170] M. Goldstein, J. Chem. Phys. **51**, 3728 (1969).

[171] G. Adam and J. H. Gibbs, J. Chem. Phys. **43**, 139 (1965).

[172] V. Lubchenko and P. G. Wolynes, Annu. Rev. Phys. Chem. **58**, 235 (2007), arXiv:0607349 [cond-mat] .

[173] H. Shintani and H. Tanaka, Nat. Phys. **2**, 200 (2006).

[174] P. Ronceray and P. Harrowell, Phys. Rev. E **96**, 042602 (2017).

[175] J. Russo, F. Romano, and H. Tanaka, Phys. Rev. X **8**, 021040 (2018).

[176] D. Klotsa, E. R. Chen, M. Engel, and S. C. Glotzer, Soft Matter 2018, DOI: 10.1039/C8SM01573B.

[177] C. X. Du, G. van Anders, R. S. Newman, and S. C. Glotzer, Proc. Natl. Acad. Sci. **114**, E3892 (2017).

[178] K. C. Russell, Acta Metall. **17**, 1123 (1969).

[179] N. Tasios, A. P. Gantapara, and M. Dijkstra, J. Chem. Phys. **141** (2014), 10.1063/1.4902992.

[180] A. Rahman, Phys. Rev. **136**, 405 (1964).

[181] S. C. Glotzer, V. N. Novikov, and T. B. Schrøder, J. Chem. Phys. **112**, 509 (2000).

[182] A. S. Keys, A. R. Abate, S. C. Glotzer, and D. J. Durian, Nat. Phys. **3**, 260 (2007).

[183] K. Schmidt-Rohr, J. Appl. Crystallogr. **40**, 16 (2007).

[184] M. M. Hurley and P. Harrowell, Phys. Rev. E **52**, 1694 (1995).

[185] W. Kob, C. Donati, S. Plimpton, P. Poole, and S. Glotzer, Phys. Rev. Lett. **79**, 2827 (1997).

[186] "Sb (sn0.121sb0.879) crystal structure," Datasheet from "PAULING FILE Multinaries Ed ition – 2012", part of Springer Materials. Acces sed 2018-08-01 at `https://materials.springer.\com/isp/crystallographic/docs/sd_1123072`.

[187] A. S. Karas, J. Dschemuchadse, G. van Anders, and S. C. Glotzer, In preparation.

[188] R. K. Cersonsky, J. Dschemuchadse, J. Antonaglia, G. van Anderš, and S. C. Glotzer, (2018).

[189] V. Molinero, S. Sastry, and C. A. Angell, Phys. Rev. Lett. **97**, 075701 (2006).

[190] A. Haji-Akbari, M. Engel, and S. C. Glotzer, Phys. Rev. Lett. **107**, 1 (2011), arXiv:1106.5561 .

[191] A. Haji-Akbari, E. R. Chen, M. Engel, and S. C. Glotzer, Phys. Rev. E - Stat. Nonlinear, Soft Matter Phys. **88**, 1 (2013), arXiv:arXiv:1304.3147v2 .

[192] J. Russo and H. Tanaka, J. Chem. Phys. **145** (2016), 10.1063/1.4962166, arXiv:1611.08041 .

[193] F. H. Stillinger and A. Weber, Thomas, Phys. Rev. B **31**, 5262 (1985).

[194] P. Crowther, F. Turci, and C. P. Royall, J. Chem. Phys. **143**, 044503 (2015).

[195] M. Kobayashi and H. Tanaka, Phys. Rev. Lett. **106**, 125703 (2011).

[196] J. Taffs and C. Patrick Royall, Nat. Commun. **7**, 13225 (2016).

[197] F. Turci, G. Tarjus, and C. P. Royall, Phys. Rev. Lett. **118**, 1 (2017).

[198] P. F. Damasceno, M. Engel, and S. C. Glotzer, Science **337**, 453 (2012).

[199] R. Eppenga and D. Frenkel, Mol. Phys. **52**, 1304 (1984).

[200] M. P. Allen, J. Chem. Phys. **124** (2006), 10.1063/1.2202352, arXiv:0603027 [cond-mat] .

[201] P. E. Brumby, A. J. Haslam, E. De Miguel, and G. Jackson, Mol. Phys. **109**, 169 (2011).

[202] J. A. Anderson, E. Jankowski, T. L. Grubb, M. Engel, and S. C. Glotzer, J. Comput. Phys. **254**, 27 (2013), arXiv:1211.1646v2 .

[203] B. J. Alder and T. E. Wainwright, J. Chem. Phys. **27**, 1208 (1957).

[204] J. E. Mayer and W. W. Wood, J. Chem. Phys. **42**, 4268 (1965).

[205] R. Richert and C. A. Angell, J. Chem. Phys. **108**, 9016 (1998).

[206] R. Kurita and E. R. Weeks, Phys. Rev. E **82**, 041402 (2010).

[207] M. Ozawa, K. Kim, and K. Miyazaki, J. Stat. Mech. Theor. Exp. **2016**, 074002 (2016), arXiv:arXiv:1602.00829v1 .

[208] C. E. Pueblo, M. Sun, and K. F. Kelton, Nat. Mater. **16**, 792 (2017).

[209] J. C. Lagarias and C. Zong, Not. Am. Math. Soc. **59**, 1392 (2012).

[210] R. Kohlrausch, Ann. der Phys. und Chemie **167**, 179 (1854).

[211] G. Williams and D. C. Watts, Trans. Faraday Soc. **66**, 80 (1970), arXiv:0001055v2 [arXiv:cond-mat] .

[212] S. R. Elliott, Nature **354**, 445 (1991).

[213] S. R. Elliott, Phys. Rev. Lett. **67**, 711 (1991), arXiv:0000135489 .

[214] I. Saika-Voivod, F. Smallenburg, and F. Sciortino, J. Chem. Phys. **139** (2013), 10.1063/1.4840695, arXiv:1309.2198 .

[215] L. Berthier and G. Biroli, Rev. Mod. Phys. **83**, 587 (2011), arXiv:1011.2578 .

[216] G. Brambilla, D. El Masri, M. Pierno, L. Berthier, L. Cipelletti, G. Petekidis, and a. B. Schofield, Phys. Rev. Lett. **102**, 085703 (2009), arXiv:0809.3401 .

[217] L. Berthier and T. a. Witten, Phys. Rev. E **80**, 021502 (2009).

[218] J. Mattsson, H. M. Wyss, A. Fernandez-Nieves, K. Miyazaki, Z. Hu, D. R. Reichman, and D. A. Weitz, Nature **462**, 83 (2009).

[219] R. Böhmer and C. A. Angell, Phys.˜Rev.˜B **45**, 10091 (1992).

[220] D. J. Plazek and K. L. Ngai, Macromolecules **24**, 1222 (1991).

[221] W. Zhang, I. Ronneberger, P. Zalden, M. Xu, M. Salinga, M. Wuttig, and R. Mazzarello, Sci. Rep. **4**, 6529 (2015).

[222] E. G. Teich, G. van Anders, and S. C. Glotzer, (2018), in preparation.

[223] A. T. Cadotte, J. Dshemuchadse, P. F. Damasceno, R. S. Newman, and S. C. Glotzer, Soft Matter **12**, 7073 (2016), arXiv:1605.07160v1 .

[224] W. Zygmunt, E. G. Teich, G. van Anders, and S. C. Glotzer, In preparation.

[225] S. Lee, E. G. Teich, M. Engel, and S. C. Glotzer, In preparation.

[226] J. Kindt, S. Tzlil, A. Ben-Shaul, and W. M. Gelbart, Proc. Natl. Acad. Sci. U. S. A. **98**, 13671 (2001).

[227] A. Leforestier and F. Livolant, J. Mol. Biol. **396**, 384 (2010).

[228] A. Bolzer, G. Kreth, I. Solovei, D. Koehler, K. Saracoglu, C. Fauth, S. Müller, R. Eils, C. Cremer, M. R. Speicher, and T. Cremer, PLoS Biol. **3**, e157 (2005).

[229] A. Khalil, J. L. Grant, L. B. Caddle, E. Atzema, K. D. Mills, and A. Arneodo, Chromosom. Res. **15**, 899 (2007).

[230] L. Rossi, V. Soni, D. J. Ashton, D. J. Pine, A. P. Philipse, P. M. Chaikin, M. Dijkstra, S. Sacanna, and W. T. M. Irvine, Proc. Natl. Acad. Sci. **112**, 5286 (2015).

[231] P. M. Dodd, G. van Anders, and S. C. Glotzer, In preparation.

[232] P. Nelson, *Biological Physics (Updated Edition)* (W. H. Freeman, 2003).

[233] A. J. K. Mackenzie and M. J. Thomson, Biometrika **44**, 205 (1957).

[234] D. C. Handscomb, Can. J. Math. **10**, 85 (1958).

[235] S. Patala, J. K. Mason, and C. A. Schuh, Prog. Mater. Sci. **57**, 1383 (2012).